Polytechnic University of Marche
Doctoral School in Engineering Sciences
Curriculum in Civil, Environmental and Building Engineering
and Architecture

Coupled longitudinal-transversal vibrations of nonlinear planar Timoshenko beams with an axial end spring

Analytical modeling, numerical simulation and experimental study

Ph.D. Dissertation of:
Łukasz Kłoda

Advisor:
Prof. Stefano Lenci

Coadvisor:
Prof. Jerzy Warmiński

Curriculum Supervisor:
Prof. Stefano Lenci 2016-2018/Prof. Francesco Fatone 2018-2019

XXXII edition - new series

Polytechnic University of Marche
Doctoral School in Engineering Sciences
Curriculum in Civil, Environmental and Building Engineering
and Architecture

Coupled longitudinal-transversal vibrations of nonlinear planar Timoshenko beams with an axial end spring

Analytical modeling, numerical simulation and experimental study

Ph.D. Dissertation of:
Łukasz Kłoda

Advisor:
Prof. Stefano Lenci

Coadvisor:
Prof. Jerzy Warmiński

Curriculum Supervisor:
Prof. Stefano Lenci 2016-2018/Prof. Francesco Fatone 2018-2019

XXXII edition - new series

Polytechnic University of Marche
Doctoral School in Engineering Sciences
Faculty of Engineering
Via Brecce Bianche – 60131 Ancona (AN), Italy

Everything will pass.
The Wise Man knows this from the very
beginning and does not regret anything.

Olga Tokarczuk
Polish Nobel Laureate
in Literature 2019

Acknowledgments

I'm grateful to Professor Stefano Lenci and Professor Jerzy Warmiński for their support and for giving me the opportunity to attend this PhD course.

This work is part of the collaboration between Polytechnic University of Marche and Lublin University of Technology, which is aimed at developing a Joined Doctoral Programme.

The work is partially supported by Grant 2019/33/N/ST8/02661 from the National Science Centre, Poland.

Ancona, 2019

Łukasz Kłoda

Abstract

In the thesis, studies on nonlinear dynamics of a homogeneous and isotropic beam are performed. Partial differential equations of motion of a straight planar beam model are derived, taking into account extensibility and shearing effects, longitudinal, transverse and rotational inertia as well as different curvature definitions. For special boundary conditions (like hinged-simply supported beam with an axial spring) approximate method of *multiple time-scales* is implemented to catch various dynamic phenomena of the system, wherein free dynamics and forced-damped vibrations are represented by backbone curves and nonlinear frequency response curves, respectively. In the structure axial-transverse oscillations are coupled and the importance of combination of two modes, for instance in internal resonance, is shown. Analytical considerations are supported by numerical model elaborated in commercial software Abaqus_CAE®. Initially, the linear behaviour of the beam model in *frequency* module is tested and then backbone curves and stable frequency response curves with use of transient *dynamic explicit* module are obtained. Time-dependent simulations with *path-following* and *shooting* methods are used and outcomes are compared with analytical results. Apart from sophisticated theoretical approaches, a basic validation tests on the Euler-Bernoulli beam prototype are done. Nonlinear dynamics of kinematically excited prototype with various boundary conditions in axial direction is executed experimentally. Hardening/softening phenomena and jumps between stable solutions are observed in analytical and numerical solutions, as well as in experiments. Study on nonlinear dynamics of a beam ends with conclusions and further developments are suggested.

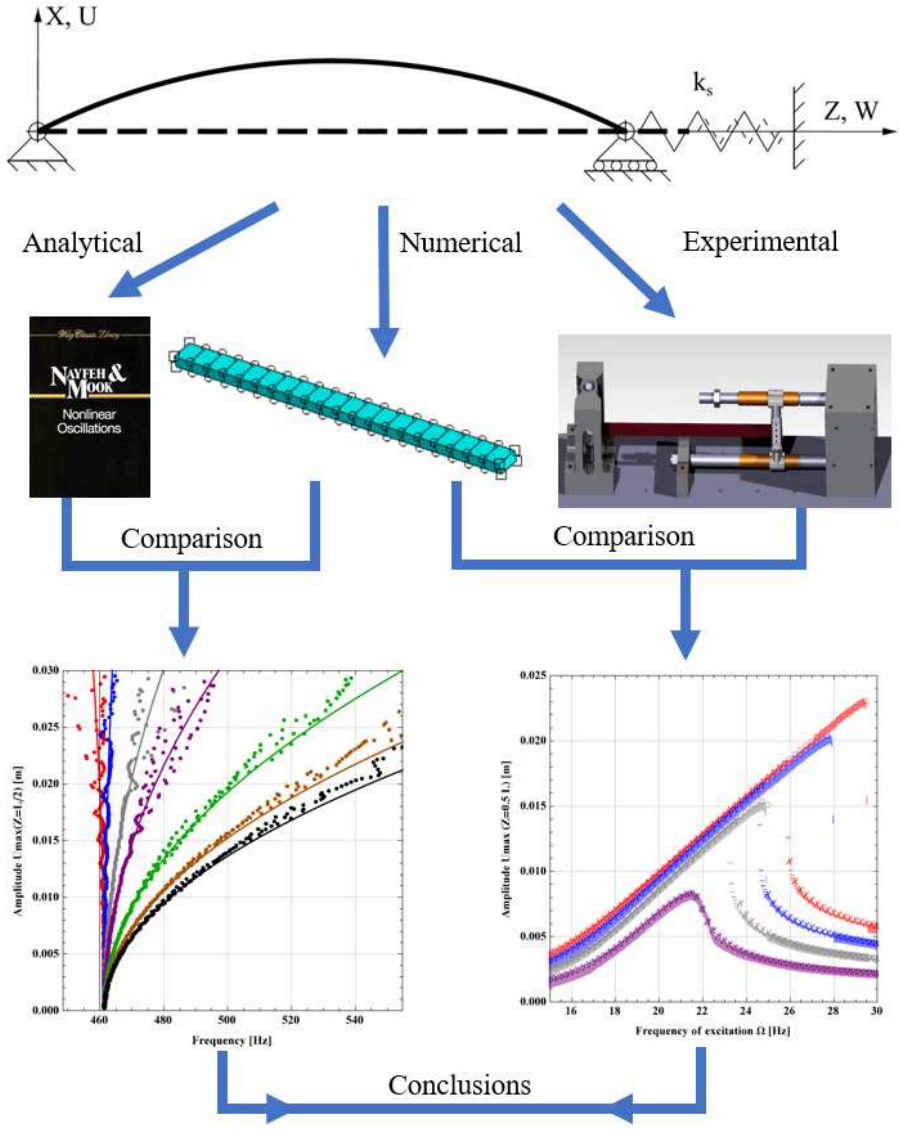

Figure 1: Graphical abstract.

Sommario

Questa tesi di dottorato analizza la dinamica non lineare di una trave omogenea e isotropa. Sono state inizialmente ricavate le equazioni differenziali alle derivate parziali del moto per un modello di trave rettilinea nel caso piano, tenendo conto degli effetti dell'estensibilità, di taglio e dell'inerzia longitudinale, trasversale e rotazionale, e per diverse definizioni di curvatura. Per le particolari condizioni al contorno scelte (trave incernierata – semplicemente appoggiata con una molla assiale), é stato utilizzato il metodo alle scale temporali multiple (*multiple time-scales*) per cogliere i differenti fenomeni dinamici nel sistema, dove le vibrazioni dinamiche libere e forzate con smorzamento sono rappresentate rispettivamente da curve backbone e da curve non lineari di risposta in frequenza. In questo lavoro sono state accoppiate vibrazioni longitudinali e trasversali, mostrando ed analizzando l'importanza dell'interazione di due modi, ad esempio per fenomeni di risonanze interne. I risultati analitici sono state integrati con un modello numerico realizzato nel software commerciale Abaqus_CAE®. Inizialmente, il comportamento lineare del modello della trave é stato esaminato nel modulo in *frequenza* e successivamente, utilizzando il modulo *dinamico esplicito*, sono state ottenute le curve backbone e le curve non lineari di risposta in frequenza stabili. Le simulazioni numeriche hanno usato i metodi di *path-following* e *shooting*. I risultati delle simulazioni sono stati confrontati con le soluzioni analitiche e dimostrano la conformità di entrambi i metodi. Oltre alle sofisticate analisi teoriche, sono stati effettuati alcuni test preliminari di laboratorio su un prototipo di trave di Eulero-Bernoulli al variare delle condizioni al contorno in direzione longitudinale. La dinamica della struttura reale è stata testata sperimentalmente forzando il sistema cinematicamente nella direzione trasversale con diverse ampiezze di eccitazione e condizioni al contorno. Sono stati osservati fenomeni di non linearitá quali hardening e softening e salti tra soluzioni stabili. Tali effetti sono stati riscontrati sia negli studi analitici sia in quelli numerici, nonché negli esperimenti sul prototipo. Infine, il lavoro é completato dalle conclusioni e dai possibili sviluppi futuri del problema.

Streszczenie

W pracy doktorskiej dokonano analizy dynamiki nieliniowej belki. W układzie płaskim wyprowadzono cząstkowe równania różniczkowe ruchu, biorąc pod uwagę efekty rozciągania i zginania ze ścinaniem bezwładność wzdłużną, poprzeczną i obrotową; a także różne definicje krzywizny. Uwzględniając wybrane warunki brzegowe (belka swobodnie podparta z poosiowym elastycznym elementem), zastosowano metodę wielu skal czasowych i zbadano różne zjawiska dynamiczne w układzie. Na podstawie uzyskanych rozwiązań analitycznych wyznaczono drgania swobodne oraz wymuszone badanej struktury oraz krzywe szkieletowe i nieliniowej charakterystyki amplitudowo częstotliwościowe. W pracy wykazano możliwość sprzężenia drgań wzdłużnych i poprzecznych, a następnie przeprowadzono analizę interakcji dwóch postaci drgań. Rozważania analityczne zostały uzupełnione przez model numeryczny wykonany w komercyjnym oprogramowaniu Abaqus_CAE®. Na początku zbadano dynamikę układu w zakresie liniowym w module *frequency*, a następnie wykorzystując modułu *dynamic explicit* wyznaczono krzywe szkieletowe oraz narysowano wykresy stabilnych odpowiedzi amplitudowo-częstotliwościowej. W obliczeniach zastosowano metodę *strzelania* oraz metodę *podążania za ścieżką stabilnego rozwiązania*. Wyniki porównano z rozwiązaniami analitycznymi wykazując zgodność obu metod. Oprócz wyrafinowanych teoretycznych analiz wykonano stanowisko laboratoryjne uwzględniające smukłą belkę i zmienne warunki brzegowe w kierunku wzdłużnym. Dynamika rzeczywistej struktury została zbadana eksperymentalnie wymuszając układ kinematycznie w kierunku poprzecznym z różnymi amplitudami wymuszenia oraz warunkami brzegowymi. Zjawiska nieliniowości obserwowano w postaci sztywnych i miękkich charakterystyk rezonansowych oraz przeskoków między stabilnymi rozwiązaniami. Efekty zostały zaobserwowane w badaniach analitycznych i numerycznych, a także w eksperymencie. Pracę zakończono wnioskami i planowanym przyszłym rozwojem zagadnienia.

Contents

List of Figures

List of Tables

Chapter 1

Introduction

Cables, beams and shells are the most common structural elements in engineering. They are used in large-scale to design buildings, bridges; are indispensable automotive components; at the micro-scale are used every day in sensors and controllers in cell phones and many other devices. Beams and shells are subjected to optimization and wise solutions are often proposed for design purposes. This requires careful theoretical and experimental examination.

The development of modern structures requires scientific description with more and more accurate mathematical models. Their behaviour is described with high accuracy in various dynamical conditions. Nowadays, a lot of attention is paid to nonlinear dynamics of those structures, for example beams under different boundary conditions, like clamped-clamped, cantilever, hinged-hinged, hinged-simply supported and so on. Despite the complexity of the problems, advanced software for mathematical manipulations, and more powerful hardware, allow us to analytically attack those models, by covering all geometrical effects and associated complex nonlinear and non-homogeneous dynamic boundary conditions. We will study a particular case of a beam with arbitrary boundary conditions in axial direction and we will consider the dynamic behaviour of such a system with three different approaches: numerical, analytical and experimental.

1.1 Motivation

In real structures ideal constraints (i.e. those that exactly eliminate the displacements or rotations) do not exist; for example constraints of the hinges, a beam has susceptibility to deformation and can be reduced to sliding support with a robust axial elastic element. It is well known that nonlinear dynamics of any structure depends on initial and boundary conditions, and it is worth to check how the axial spring stiffness changes the behaviour of the new arrangement. As it will be shown in Section 1.3 there are only a few publications on this topic and therefore the expected rich nonlinear dynamics of the system as well as its applicability motivated us to work on it.

Second, equally important motivation is the coupling between axial and transversal displacements. Commonly, the differential equations of motion which describe vibrations of the beam are focused only on lateral displacements and associated bending-shearing deformations. The simultaneous consideration of the longitudinal and transverse terms of the beam increases the level of difficulty of the problem. However, it shows the importance of interactions, which for some cases can be omitted and in critical parameters they completely change the behaviour of the structure.

1.2 Objectives

The objectives of the work are:

- to accurately derive the partial differential equations of motion for a simply supported beam with particular consideration of various boundary conditions in longitudinal direction and their effects on dynamical response;
- to propose several strategies, based on finite element method, for free and forced-damped nonlinear dynamics investigation of the mechanical systems;
- to properly design an experimental prototype beam, to subject it to large amplitude vibrations together with multifarious longitudinal elastic supports of the system;
- to compare analytical, numerical and experimental results
- to examine sensitivity of the parametric response of the beam to small variations for design purposes,
- to analytically, numerically and experimentally detect variations in hardening/softening dichotomy.

1.3 State of the art - beams dynamics

Origins of the study on beams dynamics is dated back to 1654-1782 to Jacob and Daniel Bernoulli. Jacob realized that the curvature of deformed beam is proportional to bending moment along the spam, while his nephew, Daniel derived the differential equation of motion for an oscillating beam. Their extravagant at that time model was examined by Leonard Euler by cross checking various conditions of loading and related to them deformation shapes [1]. The established beam model is the most common one and recognized under different names: *classical beam theorem*, the *Euler-Bernoulli beam theory*, *Euler*

beam theory or *Bernoulli beam theory*. The Euler-Bernoulli beam links bending curvature-bending moment relation and is the simplest theorem commonly used in engineering. The balance of strain energy due to bending and kinetic energies due to transverse speed gives relatively good results for low modes of slender beams. Higher order modes reduces length of the half-waves as in case of thick (non-slender) beams where other effects becomes stronger. The historical draft of the Euler-Bernoulli beam and derivation can be found in many well recognizable books for example [2–8].

The first improvement of classical beam theory was proposed by Rayleigh in 1877 [9]. He observed that the angular displacement of the beam element is a lateral deformation derivative, infinitesimally small with respect to the infinitesimally small beam element. The angular speed is a derivative of angular deformation with respect to time. Then, by multiplying the square of angular velocity by a half of inertia of the segment and integrating those terms over beam lenght gives a kinetic energy, which correspond to rotatory inertia. In other words, he took into account the effect of beam cross-section rotational inertia which supplement the kinetic energy [10]. In 1937 [11], the *Rayleigh beam* model was used to study fixed-free conditions.

The Rayleigh beam theorem was extended by Timoshenko in 1921 [12] and 1922 [13]. To the Euler-Bernoulli beam a shearing and rotation effects were implemented, this improvement highlights differences for higher order modes of oscillations as well as thick beam and remains fully compatible with results for slender beams. Over the time the Timoshenko beam gained popularity becoming the reference for non-slender beams.

Kruszewski performed theoretical analysis of the cantilever and free-free beams using Timoshenko teorem for the first three modes [14]. Traill-Nash and Collar distinguished five boundary conditions and analyzed beams dynamics under combined arrangement as follows: cantilever, free-free (symmetric and anti-symmetric modes), simply supported-free, simply supported (symmetric and anti-symmetric modes), clamped-clamped (symmetric and anti-symmetric modes). Authors also considered more general study but with simplifaications by neglecting rotatory inertia or assuming infinite shear stiffness. They validated results experimentally and numerically for non-slender beams, Table 1.1 shows investigation discrepancies [10].

In [15], Herrmann investigated forced Timoshenko beams by reducing general problem of forced motion to free vibration problem. Based on orthogonality of the principal modes the problem has been resolved with time-dependent boundary conditions by Mindlin and Goodman [16, 17]. Study on beams dynamics aroused increasing interest, for example, Dolph analyzed hinged-hinged and free-free shearable beams including rotatory inertia in dimensionless form [18]. Huang compared classical beam vs Timoshenko model for clamped-free beam

Table 1.1: Experiment vs theoretical beam models: comparison of natural frequencies for non-slender beams [10].

Beam models	First natural Frequency	Second natural frequency
Euler-Bernoulli	from +14% to +26%	from +78% to +133%
Timoshenko	from −1% to +2%	from −1% to +6%

and drawn dimensionless correction in natural frequencies as a radius of gyration function [19].

A discussion on the shear coefficient in Timoshenko's beam theory for different cross-sections has been done by Cowper, in [20].

Dawson presented approximate bending and shear deflections using a series of simple beam functions. For this purpose he used Rayleigh-Ritz method and compared it to analytical solutions for the five bending modes of Timoshenko beam. He concluded that his method can be extended to initially twisted beams, for which an analytical solution does not exist [21]. Indeed, next year, together with Carnegie, he reported natural frequencies and associated modal shapes of pre-twisted cross section along the length up to 90 degrees for first three bending modes [22].

The effect of shear flexibility and rotatory inertia on the natural frequencies of uniform beams was captured in an energy approach by Carr for hinged-hinged, fixed-free, free-free, fixed-fixed, fixed-hinged and free-hinged beams [23]. He omitted the difficulty of using simple functions by linking the shear flexibility and the effect of rotatory inertia relations. That approximation hardly changes the natural frequencies with respect to the exact solutions obtained by transcendental frequency equations for higher modes.

Atluri reconsidered Timoshenko beam model and introduced to nonlinear equations of motion terms which arise from longitudinal and rotatory inertia, caused by large amplitudes of oscillations. Dynamics of hinged beam with no axial restraints was considered by using Galerkin method and modal expansion [24]. He applied the perturbation procedure of multiple time-scales to derive frequency-amplitude relations and proved that nonlinear natural frequency decreases as the amplitude of oscillations increases in the hinged-simply supported beam, contrary to previous works which neglected the axial inertia effect [25–28]. Also Mei built, incorrect for this purpose, a finite element model of large displacements [29,30]. Prathap and Varadan drew conclusions from the errors of their predecessors and formulated the classical problem of the large

amplitude transverse vibration considering key inertia terms for a hinged beam with axial restraints (hinged-hinged). They used the exact nonlinear curvature expressions, nonlinear equilibrium equations and not averaged axial force generated due to immovability of supports. Although, they ignored longitudinal inertia forces to simplify analysis, of course this assumption has a much lower impact on the hinged-hinged beam's dynamics than in the case of a simply supported beam [31]. Simultaneously, Crespo da Silva and Glynn went over the formulation in a planar system and dealt with flexural-flexural-torsional modes of inextensible beams [32]. Using perturbation analysis the nonlinear frequency response curves were drawn for the first, second and third modes of a cantilever beam [33].

Two years later, Hutchinson was exploring an exact solution for the natural frequencies of solid elastic cylinders in free configuration [34]. He described the problem by three-dimensional equations considering radial, tangential and axial displacements, and then plotted frequency spectra of even and odd modes in diameter to lenght ratio-natural frequency and compared with experiments reported by [35]. Results were in a very good agreement. Next, he extended his work to comparison of Euler-Bernoulli and Timoshenko beams exact solutions in free-free configuration with an Pochhammer-Chree approximate solutions [36] and reconsidered a shear coefficient in diameter-to-length, Poisson's ratio and frequency relations.

From our point of view, Luongo et al. presented very interesting research on nonlinear dynamics of planar shear-indeformable as well as shear-deformable beams in 1986 and 1987 [37, 38]. Latter investigation were preceded by several considerations on the free nonplanar vibrations of inextensional beams [39] and planar unshearable beams [40]. They employed perturbation method for among others hinged-hinged and hinged-simply supported beams in the neighborhood of the resonant frequencies (first and third) and drawn frequency response curves distinguishing stable and unstable solutions. As in [24], their examination shows hardening and softening phenomena for axially restrained and unrestrained beams, respectively.

After a decade, Crespo Da Silva returned with a reconsidered classical beam model wherein flexure along two principal directions, torsion and extension are formulated. The shearing effect due to bending was neglected. Effects of all geometric nonlinearities, which arise from mid-plane stretching, *mechanical* curvature as well as *inertia* terms were considered in [41] and then applied to variational approach to obtain equations of motion and boundary conditions associated with them. Consequently the nonlinear response of clamped-clamped and clamped-hinged beams were determined using perturbation analysis [42]. Due to method restrictions distance between reinforcements had been restrained. Nevertheless, nonlinear inertia and curvature in the analysis were

involved in the nonlinear analysis.

In the late XX and beginning of the XXI centuries scientists were focused on possibilities of nonlinear response using beam-like systems. Various already established methods were applied to achieve more attractive dynamics of the structures and to obtain full control over structures as:

- Beams application in micro-electro-mechanical systems e.g. electromechanical switches [43]; coupling linear and nonlinear elastic forces with the nonlinear electric forces generated by the capacitors to study static and dynamic behaiour of the devices [44]; inspection on different beam shapes for piezoelectric energy harvesting [45]; and mode localization of two doubly clamped microbeams with mechanical link [46].

- Rotating structures, wherein a canteliever beam with coupled through the stretch/chordwise deformations and weak linearly uncoupled flapwise deformations [47]; consideration on the preset angle of the beam and nonconstant angular speed [48] and a tip mass [49]; vibration control of rotating composite beams and blades [50].

- Health morthing of beam-type and plate-type structures using natural frequencies methods, corresponding mode shapes, curvature mode shape methods and combined method [51]. It enables damage detection, localize and investigate the value of the defect [52, 53].

- Interaction between bending modes for initially straight, buckled or moderately curved beams [54–57]. For example, Avramov et al. studied nonlinear strain-displacement model of hinhed-hinged beam with periodic lateral force. They applied the multiple time scales method to the system and inspected almost-periodic beam oscillations, bifurcation diagrams and Poincare sections in [54]. In [55], Lacarbonara and Rega investigated two-to-one, three-to-one and one-to-one internal resonance of the one-dimensional slender beam which was buckled by prescribed end-displacement. They were focused on analysis of integer ratios between eigenfrequencies of clamped–clamped buckled beams as well as suspended cables, and then determined cases where the non-linear interactions which might trig resonant non-linear normal modes. Emam and Nayfeh also considered clamped-clamed beam, but in their approach the axial static load (beyound the critical value) initially deformed beam and transverse harmonic excitation were imposed around the primary resonance. They detected orbits of period -one; -two; -four; -eight; and snaptrough motion in [56]. Next Lacarbonara et al. considered the kinematically excited, imperfect curved hinged-hinged beam with a torsional spring subjected to one end [57]. Two main parameters were varied (tor-

sional spring stiffness and amplitude of initial half-sinusoidal deformation in rest configuration) to find flexural modal interactions and then display mode shapes functions, frequency force curves of one-to-one auto parametric resonance of the first two modes and particular cases of weakly localized responses.

- Effect of additional mass on the beams dynamics [49, 58–60]. Pakdemitli and Nayfeh analyzed a hinged-hinged beam with a grounded spring-mass system attached to the beam along the spam [58]. They used two perturbation approaches: averaging Lagrangian over the fast time scale then derived the modulation equations and the method of multiple time scales applied directly to the partial differential equations together with associated boundary conditions. Using both methods they analyzed the lowest five linear natural frequencies for selected mass-spring suspensions and then nonlinear responses of the lowest two frequencies of the structure were investigated for a free and forced-damped oscillations. Whereas, Lacarbonara and Camillacci analysed nonlinear normal modes of the hinged-hinged beam undergoing axis streching and carrying the lumped mass in [59]. Cubic inertia and weak cubic geometrical nonlinearities were assumed in the beam model and analysis was performed in two cases (i) away from internal resonances and (ii) near to three-to-one internal resonances. Parametric resonances of the unshearable and inextensible simply supported beams with tip mas were analyzed with use of the multiple time scales method and compared with experimental results in [60]. Authors highlighted that increase of the tip mass produced a more pronounced softening effect in simply supported beam, it was in contrary to behaviour of a cantilever beam. Moreover, they observed single-mode nonperiodic behaviors near the particular boundary of the resonance tongue, which were particularly interesting from mechanical point of view.

- Stretching forces in simply supported beams. The axial forces imposed by small deflection of boundary conditions affects natural frequencies which decrease for odd modes, while for even modes can either increase or decrease [61]. In case of the hinged-hinged beams, the response of the slighty streached beam has demonstrated hardening behaviour [62].

In recent years novelty on coupling in transverse-longitudinal vibrations of hinged-simply supported beams with an axial spring was developed by two research groups. The first led by Yabuno, Lacarbonara et al. explored knowledge about excited beams [63–66]. Three models of a planar beams-spring system, excited by kinematic excitation were studied analytically and experimentally in [63]. The frequency response curves of the hinged-hinged and hinged-simply

supported beam represented hardening and softening behaviour for the first bending mode, respectively. Particularly those experiments, by testing different spring stiffness will be extended in Chapter 4 of the thesis. Next, in [64] the hinged-singed beam with time-varying horizontal displacement of the one end were dynamically tested by finite element method for different axial to flexural stiffness ratios. In the next approach the beams' tip was also axially excited (via periodic motion of a shaker's head), where the sliding support was linked by a linear spring. The *passive control* method for changing the nonlinear characteristics of the frequency response curve by a change of spring stiffnes without shifting the linear unstable region were proposed in [65]. Finally, the hinged-simply supported beam-spring-tip mas system was mounted on sliding trolley and then excited by periodic movement of the slip table in the axial direction. They highlighted that third-order analysis based on the multiple time scales is not able to quantitatively capture the frequency response curves of the structure and therefore they introduced a fifth-order analysis to get results coherent with experiment.

Since 2016, nonlinear free vibrations, various curvature definitions, analytical, numerical and experimental methods were dealt with by Lenci and Rega et al. [67–78]. They started from deriving a set of partial differential equations of motion and associated boundary conditions based on a linear elastic behaviour of the material, kinematic of shearable and extensible beam element, and balance equations including axial, transversal and rotatory inertia. Using perturbation methods, they investigated the free oscillations for the first bending mode by neglecting axial displacements in linear order equations in [67] and including them in nonlinear coupled axial-transverse motion [68]. The analytical model was validated with use of the finite element simulations by comparing backbone curves in [70]. Discrepancies in the system responses based on different curvature definitions (mechanical and geometric) were examined in [71]. Free and forced oscillations of the simply supported beam with boundary conditions like inclined (linear) roller at the free end with no spring were considered in [72] and also isochronous beam with inclined support sliding on an arbitrary path were developed in [73]. In subsequent the path following finite element method [74, 75] and the multiple time scale method [76] were used in studies on forced-damped nonlinear oscillations of the planar, initially straight beam with an axial spring for the primary resonance as well as higher order resonances [77]. The most recent work is on experimental test and its finite element method counterpart is presented in [78] and through this doctoral thesis, nonetheless development on this topic is still in progress.

The thesis is organized as follows. In Chapter 2 the multiple time scales method up to third order of approximation is applied directly to the coupled partial differential equations of motion of the Timoshenko beam with associated

boundary conditions. Numerical model is performed in Chapter 3 and includes four numerical methods of analyzing the beams dynamic: free linear oscillations, nonlinear oscillations based on time histories, path following and shooting methods implemented for forced-damped vibrations (explicit in simulation time). The experimental test of the kinematically excited beam is reported in Chapter 4 and collectively results for analytic, numeric and experiment are compared in Chapter 5. The thesis ends in Chapter 6 with conclusions, the advantage of studies and future developments .

Chapter 2

Analytical approach

In this chapter analytical modeling of the beam will be presented, wherein linear behaviour, balance and geometrical nonlinearities are combined in order to derive an exact planar beam model, described by a set of three partial differential equations of motion. Origin of the most general case of a finite length beam is presented in Section 2.1. In Section 2.1.2 considerations will be devoted to various types of boundary conditions and finally a perturbation method will be applied to the beam model under hinged-simply supported type of boundary conditions. Analytical part will be summarized by frequency response and backbone curves together with a discussion on higher order resonances of beams.

2.1 Beam model

2.1.1 Beam element definition

Let us consider an initially straight beam of length L ($0 < Z \leq L$) in rest configuration, with a constant cross section A and second order of area J. Beam's linear elastic material properties are defined by: Young modulus E, density ρ and shear modulus G. Parameter G implies that Poisson's ratio ν and shear factor ξ are also invariable.

The beam element is placed in a plane described by two orthogonal axes Z, X. The displacements are dependent on time T. Initially undeformed configuration is along the Z axis, its deformation in (Z, X) plane is defined by $W(Z,T)$ and $U(Z,T)$ displacements. A cross section of the beam can also rotate of an angle $\theta(Z,T)$, see Figure 2.1. By analyzing kinematics of the beam element we find that:

- the axial stretch of elementary segment S' and the axial strain $\hat{e}$ are

$$S' = \sqrt{(1+W')^2 + U'^2}, \quad \hat{e} = S' - 1. \tag{2.1}$$

  where primes denote partial derivative with respect to the coordinate Z,

- the slope angle φ satisfies

$$\cos\varphi = \frac{1+W'}{S'}, \quad \sin\varphi = \frac{U'}{S'}, \quad \tan\varphi = \frac{U'}{1+W'}, \tag{2.2}$$

- the shear strain γ is described as a difference between slope angle and rotation of cross section of the beam element

$$\gamma = \theta - \varphi. \tag{2.3}$$

  The beam model can be devoid of shear effect in case $\gamma = 0$. It will not be studied here. In our analytical studies only shearable beams ($\gamma \neq 0$) will be investigated. A generalized formula captures both slender and non-slender structures.

Two different definitions of a curvature can be assumed; first, the most commonly used is the *mechanical* curvature

$$k_m = \frac{d\theta}{dZ} = \theta', \tag{2.4}$$

second, more general description is the *geometrical* curvature [6, 69, 79, 80], which can be written as follow

$$k_g = \frac{d\theta}{dS} = \frac{\theta'}{S'} = \frac{\theta'}{\sqrt{(1+W')^2 + U'^2}}. \tag{2.5}$$

For inextensible beams S'=1, and thus geometrical and mechanical curvatures coincide for both shearable as well as unshearable beams. Thus, for small elongation k_m and k_g are close. However, as lateral deformation increases curvatures k_m and k_g differ. In this work we apply the definition of curvature k_g to a beam model which brings nonlinearities to the system, and is appropriate for a large amplitudes of coupled axial-transversal oscillations of the beam.

The constitutive law is assumed to be linear elastic, without coupling between different deformations:

- axial force - along the deformed beam element, related to axial stiffness EA and elongation strain

$$N = EA\hat{e}; \tag{2.6}$$

- shear force - perpendicular to the distorted segment, product of shear strain and shear stiffness GA

$$V = GA\gamma; \tag{2.7}$$

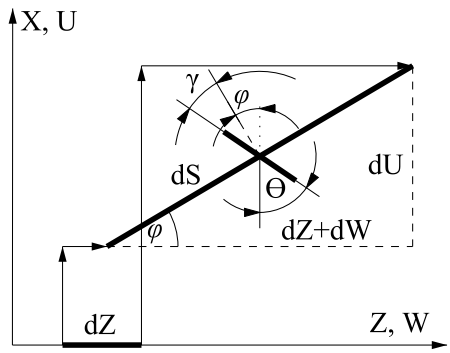

Figure 2.1: Kinematics of extensible-shearable beam element [76].

- bending moment given by curvature strain multiplied by bending stiffness EJ

$$M = EJk_g. \tag{2.8}$$

The previous constitutive laws imply that the only nonlinearities are of geometrical nature.

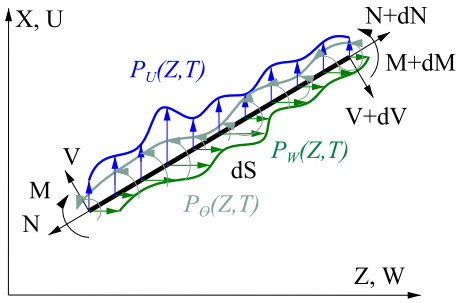

Figure 2.2: Coplanar forces of the deformed beam element [76].

Figure 2.2 presents forces acting on the beam element. When the strain forces and external forces are decomposed along the three coordinates horizontal, vertical and rotational. They give the following equilibrium (balance) equations:

$$(N\cos\varphi + V\sin\varphi)' = \rho A\ddot{W} + C_W\dot{W} + P_W(Z,T), \tag{2.9}$$

$$(N\sin\varphi - V\cos\varphi)' = \rho A\ddot{U} + C_U\dot{U} + P_U(Z,T), \tag{2.10}$$

$$M' - VS' = \rho J\ddot{\theta} + C_\theta\dot{\theta} + P_\theta(Z,T), \tag{2.11}$$

where dot ($\dot{}$) corresponds to time derivative $\frac{\partial()}{\partial T}$. C_W, C_U and C_θ are linear viscous damping coefficients, they can be extended to higher order nonlinearity for some purposes [81–85]. $P_W(Z,T)$, $P_U(Z,T)$, $P_\theta(Z,T)$ are time dependent external excitations. Material property ρA is mass per unit length in rest configuration and ρJ depicts second moment of inertia of the cross-section of undeformed beam. A set of material properties EA, GA, EJ, ρA and ρJ is constant in the rest reference configuration.

Substituting equations (2.1)-(2.3), (2.5) and (2.6)-(2.8) into (2.9)-(2.11) we obtain a set of partial differential equations of motion of the exact planar beam model

$$\begin{aligned}\rho A\ddot{W} + C_W\dot{W} + P_W(Z,T) = \\ \left\{ EA\left[\sqrt{(1+W')^2+U'^2}-1\right]\frac{1+W'}{\sqrt{(1+W')^2+U'^2}} \right. \\ \left. +GA\left[\theta-\arctan\left(\frac{U'}{1+W'}\right)\right]\frac{U'}{\sqrt{(1+W')^2+U'^2}} \right\}', \end{aligned} \tag{2.12}$$

$$\begin{aligned}\rho A\ddot{U} + C_U\dot{U} + P_U(Z,T) = \\ \left\{ EA\left[\sqrt{(1+W')^2+U'^2}-1\right]\frac{U'}{\sqrt{(1+W')^2+U'^2}} \right. \\ \left. -GA\left[\theta-\arctan\left(\frac{U'}{1+W'}\right)\right]\frac{1+W'}{\sqrt{(1+W')^2+U'^2}} \right\}', \end{aligned} \tag{2.13}$$

$$\begin{aligned}\rho J\ddot{\theta} + C_\theta\dot{\theta} + P_\theta(Z,T) = \left(EJ\frac{\theta'}{\sqrt{(1+W')^2+U'^2}} \right)' \\ -GA\left[\theta-\arctan\left(\frac{U'}{1+W'}\right)\right]\sqrt{(1+W')^2+U'^2}. \end{aligned} \tag{2.14}$$

The above presented planar beam model is exact and includes [76]:

- axial, bending and shear deformations;
- axial, transversal and rotatory inertia;
- *geometrical* (not mechanical) curvature [71, 79];

- external forces and damping.

The proposed planar model is almost geometrically exact, the only simplifications are plain deformation of the cross-section and disregard of the transverse strain. In Section 2.1.2 the boundary conditions will be introduced. Afterward their nonlinear dynamics will be analytically examined by the perturbation method in Section 2.2.

2.1.2 Boundary conditions

Scleronomic constraints

Boundary conditions of beams constraint position, angle by reacting force or momentum. For example eliminaring the lateral displacement of the beam end is called *simply supported*, while the blockade of lateral and longitudinal displacement is named *hinge*. Restriction of rotation and displacement in axial and transverse directions is the *clamped* boundary condition. Latter three types of boundary conditions are scleronomic - independent of time [86]. Those scenarios can be used to define a lot of conditions of the beams, like: clamped-clamped, clamped-hinged, clamped-simply supported, clamped-free (cantilever beam), hinged-hinged, hinged-simply supported and hinged-free (rotating structure).

Rheonomic constraints

Whereas, rheonomic bounds are dependent on time and they cover boundary conditions related to additional components of the system like inertia, spring, damper or defined by time-dependent function of the beam point position or equivalent. Combinations of scleronomic and rheonomic boundary conditions have numerous schemes.

We are interested in investigating the nonlinear dynamics of the beam with one end hinged and the second end simply supported with an additional axial spring. The system is shown in Figure 2.3, where dashed (solid) thick line represents initially straight (deformed) beam. Lateral beam's deflection causes support movement in $-Z$ direction, which means tip deformation and spring extension. The linear elastic element with stiffness k_s is axially grounded. Note that the system has the symmetry axis $X = 0$. Considerable stiffness of the spring causes the bigger resistance to axial shortening of the system. Three different cases for $Z = L$ are possible for the considered configuration:

- $k_s = 0$: axially unrestrained beam, the end is free to move horizontally;
- $k_s = \infty \quad \rightarrow \quad W(L,T) = 0$: axially restrained beam, hinged;
- $0 < k_s < 0$: movable/axially unrestrained beam, supported-spring node.

Without losing generality ($0 \leq k_s \leq 0$), boundary conditions of the beam-spring system are

$$U(0,T) = 0, \quad U(L,T) = 0, \tag{2.15}$$

$$M(0,T) = 0, \quad M(L,T) = 0, \tag{2.16}$$

$$W(0,T) = 0, \quad N(L,T)\cos\varphi + V(L,T)\sin\varphi + W(L,T)k_s = 0. \tag{2.17}$$

Recalling equations (2.5) and (2.8), assumption of momentum absence at the ends can be expressed in the form:

$$\theta'(0,T) = 0, \quad \theta'(L,T) = 0. \tag{2.18}$$

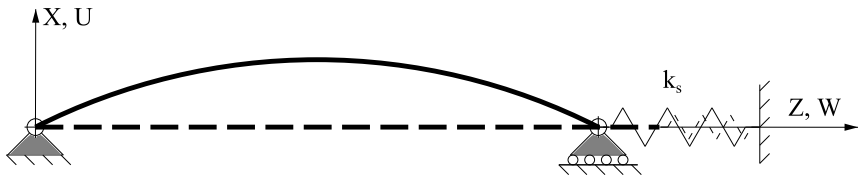

Figure 2.3: Configuration of the beam-spring system.

The dynamics of provided analytical model of the beam in Section 2.1.1 together with foregoing boundary conditions will be studied thoroughly in Section 2.2.

2.2 Multiple time-scales method

In this section, we study analytically by multiple time-scales method the nonlinear resonance phenomenon, which occurs when the frequency of excitation is near the nth linear (transversal) frequency of the beam, corresponding to a bending mode. For example, the multiple time-scales can be related to measurements with different sampling rate of office temperature. The first time-scale t_0 corresponds to the temperature change every hour. If we look at it in a week interval, temperature early morning is the lowest then increases to the warmest moment of the day (afternoon) and then decreases (daily oscillation), see Fig. 2.4a. Variation of temperature is repeatable. When the measurement is recorded once a week, for the highest daily temperature, it also changes

on yearly domain as displayed in Fig. 2.4b (slow time-scale t_1). Differences are caused by changes in the season: winter, spring, summer, autumn and again from the beginning. Slower time-scales could correspond to the maximum yearly temperatures recorded over a period of decades t_2, centuries t_3, millenium t_4 and so on (Fig. 2.4c).

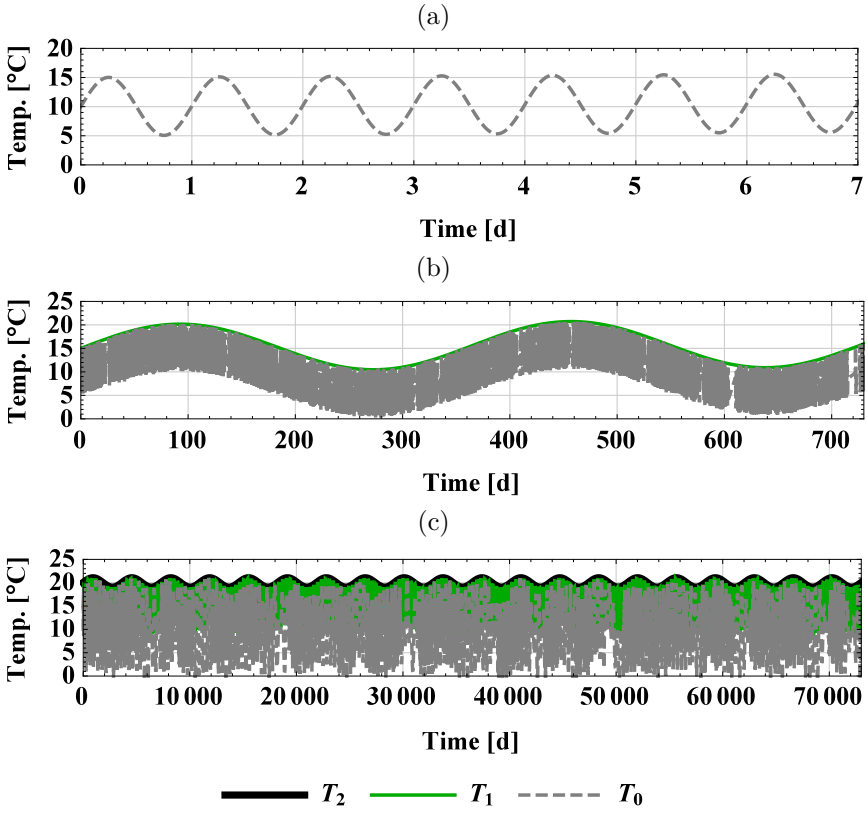

Figure 2.4: Temperature change in different time scales T_0, T_1, T_2.

Now, we are interested in employing the perturbation method in the considered structure, in particular in applying it directly to the set of three partial differential equations of motion (2.12)-(2.14) and associated boundary conditions (2.15)-(2.18). In brief the method can be described as follows. A prerequisite is the expansion of the sought solution in Taylor series, then multiple time-scales are introduced. First, the fast time-scale and then gradually slower scales, that allows to describe behaviour of certain phenomena after long transients are introduced. In practice it may happen that some terms (e.g. forcing-damping) can be reorganized and moved to higher order terms of expansion. In subsequent stages, partial differential equations, transformed into ordinary differen-

tial equations are ordered by the power of perturbation. Then, the problem is solved, step by step, accordingly to successive time-scales (each problem of higher order is based on previous, lower solutions). In the calculation process, secular generating terms have to vanish. For this purpose solvability conditions must be implemented. Computations end with modulation equations or frequency response curves and graphical representation of results [6, 87–92].

Following above-established rules, we consistently expand partial differential equations of motion (2.12)-(2.14) and boundary conditions associated with them (2.15)-(2.17) in Taylor series up to the third order perturbation terms:

$$\rho A\ddot{W} + C_W\dot{W} + P_W(Z,T) = EA\left(W' + \frac{1}{2}U'^2 - U'^2W'\right)' + \\ +GA\left(U'\theta - U'^2 + 2U'^2W' - U'W'\theta\right)', \tag{2.19}$$

$$\rho A\ddot{U} + C_U\dot{U} + P_U(Z,T) = EA\left(U'W' + \frac{1}{2}U'^3 - U'W'^2\right)' + \\ +GA\left(U' - \theta - U'W' + \frac{1}{2}U'^2\theta - \frac{5}{6}U'^3 + U'W'^2\right)', \tag{2.20}$$

$$\rho J\ddot{\theta} + C_\theta\dot{\theta} + P_\theta(Z,T) = EJ\left(\theta' - W'\theta' - \frac{1}{2}U'^2\theta'\right)' + \\ +GA\left(U' - \theta - W'\theta - \frac{1}{2}U'^2\theta + \frac{1}{6}U'^3\right). \tag{2.21}$$

Boundary conditions are

$$U(0,T) = 0, \quad U(L,T) = 0, \tag{2.22}$$

$$M(0,T) = 0, \quad M(L,T) = 0, \tag{2.23}$$

$$W(0,T) = 0,$$
$$W(L,T)k_s + EA\left[W(L,T)' + \frac{1}{2}U'(L,T)^2 - U'(L,T)^2W(L,T)'\right] + \\ +GA\left[U(L,T)'\theta(L,T) - U(L,T)'^2 + 2U(L,T)'^2W(L,T)' \right. \\ \left. -U(L,T)'W(L,T)'\theta(L,T)\right] = 0. \tag{2.24}$$

Note that intention of using Taylor expansion is not approximation of the problem but approximation of the solution. However, we are aware that this procedure leads to an approximation of the beam model (up to the order of

expansion). In Sections 2.2.1 and 2.2.2 our attention will be paid to examples where natural frequencies of excitation is near the first flexural resonance as well as higher order modes.

For our problem we introduce the fast time-scale t_0 and two slow time-scales t_1 and t_2:

$$t_0 = T, \quad t_0 = \varepsilon T, \quad t_0 = \varepsilon^2 T, \tag{2.25}$$

where ε is a small *bookkeeping* parameter. Damping coefficients are manually shifted to ε^2 and the excitation terms to ε^3:

$$C_W = \varepsilon^2 c_W, \quad C_U = \varepsilon^2 c_U, \quad C_\theta = \varepsilon^2 c_\theta, \tag{2.26}$$

$$\begin{gathered} P_W(Z,T) = \varepsilon^3 \hat{p}_W(Z,T), \quad P_U(Z,T) = \varepsilon^3 \hat{p}_U(Z,T), \\ P_\theta(Z,T) = \varepsilon^3 \hat{p}_\theta(Z,T). \end{gathered} \tag{2.27}$$

As it will be seen, this maneuver moves the above-mentioned terms to the third order perturbation equations. At this moment we assume $\hat{p}_W(Z,T) = 0$ and $\hat{p}_\theta(Z,T) = 0$, as a consequence we limit external excitation only to X-direction and rewrite equation (2.27) in the form:

$$\varepsilon^3 \hat{p}_U(Z,T) = \varepsilon^3 P_v \delta\left(Z - \frac{L}{c_z}\right) \cos(\Omega T), \tag{2.28}$$

where Dirac delta $\delta\left(Z - \frac{L}{c_z}\right)$ is a space dependent function and $\cos(\Omega T)$ involves variation in time with frequency Ω. The P_v decribes amplitude of concentrated force applied to the beam at distance $\frac{L}{c_z}$ from the origin of the coordinate system in Z direction. Dimensionless constant c_z can vary from 1 to ∞. For example $c_z = 2$ defines concentrated force in midpoint, $c_z = 4$ moves it to quarter of the beam ($Z = 0.25L$), while $c_z = 1$ represents force applied to the beam's tip ($Z = L$) [93].

Solutions of the problem are sought up to third order in the forms:

$$W(Z,T) = \varepsilon W_1(Z,t_0,t_1,t_2) + \varepsilon^2 W_2(Z,t_0,t_1,t_2) + \varepsilon^3 W_3(Z,t_0,t_1,t_2), \tag{2.29}$$

$$U(Z,T) = \varepsilon U_1(Z,t_0,t_1,t_2) + \varepsilon^2 U_2(Z,t_0,t_1,t_2) + \varepsilon^3 U_3(Z,t_0,t_1,t_2), \tag{2.30}$$

$$\theta(Z,T) = \varepsilon \theta_1(Z,t_0,t_1,t_2) + \varepsilon^2 \theta_2(Z,t_0,t_1,t_2) + \varepsilon^3 \theta_3(Z,t_0,t_1,t_2). \tag{2.31}$$

Derivatives with respect to time T undergo a chain rule and can be written in the form:

$$\dot{W} = (D_0 + \varepsilon D_1 + \varepsilon^2 D_2)W, \tag{2.32}$$

$$\ddot{W} = (D_0^2 + 2\varepsilon D_0 D_1 + \varepsilon^2(2D_0 D_2 + D_1^2))W, \tag{2.33}$$

$$\dot{U} = (D_0 + \varepsilon D_1 + \varepsilon^2 D_2)U, \tag{2.34}$$

$$\ddot{U} = (D_0^2 + 2\varepsilon D_0 D_1 + \varepsilon^2(2D_0 D_2 + D_1^2))U, \tag{2.35}$$

$$\dot{\theta} = (D_0 + \varepsilon D_1 + \varepsilon^2 D_2)\theta, \tag{2.36}$$

$$\ddot{\theta} = (D_0^2 + 2\varepsilon D_0 D_1 + \varepsilon^2(2D_0 D_2 + D_1^2))\theta, \tag{2.37}$$

where D_j denotes $\frac{\partial}{\partial t_j}$ [88]. We substitute Eqs. (2.26), (2.28)-(2.37) into partial differential equations of motion (2.19)-(2.21) and associated boundary conditions (2.15)-(2.18), collect them in order of ε perturbation. As a consequence we obtain three sets of rearranged equations:

First order

$$EAW_1'' - \rho A D_0^2 W_1 = 0, \tag{2.38}$$

$$GA(U_1' - \theta_1)' - \rho A D_0^2 U_1 = 0, \tag{2.39}$$

$$EJ\theta_1'' - GA(\theta_1 - U_1') - \rho J D_0^2 \theta_1 = 0. \tag{2.40}$$

Boundary conditions:

$$U_1(0,T) = 0, \quad U_1(L,T) = 0, \quad \theta_1'(0,T) = 0, \quad \theta_1'(L,T) = 0, \quad W_1(0,T) = 0, \tag{2.41}$$

$$EAW_1'(L,T) + k_s W_1(L,T) = 0. \tag{2.42}$$

Second order

$$EAW_2'' - \rho A D_0^2 W_2 = 2\rho A\, D_0 D_1 W_1 - GA(\theta_1 U_1' - U_1'^2)' - \frac{1}{2} EA(U_1'^2)', \tag{2.43}$$

$$GA(U_2' - \theta_2)' - \rho A D_0^2 U_2 = \\ = 2\rho A D_0 D_1 U_1 - EA(U_1' W_1')' + GA(U_1' W_1')', \tag{2.44}$$

$$EJ\theta_2'' - GA(\theta_2 - U_2') - \rho J D_0^2 \theta_2 = \\ = 2\rho J D_0 D_1 \theta_1 + GA(W_1' \theta_1) + EJ(W_1' \theta_1')'. \tag{2.45}$$

Boundary conditions:

$$U_2(0,T) = 0, \quad U_2(L,T) = 0, \quad \theta_2'(0,T) = 0, \quad \theta_2'(L,T) = 0, \quad W_2(0,T) = 0, \tag{2.46}$$

$$EAW_2'(L,T) + k_s W_2(L,T) + \\ + \frac{1}{2} EAU_1'^2(L,T) - GA[U_1'^2(L,T) + \theta_1(L,T) U_1'(L,T)] = 0. \tag{2.47}$$

Third order

$$EAW_3'' - \rho A D_0^2 W_3 = c_W D_0 W_1 + \rho A(D_1^2 + 2D_0 D_2) W_1 + \\ + 2\rho A D_0 D_1 W_2 - EA(U_1' U_2' - U_1'^2 W_1')' + \\ - GA(2W_1' U_1'^2 + \theta_2 U_1' - 2U_2' U_1' - \theta_1 W_1' U_1' + \theta_1 U_2')', \tag{2.48}$$

$$GA(U_3' - \theta_3)' - \rho A D_0^2 U_3 = c_U D_0 U_1 + p_v \delta \left(Z - \frac{L}{c_z} \right) \cos(\Omega T) + \\ + \rho A(2D_0 D_2 + D_1^2) U_1 + 2\rho A D_0 D_1 U_2 + \\ + EA \left(U_1' W_1'^2 - U_1' W_2' - \frac{1}{2} U_1'^3 - U_2' W_1' \right)' + \\ + GA \left(-\frac{1}{2} \theta_1 U_1'^2 - U_1 W_1'^2 + U_1' W_2' + \frac{5}{6} U_1'^3 + U_2' W_1' \right)', \tag{2.49}$$

$$EJ\theta_3'' - GA(\theta_3 - U_3') - \rho J D_0^2 \theta_3 = c_\theta D_0 \theta_1 + \rho J \left(2D_0 D_2 + D_1^2 \right) \theta_1 + \\ + \rho J 2 D_0 D_1 \theta_2 + GA \left(\frac{1}{2} \theta_1 U_1'^2 - \frac{1}{6} U_1'^3 + \theta_2 W_1' + \theta_1 W_2' \right) + \\ + EJ \left(\frac{1}{2} \theta_1' U_1'^2 - \theta_1' W_1'^2 + \theta_2' W_1' + \theta_1' W_2' \right)'. \tag{2.50}$$

Boundary conditions:

$$U_3(0,T) = 0, \quad U_3(L,T) = 0, \quad \theta_3'(0,T) = 0, \quad \theta_3'(L,T) = 0, \quad W_3(0,T) = 0, \tag{2.51}$$

$$\begin{aligned} EAW_3'(L,T) + k_s W_3(L,T) + \\ +GA[-\theta_1(L,T)W_1'(L,T)U_1'(L,T) + \\ +\theta_2(L,T)U_1'(L,T) + U_2'(L,T)\theta_1(L,T)] + \\ +(EA-2GA)[U_2'(L,T)U_1'(L,T) - W_1'(L,T)U_1'^2(L,T)] = 0. \end{aligned} \tag{2.52}$$

2.2.1 Primary resonance

First order solution

The first order equations are constituted by two separate eigenvalue problems, which are independent (because to this order we are in the linear regime). The longitudinal problem involves the axial displacement W_1, while the bending is oriented in the transversal direction, and involves coupling between U_1 and θ_1. The solutions is represented by time and space dependent functions:

$$W_1(Z,t_0,t_1,t_2) = \left[\Lambda_{re}(t_1,t_2)e^{i\overline{\omega}_n t_0} + \Lambda_{im}(t_1,t_2)e^{-i\overline{\omega}_n t_0}\right]\hat{W}_{1,n}(Z), \tag{2.53}$$

$$U_1(Z,t_0,t_1,t_2) = \left[A_{re}(t_1,t_2)e^{i\omega_n t_0} + A_{im}(t_1,t_2)e^{-i\omega_n t_0}\right]\hat{U}_{1,n}(Z), \tag{2.54}$$

$$\theta_1(Z,t_0,t_1,t_2) = \left[A_{re}(t_1,t_2)e^{i\omega_n t_0} + A_{im}(t_1,t_2)e^{-i\omega_n t_0}\right]\hat{\theta}_{1,n}(Z), \tag{2.55}$$

Functions $\hat{W}_{1,n}(Z)$, $\hat{U}_{1,n}(Z)$ and $\hat{\theta}_{1,n}(Z)$ represent the nth modal shapes and are given by:

$$\hat{W}_{1,n}(Z) = \sin\left(s_n Z\right), \tag{2.56}$$

$$\hat{U}_{1,n}(Z) = \sin\left(\frac{n\pi Z}{L}\right), \quad \hat{\theta}_{1,n}(Z) = \left(\frac{n\pi}{L} - \frac{L\rho\omega_n^2}{\pi G n}\right)\cos\left(\frac{n\pi Z}{L}\right). \tag{2.57}$$

The nth circular frequencies of the system in the axial and transversal direction are given by, respectively,

$$\overline{\omega}_n^2 = s_n\sqrt{\frac{EA}{\rho A}}, \tag{2.58}$$

$$\omega_n^2 = \frac{AG}{2J\rho} + \frac{\pi^2 n^2(E+G)}{2L^2\rho} - \frac{\sqrt{[AGL^2+\pi^2 Jn^2(E+G)]^2 - 4\pi^4 EGJ^2 n^4}}{2JL^2\rho}, \tag{2.59}$$

where the parameter s_n is determined by the transcendental equation for the nth natural frequency (2.58) and corresponding mode shape (2.56). The trigonometric problem is related to boundary conditions (2.41)-(2.42) and is given by:

$$AEs_n \cos(s_n L) + k_s \sin(s_n L) = 0. \tag{2.60}$$

which is a consequence of the boundary conditions (2.41) and (2.42) applied to the modal shape (2.60). In this section we are focused only on primary resonance of the bending mode, thus to the first order solution lateral deformations are much larger than longitudinal ones. This is the same approach used in [69], and thus we assume:

$$W_1(Z,T) = 0, \tag{2.61}$$

This is reliable when the frequencies ratio is very high ($\frac{\overline{\omega}_n^2}{\omega_n^2} >> 1$), and reduces the difficulty of equations to solve. Note that, because of the rescaling (2.26) and (2.27), damping and external excitation do not appear in the equations of this order.

Second order solution

The second order equation (2.43) supplemented by (2.46)-(2.47) depends on different powers of frequency components as well as shape functions. The key to solve partial differential equations is to decompose frequencies of right hand side and then collect them. It allows to calculate derivative with respect to time t_0 and as a result reduce partial differential equation to ordinary differential equations, which are easy to solve. The result of the second order problem is a sum of solutions given by:

$$\begin{aligned} W_2(Z,t_0,t_1,t_2) = W_{2a}(Z,t_1,t_2) + W_{2b}(Z,t_1,t_2)e^{2i\omega_n t_0} + \\ + W_{2c}(Z,t_1,t_2)e^{-2i\omega_n t_0}, \end{aligned} \tag{2.62}$$

where

$$\begin{aligned} W_{2a}(Z,t_1,t_2) = -A_{im}(t_1,t_2)\, A_{re}(t_1,t_2)\left(En^2\pi^2 - 2L^2\rho\omega_n^2\right) \times \\ \times \frac{2n\pi Z + L\left(\frac{k_s L}{EA}+1\right)\sin\left(\frac{2n\pi Z}{L}\right)}{4EL^2 n\pi\left(\frac{k_s L}{EA}+1\right)}, \end{aligned} \tag{2.63}$$

$$W_{2b}(Z,t_1,t_2) = -\frac{A_{re}\left(t_1,t_2\right)^2\left(\pi^2En^2-2L^2\rho\omega_n^2\right)}{\sqrt{E}\frac{k_sL}{EA}\sin\left(\frac{2L\sqrt{\rho}\omega_n}{\sqrt{E}}\right)+2L\sqrt{\rho}\omega_n\cos\left(\frac{2L\sqrt{\rho}\omega_n}{\sqrt{E}}\right)}\times$$
$$\times\frac{1}{16\sqrt{E}L\left(En^2\pi^2-L^2\rho\omega_n^2\right)}\times\left[4\pi^2En^2\sin\left(\frac{2\sqrt{\rho}Z\omega_n}{\sqrt{E}}\right)+\right.$$
$$+2\pi E\frac{k_sL}{EA}n\sin\left(\frac{2\pi nZ}{L}\right)\sin\left(\frac{2L\sqrt{\rho}\omega_n}{\sqrt{E}}\right)-8\rho\omega_n^2L^2\sin\left(\frac{2\sqrt{\rho}Z\omega_n}{\sqrt{E}}\right)+$$
$$\left.+4\pi\sqrt{E}Ln\sqrt{\rho}\omega_n\sin\left(\frac{2\pi nZ}{L}\right)\cos\left(\frac{2L\sqrt{\rho}\omega_n}{\sqrt{E}}\right)\right], \quad (2.64)$$

$$W_{2c}(Z,t_1,t_2) = \frac{A_{im}\left(t_1,t_2\right)^2}{A_{re}\left(t_1,t_2\right)^2}W_{2b}(Z,t_1,t_2). \quad (2.65)$$

The second order equations (2.44)-(2.45) and related to them boundary conditions (2.46) depend on first slow time-scale t_1. The secular generating terms, which contains $e^{\pm i\omega_0t_0}$ must be eliminated. For this purpose the following solvability conditions are applied:

$$\int_0^L\left[GA\left(\widetilde{U}_2'-\widetilde{\theta}_2'\right)'-\rho AD_0^2\widetilde{U}_2\right]U_1dZ=\int_0^L\left(2\rho AD_0D_1U_1\right)U_1dZ, \quad (2.66)$$
$$\int_0^L\left[EJ\widetilde{\theta}_2''-GA\left(\widetilde{\theta}_2-\widetilde{U}_2'\right)-\rho JD_0^2\widetilde{\theta}_2\right]\theta_1dZ=\int_0^L\left(2\rho JD_0D_1\theta_1\right)\theta_1dZ. \quad (2.67)$$

integrating by parts

$$GA\widetilde{U}_2'U_1|_0^L-GA\widetilde{U}_2U_1'|_0^L-GA\widetilde{\theta}_2'U_1|_0^L+GA\widetilde{\theta}_2U_1'|_0^L+$$
$$\int_0^L\left[GA\left(\widetilde{U}_2U_1''-\widetilde{\theta}_2U_1''\right)-\rho AD_0^2\widetilde{U}_2U_1\right]dZ=$$
$$\int_0^L\left(2\rho AD_0D_1U_1\right)U_1dZ, \quad (2.68)$$
$$EJ\widetilde{\theta}_2'\theta_1|_0^L-EJ\widetilde{\theta}_2\theta_1'|_0^L+GA\widetilde{U}_2\theta_1|_0^L+$$
$$\int_0^L\left[EJ\widetilde{\theta}_2\theta_1''+GA\left(\widetilde{\theta}_2\theta_1-\widetilde{U}_2\theta_1'\right)-\rho JD_0^2\widetilde{\theta}_2\theta_1\right]\theta_1dZ=$$
$$\int_0^L\left(2\rho JD_0D_1\theta_1\right)\theta_1dZ. \quad (2.69)$$

Adding up Eqs. (2.68)-(2.69) and applying boundary conditions (2.46) then

collecting terms with respect to $\widetilde{U}_2$ and $\widetilde{\theta}_2$ we get:

$$\int_0^L \left[GA\left(U_1' - \theta_1'\right)' + \rho A\omega_n^2 U_1\right] \widetilde{U}_2 dZ + \int_0^L \left[EJ\theta_1'' - GA\left(\theta_1 - U_1'\right) + \rho J\omega_n^2\theta_1\right] \widetilde{\theta}_2 dZ = \int_0^L \left(2\rho A D_0 D_1 U_1\right) U_1 dZ + \int_0^L \left(2\rho J D_0 D_1\theta_1\right)\theta_1 dZ. \tag{2.70}$$

Note that functions in the square brackets are identical as Eqs. (2.39)-(2.40) in the first order (linear) problem and reduce left hand side

$$0 = \int_0^L \left(2\rho A D_0 D_1 U_1\right) U_1 dZ + \int_0^L \left(2\rho J D_0 D_1\theta_1\right)\theta_1 dZ. \tag{2.71}$$

It immediately gives

$$\frac{\partial A_{re}}{\partial t_1} = 0, \ \frac{\partial A_{im}}{\partial t_1} = 0, \tag{2.72}$$

consequently amplitudes do not depend on the slow time t_1, although they depend on second slow time-scale, $A_{re}(t_2)$ and $A_{im}(t_2)$.

Now equations (2.44)-(2.45) are simplified to

$$GA(\theta_2 - U_2')' + \rho A D_0^2 U_2 = 0, \tag{2.73}$$

$$EJ\theta_2'' - GA(\theta_2 - U_2') - \rho J D_0^2\theta_2 = 0, . \tag{2.74}$$

Solutions of these homogeneous equations are already presented in(2.54)-(2.55), thus we write second order solution:

$$U_2(Z, t_0, t_2) = 0, \quad \theta_2(Z, t_0, t_2) = 0. \tag{2.75}$$

Third order solution

In the third order solution, instead of solving equations (2.49)-(2.50), only $D_2 A_{re}(t_2)$ and $D_2 A_{im}(t_2)$ need to be determined. For this purpose, similarly

to second order solution, we apply following solvability conditions:

$$\int_0^L \left[GA\left(U_3' - \theta_3'\right)' - \rho A D_0^2 U_3\right] U_1 dZ = \int_0^L \left[\rho A 2 D_0 D_2 U_1 + GA\left(-\frac{1}{2}\theta_1 U_1'^2 + U_1' W_2' + \frac{5}{6}U_1'^3\right)' + EA\left(-U_1' W_2' - \frac{1}{2}U_1'^3\right)' + c_U D_0 U_1 + p_v \delta\left(Z - \frac{L}{c_z}\right)\cos\left(\Omega T\right)\right] U_1 dZ, \tag{2.76}$$

$$\int_0^L \left[EJ\theta_3'' - GA\left(\theta_3 - U_3'\right) - \rho J D_0^2 \theta_3\right] \theta_1 dZ = \int_0^L \left[\rho J 2 D_0 D_2 \theta_1 + GA\left(\frac{1}{2}\theta_1 U_1'^2 - \frac{1}{6}U_1'^3 + \theta_1 W_2'\right) + EJ\left(\frac{1}{2}\theta_1' U_1'^2 + \theta_1' W_2'\right)' + c_\theta D_0 \theta_1\right] \theta_1 dZ. \tag{2.77}$$

Reducing left hand side of Eqs. (2.76)-(2.77) by integrating by parts, substituting boundary conditions (2.51) and equations of the first order (2.39)-(2.40) we obtain

$$\int_0^L \left[\rho A 2 D_0 D_2 U_1 + GA\left(-\frac{1}{2}\theta_1 U_1'^2 + U_1' W_2' + \frac{5}{6}U_1'^3\right)' + EA\left(-U_1' W_2' - \frac{1}{2}U_1'^3\right)' + c_U D_0 U_1 + p_v \delta\left(Z - \frac{L}{c_z}\right)\cos\left(\Omega T\right)\right] U_1 dZ + \int_0^L \left[\rho J 2 D_0 D_2 \theta_1 + GA\left(\frac{1}{2}\theta_1 U_1'^2 - \frac{1}{6}U_1'^3 + \theta_1 W_2'\right) + EJ\left(\frac{1}{2}\theta_1' U_1'^2 + \theta_1' W_2'\right)' + c_\theta D_0 \theta_1\right] \theta_1 dZ = 0. \tag{2.78}$$

Equation (2.78) contains resonant ($e^{\pm i\omega_n t_0}$) and non-resonant terms (e^0, $e^{\pm 2i\omega_n t_0}$, $e^{\pm 3i\omega_n t_0}$). Non resonant terms enable to solve third order solution in frequency domain and associated mode shape, but it is out of our interests. We are focused only on the amplitude of the nth nonlinear resonance. The frequency of excitation Ω is decomposed on a sum of natural circular frequency ω_n and an

additive detuning parameter $\varepsilon^2\sigma$, thus we write:

$$\Omega T = \left(\omega_n + \varepsilon^2\sigma\right) T = \omega_n T + \varepsilon^2\sigma T = \omega_n t_0 + \sigma t_2. \tag{2.79}$$

By performing cumbersome computations on (2.78), decomposing and collecting with respect to frequencies and then extracting terms containing $e^{i\omega_n t_0}$ and $e^{-i\omega_n t_0}$ we obtain two ordinary differential equations. Their expressions are very long and can not be reported here, therefore we arrange them in general notation:

$$ic_1\frac{\partial A_{re}}{\partial t_2} + ic_2 A_{re} + 4c_3 A_{re}^2 A_{im} + \frac{1}{2}p_v e^{i\sigma t_2}\sin\left(\frac{n\pi}{c_z}\right) = 0, \tag{2.80}$$

$$-ic_1\frac{\partial A_{im}}{\partial t_2} - ic_2 A_{im} + 4c_3 A_{im}^2 A_{re} + \frac{1}{2}p_v e^{-i\sigma t_2}\sin\left(\frac{n\pi}{c_z}\right) = 0, \tag{2.81}$$

where

$$\begin{aligned} c_1 &= \rho\omega_n\frac{J\left(Gn^2\pi^2 - L^2\rho\omega_n^2\right)^2 + AL}{G^2 L n^2\pi^2}, \\ c_2 &= \omega_n\left[c_\theta\frac{\left(Gn^2\pi^2 - L^2\rho\omega_n^2\right)^2}{2G^2 L n^2\pi^2} + c_U\frac{L}{2}\right]. \end{aligned} \tag{2.82}$$

After substitution any beam properties, functions c_1 and c_2 have real positive values. The c_1 involves inertia, while c_2 contains damping coefficients. The key factor is c_3, which depends on system properties (A, E, G, J, k_s, L, ρ) and on the order n of the considered resonance.

Analytical frequency response curves

For determining frequency response curves of equations (2.80)-(2.81) it is convenient to introduce the polar form of the complex amplitudes:

$$A_{re}(t_2) = \frac{1}{2}a(t_2)e^{i\beta(t_2)},\ A_{im}(t_2) = \frac{1}{2}a(t_2)e^{-i\beta(t_2)}. \tag{2.83}$$

Then we rewrite (2.80)-(2.81), separating real and imaginary the modulation equations are found:

$$\frac{\partial a}{\partial t_2} = -\frac{c_2}{c_1}a - \frac{p_v}{c_1}\sin\left(\frac{n\pi}{c_z}\right)\sin\left(\sigma t_2 - \beta\right), \tag{2.84}$$

$$a\frac{\partial\beta}{\partial t_2} = \frac{c_3}{c_1}a^3 + \frac{p_v}{c_1}\sin\left(\frac{n\pi}{c_z}\right)\cos\left(\sigma t_2 - \beta\right). \tag{2.85}$$

Introducing variable

$$\gamma(t_2) = \sigma t_2 - \beta(t_2) \quad \Rightarrow \quad \frac{\partial \gamma(t)}{\partial t_2} = \sigma - \frac{\partial \beta}{\partial t_2}, \tag{2.86}$$

the system (2.84)-(2.85) becomes

$$\frac{\partial a}{\partial t_2} = -\frac{c_2}{c_1} a - \frac{p_v}{c_1} \sin\left(\frac{n\pi}{c_z}\right) \sin(\gamma), \tag{2.87}$$

$$a \frac{\partial \gamma}{\partial t_2} = \sigma a + \frac{c_3}{c_1} a^3 + \frac{p_v}{c_1} \sin\left(\frac{n\pi}{c_z}\right) \cos(\gamma). \tag{2.88}$$

After sufficient long transient period, motion becomes steady state and amplitude and phase angle are constant, that leads to:

$$\frac{\partial \gamma(t)}{\partial t_2} = 0, \quad \frac{\partial a(t)}{\partial t_2} = 0 \tag{2.89}$$

Solving equation (2.87) with respect to $\sin(\gamma)$ and equation (2.88) with respect to $\cos(\gamma)$ we get:

$$\sin(\gamma) = -\frac{c_2 a}{p_v \sin\left(\frac{n\pi}{c_z}\right)}, \quad \cos(\gamma) = -\frac{a\left(c_3 a^2 - c_1 \sigma\right)}{p_v \sin\left(\frac{n\pi}{c_z}\right)}. \tag{2.90}$$

From the *Pythagorean trigonometric identity* [94], $\sin^2(\gamma) + \cos^2(\gamma) = 1$ we get the *frequency response equation*:

$$p_v^2 \sin^2\left(\frac{n\pi}{c_z}\right) = c_2^2 a^2 + a^2 \left(c_3 a^2 - c_1 \sigma\right)^2. \tag{2.91}$$

Equation (2.91) can be transformed in the simpler form:

$$\sigma = \frac{c_3 a^2 \pm \sqrt{\frac{P_v^2}{a^2} \sin^2\left(\frac{n\pi}{c_z}\right) - c_2^2}}{c_1}. \tag{2.92}$$

Analyzing *free* nonlinear oscillations, excitation $p_v = 0$, and damping ($c_U = 0$ and terms $c_\theta = 0 \ \rightarrow \ c_2 = 0$) are assumed. This provides the *backbone equation*:

$$\sigma = \frac{c_3}{c_1} a^2 = c_b a^2, \tag{2.93}$$

Representation of function (2.93) on amplitude-frequency response plot is so called *backbone curve*. The backbone curve represents a nonlinear behaviour of the studied system and the *nonlinear correction coefficient* c_b is a fingerprint

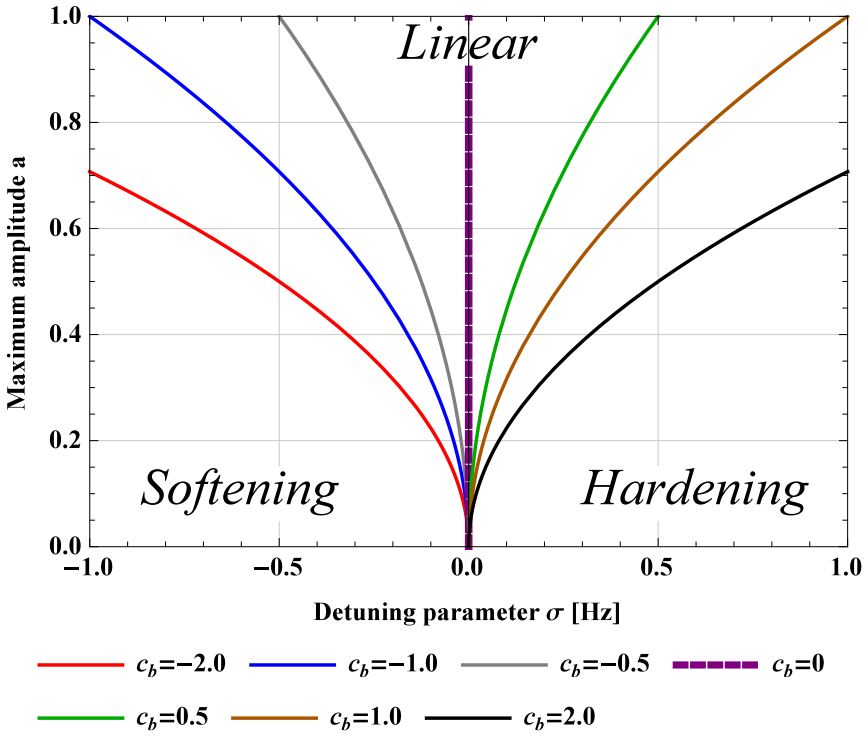

Figure 2.5: Examples of hardening, linear and softening backbone curves.

of the structure. Analyzed model with cubic nonlinearities has three various features [95]:

- $c_b > 0$: nonlinear natural frequency increases together with the amplitude of the oscillation a - hardening phenomenon;
- $c_b = 0$: natural frequency is independent of a- singular case when beam has linear nature (only up to third order of amplitude);
- $c_b < 0$: contrary to hardening, nonlinear natural frequency decreases with the increment a - softening behaviour.

The dichotomy between hardening vs softening is illustrated in Fig. 2.5. Examples of nonlinear correction coefficients (c_b), backbone curves and frequency response curves in dependence on spring stiffness k_s, which is the most important (for us) mechanical parameter, will be presented in Chapter 5.

2.2.2 Higher order resonances

Dynamics of the beam depends not only on physical properties of the structure, but also on frequency, and nature of excitation which may influence the behaviour of the system. Mostly, studies on nonlinear dynamics are limited to the lowest frequencies and their modal shapes, because they are the most prominent modes at which the object vibrates, and all the higher frequency modes have relatively smaller amplitudes of deformation. In our opinion they are important as well, and it is worth to analyze and better understand them.

Related to nth natural frequencies linear mode shapes of the beam are arranged in nth half-waves [96]. Symmetric modes ($n = 2 + 2k$) have a node in the midpoint of the beam. Therefore, in the analytical model they have to be triggered asymmetrically and it also eliminates cases of excitation only in the modal node. For example, the fourth mode ($n = 4$) can not be triggered at $c_x = 3/4$, $c_x = 2$ or $c_x = 4$ as well as the sixth ($n = 6$) mode will not disclose under conditions $c_x = 6/5$, $c_x = 3/2$, $c_x = 2$, $c_x = 3/2$ or $c_x = 6$ and so on. These assumptions are important only for forced-damped vibration, free dynamics do not have above mentioned requirements. The analytical approach presented in Section 2.2.1 is valid also for higher order resonances and will not be repeated here, but a few different approaches will be presented on this topic.

In real structures the first mode has the highest amplitude and next are lower for the same energy of the external excitation in respective resonat frequencies [77,97]. For this reason, a lot of authors are focused only in vicinity to the first natural frequency. In [59], Lacarbonara and Camillacci presented higher order mode shapes and their responses for higher order resonances of the hinged-hinged beam with additional lumped mass along the span. Additional mass distribution helps to soften frequency response curves: the lumped mass to the midpoint (quarter) reduces hardening behaviour of odd modes (1st, 2nd, 3-rd and 5-th) modes. All investigated six modes have hardening nature.

Experimental and analytical studies on first three flexular modes of a clamped-clamped microbeam resonator by Jaber et al. also demonstrate always hardening nature [98]. The authors excited each mode shape of the microbeam through different electrode configurations along the beam: full length (first mode), half of the length (second mode) and two third (1/3+1/3) on the sides. Amplitude-frequency plots show that full and two third electrodes are not able to excite (in the same phase) the second mode. On the contrary the half electrode is available to trig three modes.

Nonlinear resonance for higher order modes will be presented in Section 5.

Chapter 3

Finite element method

In mechanics of deformable bodies, the finite element method is a numerical technique wherein a continuous elastic structure is discretized by finite number of basic one-, two-dimensional or spatial elements. A one-dimensional element can be represented by a linear segment linking two nodes and their deformations are available along one axis (one direction), for example extension and compression of the beam. In planar variant, geometry can be discretized by beam elements, triangle or quadrangle defined on a plane by 2, 3 or 4 nodes, respectively. In planar problem all nodes have two (compatible in directions) degrees of freedom (DOF) and elements can be rotated. 3D shapes are commonly discretized by hexagonal/tetragonal volume elements, triangular/quadratic shell or beam elements in the space. Furthermore, we can manipulate the size of finite elements to better overlap (interpolate) geometry and design the shape of the structure in the rest configuration. In general, higher number of elements, as a consequence higher order degrees of freedom, provide a better approximation of the solution, althought it brings a higher computational cost. It leaves a great deal of freedom to discretize the system. All above mentioned elements can be interconnected at nodes and are able to interact between each other and represent an advanced structures with nonhomogeneous material properties [99, 100].

In this Chapter we will use the commercial software Abaqus_CAE® to build the finite element model. Next we will perform linear modal analysis and transient in time computations for large amplitudes on oscillations for nonlinear system. Outcomes of simulations will be compared with analytical results and thoroughly discussed in Chapter 5.

3.1 The design of numerical model

The system is constituted by 100 equal-length linear beam elements (101 nodes), with appropriate boundary conditions, placed in 3D space (X, Y, Z). Linear beam is discretized by 2-node elements of *B31* type. One end of the beam is located in the origin (0, 0, 0) and second point defines the length of the struc-

ture (0, 0, L). External forces/moments and deformations/rotations can be applied to each of nodes or pieces of elements. Therefore boundary conditions of simply supported beam (2.15)-(2.17) are satisfied by restraining deformations of nodes 1 ($Z = 0$) and 101 ($Z = L$), see Fig. 3.1. By blocking nodes displacement in the Y-direction and rotation around around the X and Z, we reduce the spatial arrangement to the plane (X,Z). The linear elastic element k_s is made in *Springs/Dashpots* module by linking beam's axially unrestrained tip and the origin of coordinate system. Spring force is linearly proportional to deformation and follow the axis of the undeformed beam.

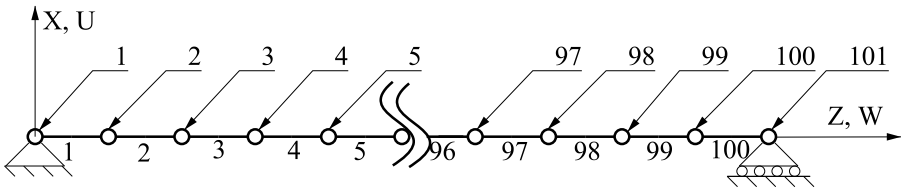

Figure 3.1: Finite element model of a hinged-simply supported beam. Numbered circles are nodes, and solid horizontal lines represent beam elements.

The finite element method is characterized by dimensional calculations. In our considerations we will focus on beams with two different geometrical relations:

- structure of square cross-section with a length over least radius of gyration (the thickness in a more susceptible direction) ratio equal to 10, let us call this case $\boldsymbol{T}$;
- a configuration $\boldsymbol{S}$ describes the object of high slenderness coefficient length to thickness almost 100.

Table 3.1: The steel beam $\boldsymbol{T}$ - parameters. The shear factor consistent with [20].

Beam length L[m]	Cross section A [mm^2]	Density ρ [kg/m^3]	Young modulus E [GPa]	Poisson's ratio ν [-]	Shear factor χ [-]	Spring stiffness k_s [N/m]
0.5	50×50	7850	210	0.3	0.85	$0 \leq ... \leq \infty$

Mechanical parameters of the beam $\boldsymbol{T}$ are listed in Table 3.1. These properties are used in theoretical considerations and can be freely changed. The

idealized theoretical model $\boldsymbol{T}$ does not take into account any additional translational/rotatory inertia subjected to the beam, although it will be done using the appropriate interaction function as in example $\boldsymbol{S}$. It will be used to adjust the numerical model to physical boundary conditions which coincide with the laboratory prototype. The properties of the $\boldsymbol{S}$ will be experimentally determined in Section 4.1.

3.2 Linear analysis

Natural frequencies of the finite element model of the simply supported beam with an axial spring are determined by linear *Lanczos* perturbation technique [101]. The Abaqus_CAE® solver generates linear responses within a few seconds, thus we analyze the first ten natural frequencies and associated mode shapes.

As it is possible to see in Fig. 3.3 and Fig. 3.2, the natural frequencies which correspond to mode shapes in axial direction increases for restrained end ($k_s = \infty$) with respect to free to move tip. The first longitudinal mode changes from third to fourth natural mode. The spring increases stiffness of the structure, while the mass matrix is constant. Consequently the mode shapes in axial direction differ. On the another hand flexural modes are not affected by the stiffness of the axial spring, and thus transerval natural frequencies and corresponding mode shapes do not change. For lateral oscillations the longitudinal deformations are much smaller and in linear regime are neglected.

To better understand this effect we vary boundary conditions in axial direction by changing the spring stiffness k_s and report natural frequencies in Tab. 3.2. In our study the key parameter is k_s and to analyze results we introduce dimensionless parameter κ related to the beam tensile stiffness:

$$\kappa = \frac{k_s L}{EA} \tag{3.1}$$

3.3 Nonlinear dynamics

3.3.1 Free dynamics

In this section the free nonlinear oscillations of the finite element model are studied for large amplitudes. The main aim is to perform simulations and then build the backbone curve. In the procedure we investigate unforced and slightly damped vibrations and then correlate the amplitude of displacement and the nonlinear vibration frequency.

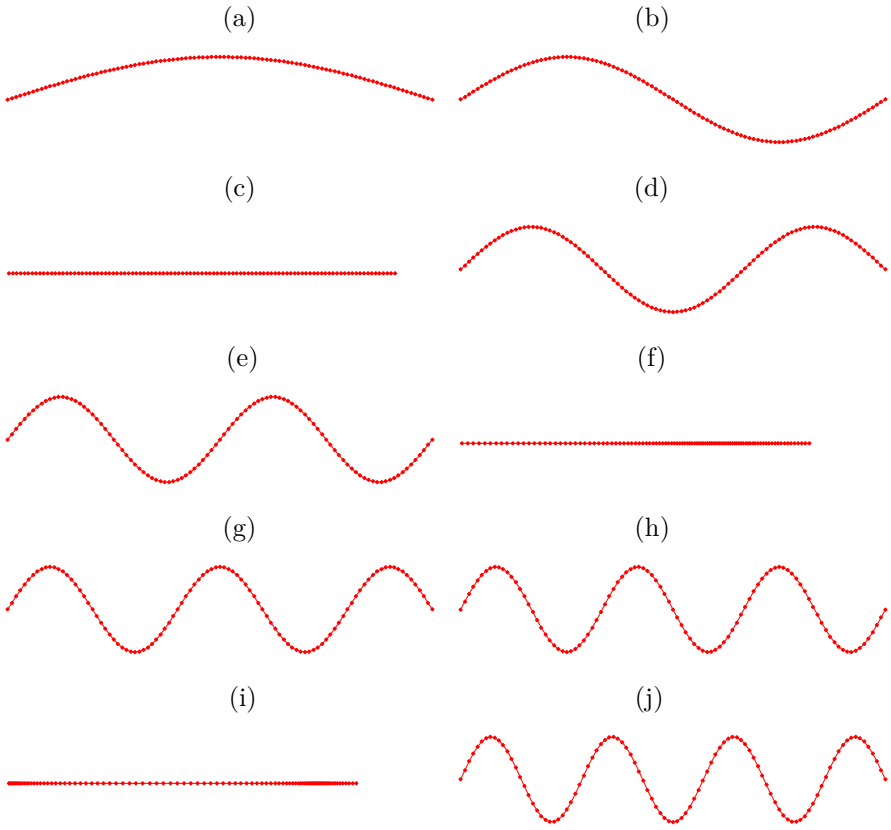

Figure 3.2: From the first (a) to tenth (j) mode shapes of the hinged simply-supported beam with no spring ($k_s = 0$). Longitudinal modes are 3rd, 6th and 9th. Dots represent deflected nodes and deformed lines are beam elements.

Numerical computations are based on beam model $\boldsymbol{T}$ and transient *explicit* simulations are made in three steps:

1. Defining midpoint displacement $U0 = 30mm$ and gradually deforming the structure in the first mode shape. The transverse shape of the beam is close to the first mode presented in Figures 3.3a and 3.2a. However the nonlinear normal mode is different that the linear one [55, 102–105]. The example of Figure 3.4 shows that large deformation in X-direction entails displacement of the nodes in Z direction in the case of hinged-simply supported beam.

2. Quenching of vibrations (closure of the transient). Here and in the previous point the damping coefficient is high.

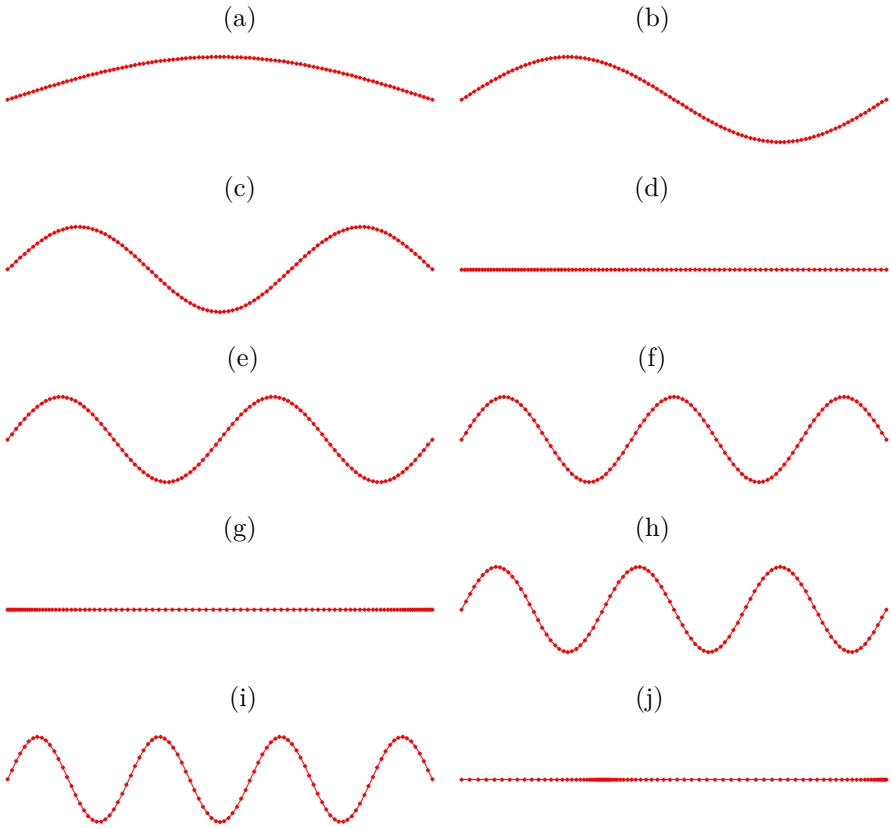

Figure 3.3: From the first (a) to tenth (j) mode shapes of the hinged hinged beam ($k_s = \infty$). Longitudinal modes are 4th, 7th and 10th. Dots represent deflected nodes and deformed lines are beam elements.

3. Change the linear bulk viscosity parameter to 0.06, relase the lock and recording the displacement U of node 50. The time history lasts 1 second. An example is shown in Fig. 3.5

The small damping introduced to the system has two advantages: stabilize numerical computations and slowly decrease amplitude of oscillations. Thanks to this, not one but many amplitudes can be analyzed in one simulation. Decreasing amplitude causes change in period of oscillations. Figure 3.6 displays examples of two zooms of time histories where amplitudes are about 2.3 mm and 0.7 mm.

The outcomes are subjected to amplitude frequency analysis as follow. Local maxima are picked from the time history and then a time distance between closest two peaks, one before T_{n-1} and one after T_{n-1}, is divided by two. This

Table 3.2: Natural frequencies of the beam-spring system ($\boldsymbol{T}$). Label b (**l**) represents bending (longitudinal) mode shape.

	Mode shape/natural frequency [Hz]					
Mode No.	$\kappa = 0$	$\kappa = 0.25$	$\kappa = 1$	$\kappa = 5$	$\kappa = 10$	$\kappa = \infty$
1	1st b 461.47	1st b 461.47	1st b 461.47	1st b 461.47	1st b 461.47	1st b 461.47
2	2nd b 1764.5	2nd b 1764.5	2nd b 1764.5	2nd b 1764.5	2nd b 1764.5	2nd b 1764.5
3	**1st l 2586.1**	**1st l 2824.3**	**1st l 3340**	3rd b 3720.4	3rd b 3720.4	3rd b 3720.4
4	3rd b 3720.4	3rd b 3720.4	3rd b 3720.4	**1st l 4368.8**	**1st l 4713**	**1st l 5172**
5	4th b 6129.3	4th b 6129.3	4th b 6129.3	4th b 6129.3	4th b 6129.3	4th b 6129.3
6	**2nd l 7757.6**	**2nd l 7843.9**	**2nd l 8088.2**	5th b 8833.4	5th b 8833.4	5th b 8833.4
7	5th b 8833.4	5th b 8833.4	5th b 8833.4	**2nd l 8979.1**	**2nd l 9483**	**2nd l 10343**
8	6th b 11723	6th b 11723	6th b 11723	6th b 11723	6th b 11723	6th b 11723
9	**3rd l 12927**	**3rd l 12979**	**3rd l 13132**	**3rd l 13812**	**3rd l 14333**	7th b 14726
10	7th b 14726	7th b 14726	7th b 14726	7th b 14726	7th b 14726	**3rd l 15511**

value corresponds to one period T_n associated to the U_{nmax}. This procedure requires very dense sampling of the output together with accurate saving precision. In performed computations the time step has been set to 0.000001 seconds

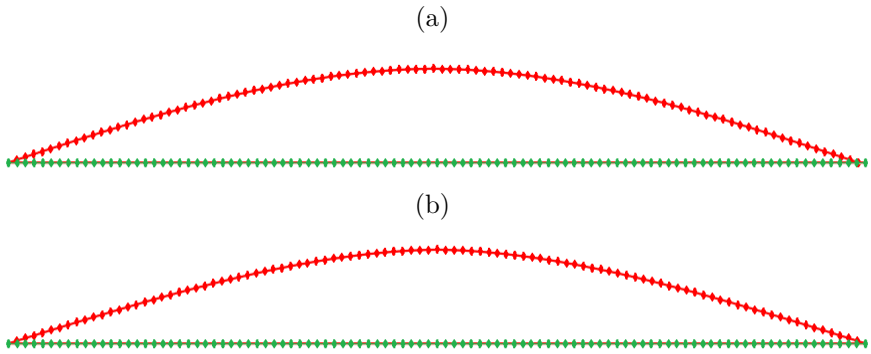

Figure 3.4: Hinged-simply supported (top) and hinged-hinged (bottom) beams $\boldsymbol{T}$. Undeformed (green) and deformed (red) finite elements. For $U0(Z = L/2) = 30$ mm the movable tip is translated about $W(Z = L) = -4.2286$ mm.

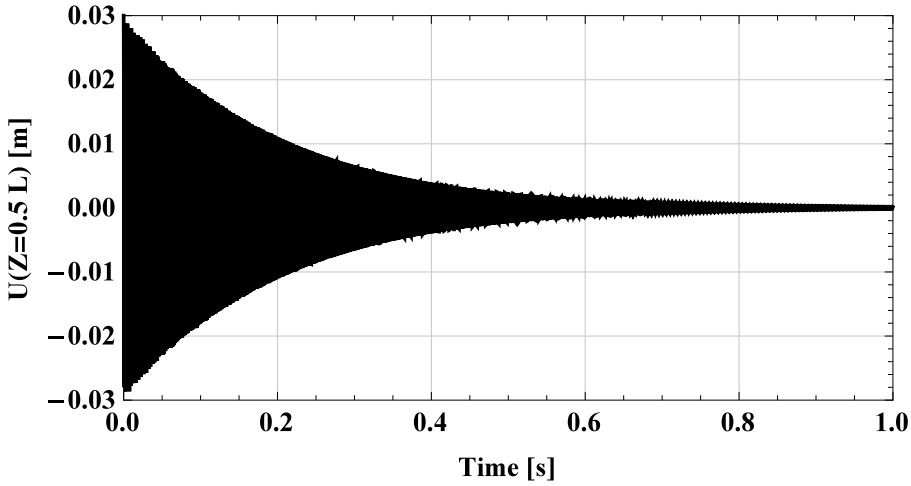

Figure 3.5: Free oscillations of the beam $\boldsymbol{T}$, $k_s = \infty$. The vibration amplitude decreases logarithmically with time.

and coordinates of each point are saved with 9 decimal digits. At the end set of amplitude peaks is transformed from time domain to frequency domain (one over period). This procedure is done automatically and the backbone curve $U_{nmax}(1/T_n)$ is built very fast. Of course we are aware that computed frequency is affected by several numerical approximations, the initially deformed beam does not reflect nonlinear modal shape and another unwanted higher order modes take part in computations. In spite of this, it will be shown in

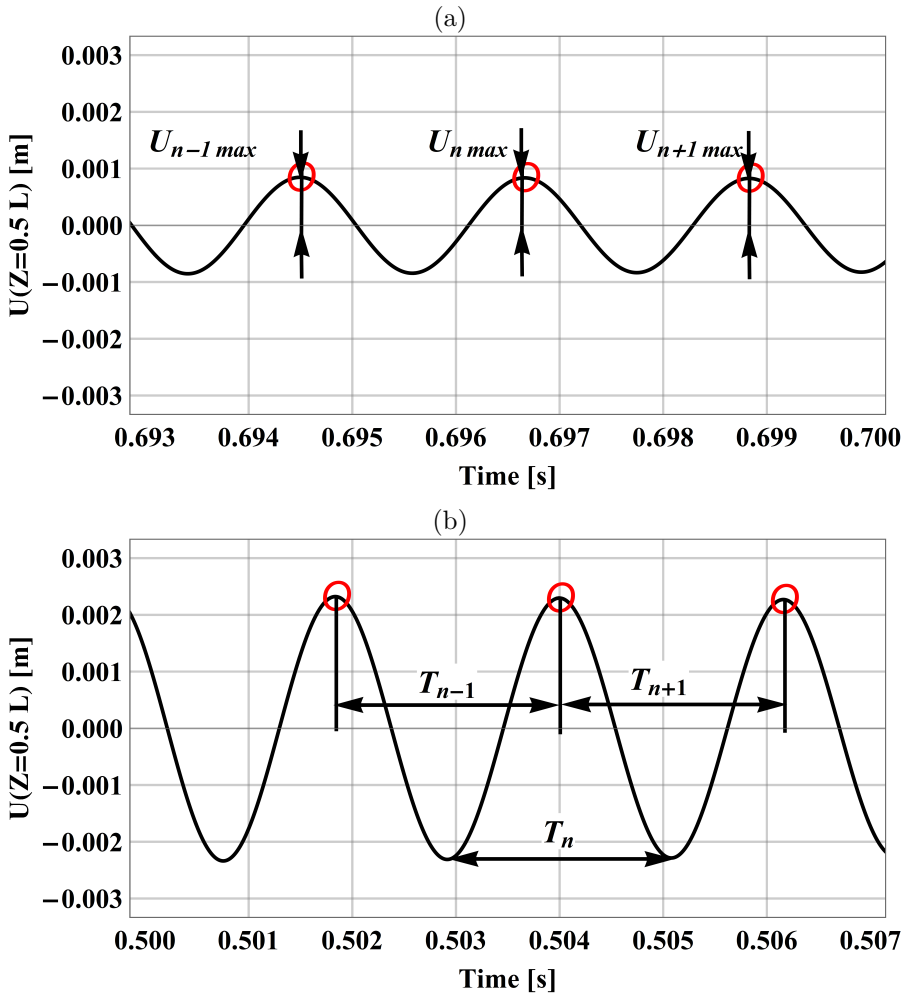

Figure 3.6: Two intervals of the time history of the beam $\boldsymbol{T}$, $k_s = \infty$, $U0(Z = L/2) = 30$ mm. Red circles correspond to consecutive amplitude peaks U_{max} (a) and time period T (b).

Section 5 that this procedure gives approximate results, but reliable in the sense of the hardening/softening dichotomy.

3.3.2 Forced vibrations - path-following method

Previous numerical computations present the linear and nonlinear free dynamics of the Timoshenko beam $\boldsymbol{T}$. In this section we are focused on constructing the full frequency response curve of the system for large amplitudes of forced-damped vibrations in the neighborhood of the primary resonance.

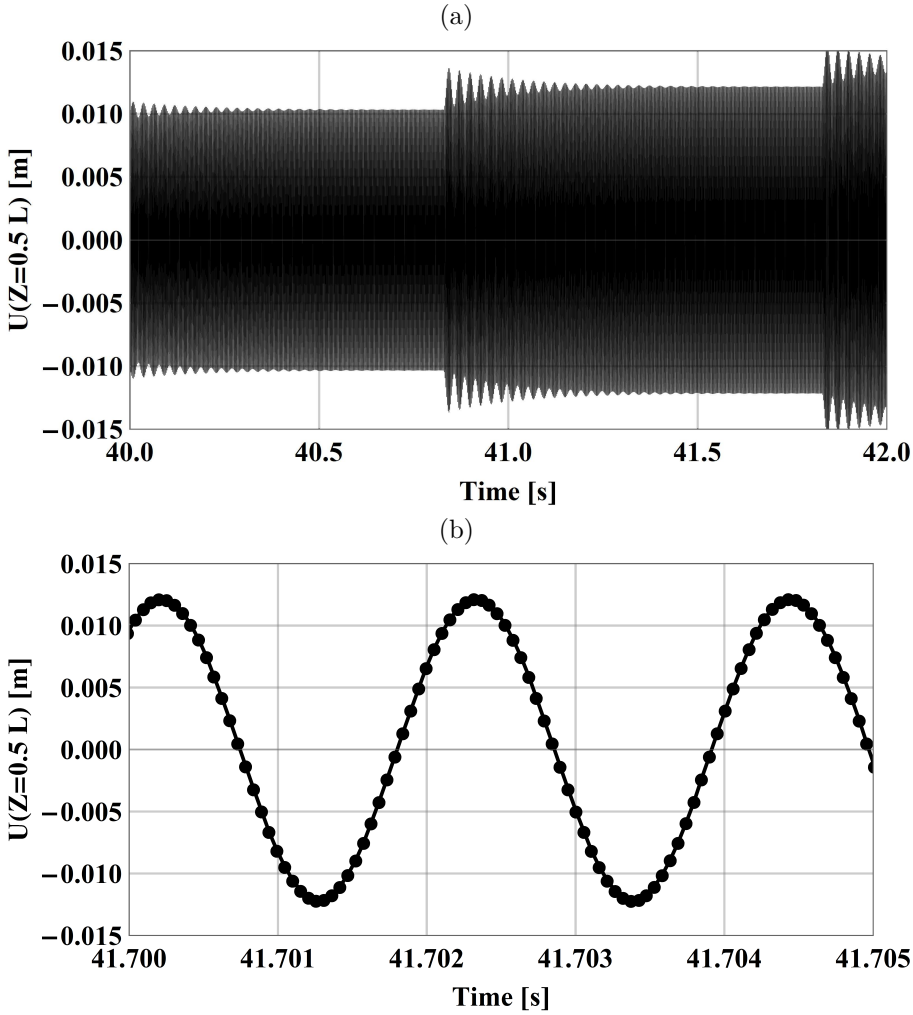

Figure 3.7: Results of simulation: gradually change frequency of excitation (a) and steady state motion (b). The hinged-hinged beam $\boldsymbol{T}$, $\kappa = \infty$, $P_v = 40799.2$ N.

In this section we assume as in Eq. (2.28) a concentrated force P_v imposed to the center point of the beam ($c_z = 2$) and oriented vertically. The amplitude of excitation P_v is assumed to represent 1 mm static deflection of the hinged simply-supported beam (0.2% of the beam's length and 2% of its thickness). Any different type of excitation can be applied in this general procedure, with full freedom of other frequency ranges - for instance higher order resonances or multifrequency excitation.

The simulation is composed of 163 computational steps (dynamic explicit),

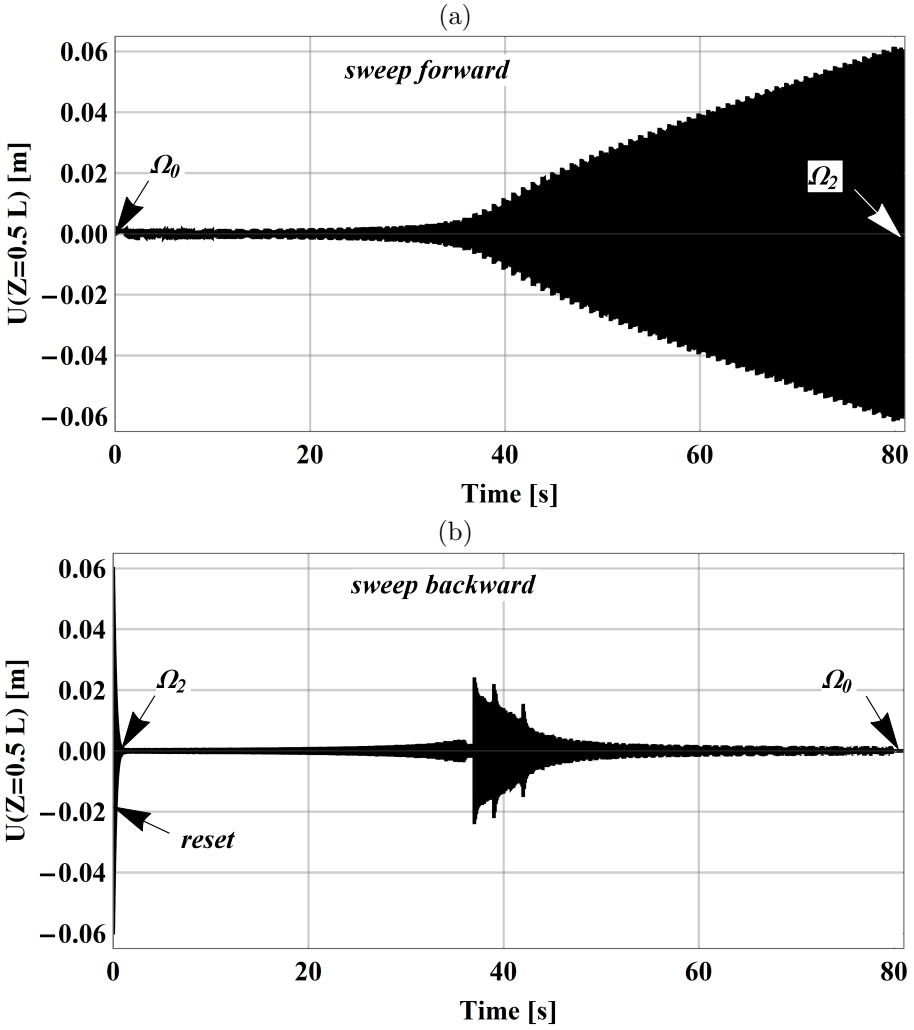

Figure 3.8: Forced-damped vibrations, global sweep forward Ω_+ (a) and backward Ω_- (b) of the hinged-hinged beam $\boldsymbol{T}$, $\kappa = \infty$, $Pv = 40799.2$ N, 0 Hz$< \Omega < 2 \times 461.47$ Hz.

each of them is assigned to nth frequency of excitation Ω_n. In the first computational step the structure is loaded by static force ($\Omega = 0$) and lasts 1 second, then in second computational step the frequency is tuned to $\Omega_{0.025} = 0.025 \times 461.47$ Hz, where 461.47 Hz is the first natural frequency, see Tab. 3.2. At the same time, the final deformation for previous computational step is used as the initial shape of current computational step. The structure is excited by a sufficient number of (full) periods, during which the transient state turns into steady state with constant amplitude (an example is reported in

Fig. 3.7a). The procedure is gradually repeated for higher frequencies $\Omega_{0.05}$, $\Omega_{0.075}$ ... Ω_1, $\Omega_{1.025}$ up to the highest frequency $\Omega_2 = 2 \times 461.47$ Hz. Technically, fine sampling of the time history is not of great importance as in free oscillations: although we assumed $\Delta t = \frac{1}{40 \times \Omega_n}$ to record a smooth shape of harmonic motion in axial and transversal directions (Fig. 3.7b). The gradual change of frequencies is called the *sweep forward* from minimum to maximum frequency (double natural frequency of the first bending mode) and we name it Ω_+ (with positive sign). The sweep forward takes 80 computational steps, next we introduce a *reset step* to Ω_0 and then repeat whole procedure by sweeping frequencies backward Ω_- as in Fig. 3.8. The reset step is important to detect the smallest amplitude path and a possible solution hysteresis. During Ω_+ we are able to cross the resonant frequency Ω_1 and then track high amplitudes. Using a little frequency change is essential in this approach, as by varying Ω the structure is slightly unsettled from the stable path but this disturbance is enough small not to loose basin of attraction and to approach another steady state solution [106]. In fact, in case of significant change of excitation frequency, mismatched initial conditions can cause jump to different branch or undergo any other system attractor. In scenario of sweeping backward the jump between lower and upper branches appears in 34th second of computational time, which correspond to $\Omega_{1.15}$. Further Ω_- decrement results in tracking the already known solution from sweep forward. It may happen that more than two solution paths exist, for example detached loop and; the best method to check this is the shooting method presented in next section.

In post processing the time history is divided into segments. Frequencies $\Omega_{n\pm}$ are individually inspected for amplitude of a steady state solution. If this condition was not reached, the calculation time has been properly extended. For some parameters, internal resonances occur in the system and the time history is composed of two harmonics. In this case, the peaks of the greatest amplitude of the stabilized segment are read and sorted.

The hardening vs softening dichotomy can be detected by the present approach, and the final outcome is the full frequency response curve. Results of numerical computations will be presented in Chapter 5. The subsequent analysis will be expanded by different cases of excitation. The presented approach of path-following method, numerical simulation made by explicit finite element method is very general and does not change for different more advanced structures.

3.3.3 Forced vibrations - shooting method

The last version of numerical method for plotting the frequency response curve is the shooting method. It acts as a combination of already presented free

oscillations and path-following methods. In the first step the beam is quasi-statically deformed by a midpoint amplitude displacement $U0_m$ which determines the initial shape of the structure. The index m denotes amplitude $U0$ in millimeters. Next a harmonic excitation (Ω_n) is applied to the structure. The properly adjusted integration time leads to a stable solution of amplitude $Umax_{m,n}(U0_m, \Omega_n)$. Figure 3.9 shows an exemplary number of simulations, necessary to cover the test range with a pattern for min< m <max and min< n <max. Several simulations can be carried out in parallel.

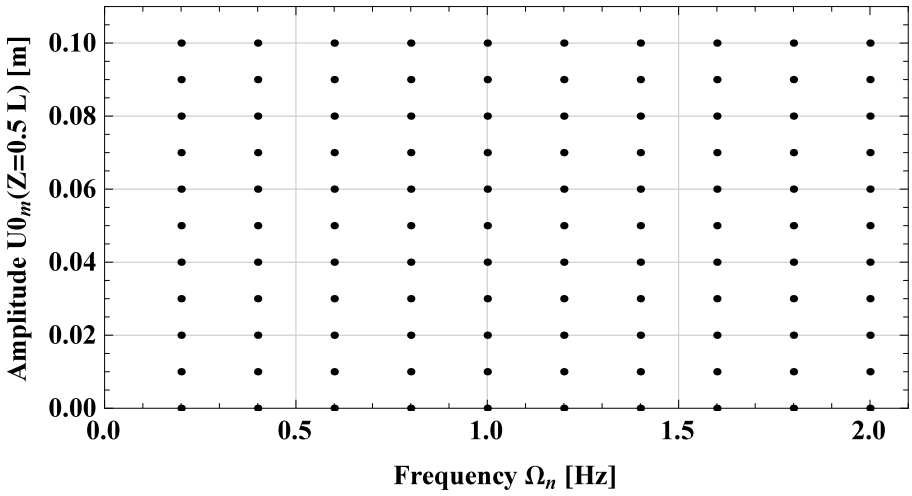

Figure 3.9: Sample distribution of initial points for shooting method: $10 \times 10 = 100$ simulations.

The set of performed simulations are reordered by the excitation frequency and corresponding vibration amplitude. Integration process for one of chosen frequencies (i.e. $\Omega_{1.425}$) can finish with different solution amplitudes; notwithstanding, in most cases regroup into one or more branches as you can see in Fig. 3.10. Two stable solutions were detected, the first value is $Umax_{60,1.425} = Umax_{30,1.425} = Umax_{20,1.425} = Umax_{10,1.425} = 0.9$ mm, while the second amplitude $Umax_{50,1.425} = Umax_{40,1.425} = 39$ mm and no other branches were found, although there is no certainty that they are not there.

It may happen that experimental or analytical predictions are known and then the range can be specified by eliminating unnecessary starting points. It is worth to remark that different methods can have discrepancies outputs and they should be considered only as a hint. This strategy of drawing a full frequency response curve is much more time consuming than the path-following method. All simulations starts from the quasi-static computational step and in order

to receive several solutions the initial amplitudes $U0$ have to be well chosen, in vicinity to solution paths. Reduction in the differences between the initial shapes of the beam generates more computations, but nonetheless in some cases the specific Ω_n can be thoroughly tested without sweeping forward neither backward. On the other hand, the final deformation of the beam together with established Ω_n can be successfully used as a starting point to follow a detached branch by semi-continuation method.

3.4 Compatibility of numerical methods

In this chapter, we first presented numerical model of a hinged simply supported beam with an axial spring on its tip. To perform computations we chose the set $\boldsymbol{T}$ for Timoshenko beam properties, and then the linear modal analysis has been performed for various spring stiffnesses k_s. Subsequent Sections show three numerical approaches dedicated to study large amplitude vibrations aimed at:

- a change of oscillation period in free dynamics as a result of decreasing amplitude, which allows to draw a backbone curve;
- the path-following method, which sweep frequencies of excitation in order to reconstruct a frequency response curve;
- manipulating initial conditions of forced damped beam, that allows to pump a portion of strain energy to the system and for selected parameters check the response of the structure

Presented methods are realized explicitly in the time domain and can be implemented to study the nonlinear dynamics of any mechanical system. The linear modal analysis displays natural frequencies and associated linear modal shapes, it always starts dynamic analysis and determines the target range of the studied problem. Next, using an approximated nonlinear modal shape, free nonlinear vibrations are performed to build the backbone curve, which present the hardening vs softening behaviour. The frequency response curve supplements the backbone curve for forced-damped oscillations. It can be done by at least two procedures, path-following or shooting methods. It is possible to use more sophisticated combination of these two methods. For example, initially draw all achievable curves by sweeping frequency of excitation and then scan area by guessing initial modal shapes for a given frequency. It gives a robustness of investigated solutions measure and can detect isolated curves, unexplored by path-following method and map them by reusing a local semi-continuation method. Exchange information between presented methods can allow to build the frequency response curves and collect associated nonlinear

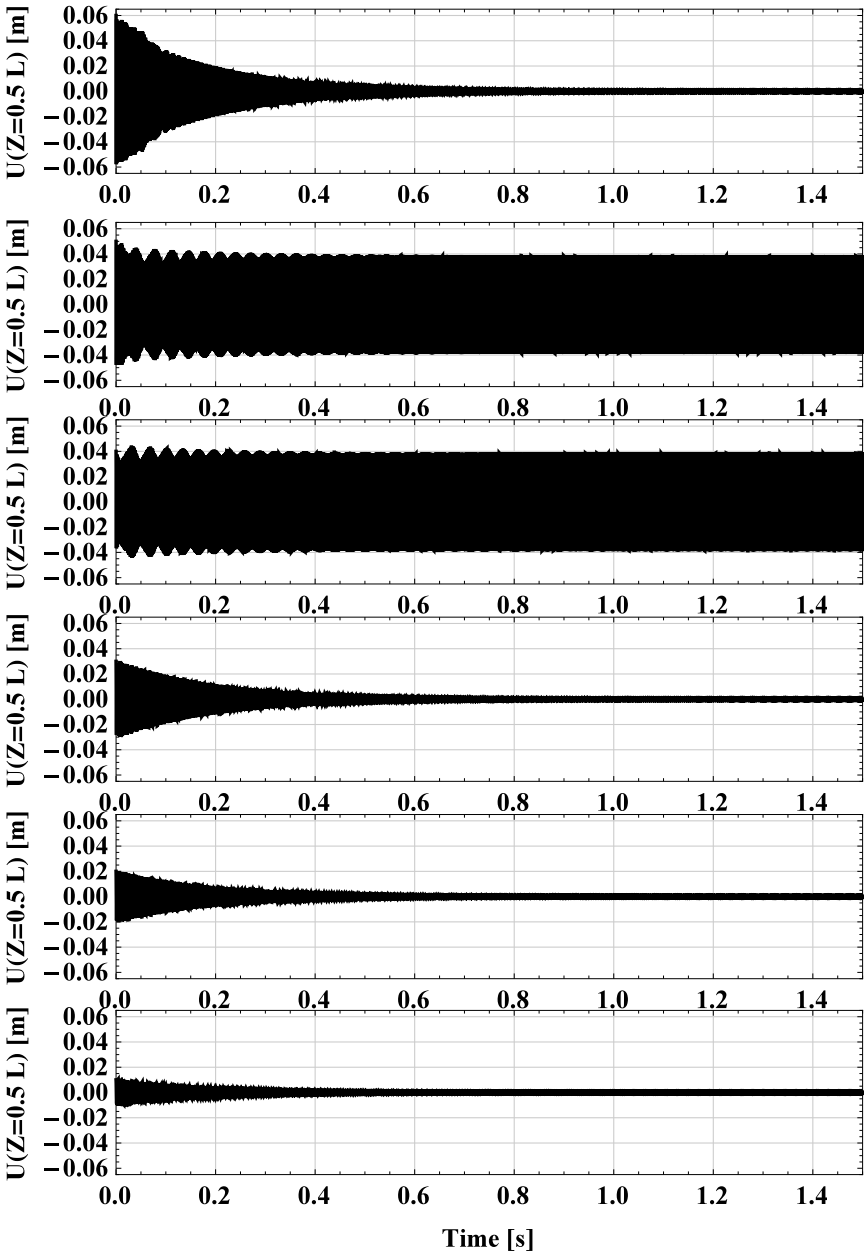

Figure 3.10: Time histories of numerical integration starting from top to bottom $U0_{60,1.425}$, $U0_{50,1.425}$, $U0_{40,1.425}$, $U0_{30,1.425}$, $U0_{20,1.425}$, $U0_{10,1.425}$, $U0_{0,1.425}$. The hinged-simply supported beam $\kappa = 4$, $P_v = 40799.2$ N.

modal shapes, stress pattern and so on, but the explicit simulations are time consuming [107].

A thorough analysis will be carried out by comparing these methods first with analytical results of a beam $\boldsymbol{T}$ and next with the laboratory dynamical tests described in next Chapter 4.

Chapter 4

Experimental test

A critical moment of any computation is to confront results obtained with different methods, e.g. numerical vs analytical methods, and understand reasons of differences. This knowledge often helps to improve a model and achieve very advanced solutions, tuned to each other. However, what happens if the idealized assumptions has no reflection in practice? How the system behaves in non-nominal conditions with some imperfections? Where and why the biggest difference occurs? For all of those questions there is one response [108]:

Experiment is the sole source of truth.
It alone can teach us something new;
it alone can give us certainty.

It motivates authors to manufacture and then investigate a prototype in laboratory. Requirements for the beam are to satisfy hinged-simply supported boundary conditions, give the possibility to change the boundary conditions in axial direction and enable to excite a large vibration amplitude in resonant frequencies. For this purpose, the kinematic excitation on slip table is provided and damping in the joints of the system are properly minimized. Additionally, a hinge and an axial sliding support requires high stiffness in restrained directions. The limitations of the measuring instruments and shaker maximum power specifications have to be taken into account, too.

The prototype presented in Fig. 4.1 meets all the above-mentioned requirements. The physical model is screwed to the slip table [109]. Three massive steel bodies hold the bearing hinge and the sliding support. The hinge is located on the left hand side and the translatable movable shaft holds the beam on the right. The sliding support is made of steel screws $M14$, supporting parts have been covered with Teflon. The two triples are able to move along them and hold the shaft, their interacting surfaces were also covered with thin reducing friction sleeves. Various sets of four elastic elements can be mounted, or with no spring leave the system simply supported. A preload in push springs makes equivalent stiffness k_s symmetrical in compression and tensile [110], during oscillations to avoid impacts between holding mechanism and the undeformed

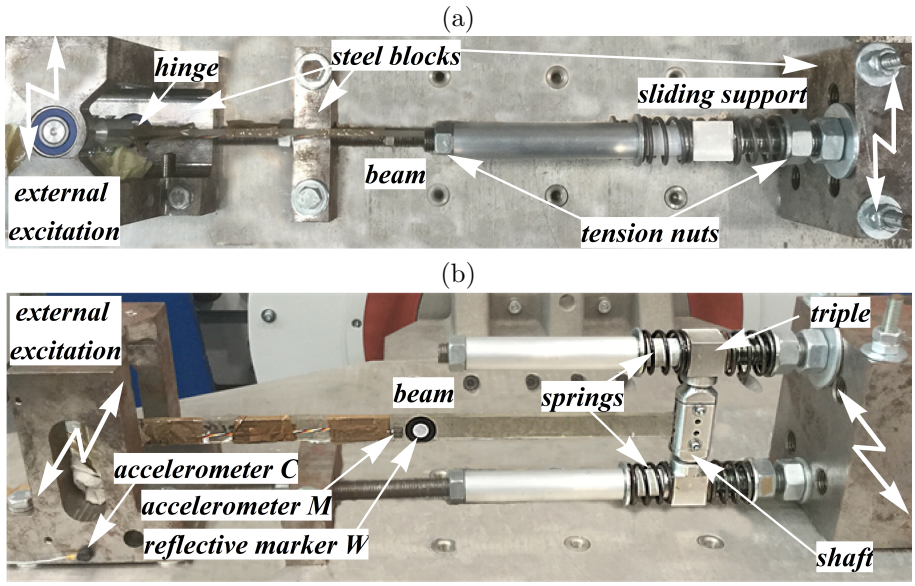

Figure 4.1: The laboratory setup mounted on the slip table top (a) and front (b) views. The direction of kinematic excitation is marked by white lighting arrows shape.

springs. Perpendicular positioning shaft to triple is very important, the delicate slant causes not surface but edge interaction and undesirably increases resistance to movement in the layout.

The presented system is designed to best reflect the hinged-simply supported beam with an elastic longitudinal element. The aim of experimental tests is to examinate parameter κ. There are three ways to control beam tensile stiffness to axial spring stiffness ratio:

1. to use one beam and change the set of springs;

2. to set constant spring and vary length/cross-section of the beam;

3. to fix longitudinal support and then swap beams with identical dimensions and different material properties.

Option 1. was chosen since this approach allows easy study with comparable vibration amplitude. The disadvantage is the system modification that involves disassembling, replacing or removing springs and re-assembly. In this process differences always arise.

4.1 Setup identification

In the setup the parameter L is not a total length of the beam but a distance between hinge and shaft rotation axes. The constant along the beam cross-section A is $b \times h$, where h describes thickens and b is width. Material of the specimen is Plexiglass, with relatively low density to Young's modulus ratio [111]. High bending susceptibility together with substantial inertia helps to achieve high amplitudes in kinematic excitation. Table 4.1 presents geometrical dimensions and material properties of the beam.

Table 4.1: The Plexiglas beam $\boldsymbol{S}$ - parameters.

Beam length L[m]	Beam height h [mm]	Beam width b [mm]	Beam density ρ [kg/m^3]	Young modulus E [GPa]	Poisson's ratio ν [-]
0.45	4.75	20	1245.05	3.3	0.35

Figure 4.2: Springs from the least to the most stiff (from left to right): 67 × 28.5×1.8 mm, 100×32.5×2.5 mm, 60×35×3 mm, 43.5×33.5×3 mm, 61 × 33.5 × 3.5 mm.

Density of the beam was calculated by dividing mass over volume. Young modulus has been tested on strength machine Shimadzu AGS-X 5kN [112] (Fig. 4.3a) and for Poisson's ratio we refer to [111]. The elastic constraints

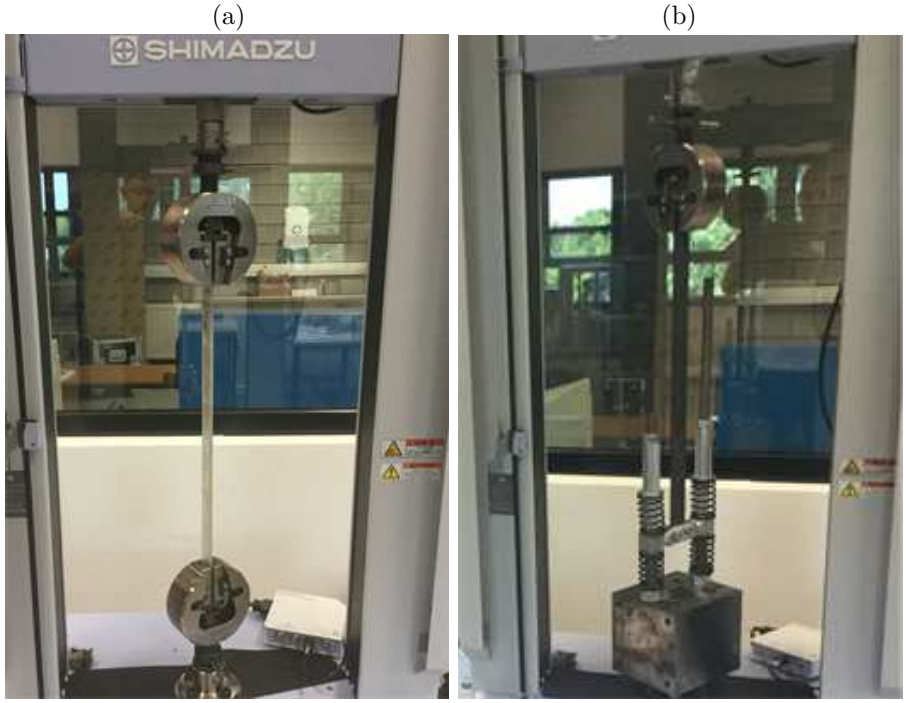

Figure 4.3: Arrangements of tensile/compression test of the beam (a) and the system of four linear springs on sliding support (b).

are made of four equal springs (Fig. 4.2), and have been examined individually in the vertical position, see Fig. 4.3b. The steel block, together with movable parts were mounted on the strength machine. The sample was replaced by a rigid steel bar. Tests were performed in extension and compression. Fig. 4.4 shows deformation-force characteristics of four spring set, and they have linear effective stiffness nature.

In order to minimize inertia effect of the handle, moving elements (triples, shaft and hinge) are made of aluminum. A higher mass of the structure (with constant stiffness) lowers the natural frequency [113] and should be taken into account. Mass M_t includes axially movable components subjected to the beams end ($Z = L$). The tip mass is 0.155 kg and consists of two triples, shaft and slide sleeves. The hinge and shaft have mass moment of inertia (calculated from geometry) $I_0 = 1.0928 \times 10^5$ kg m^2 and $I_L = 7.556 \times 10^6$ kg m^2, respectively.

The slip table has ability to control the displacement of the table top in one direction. Its excitation is described by the amplitude ξ and frequency of excitation Ω. A frequency can be set constant or variable in time. It allows to test the structure by kinematic excitation in X-direction in a neighborhood of

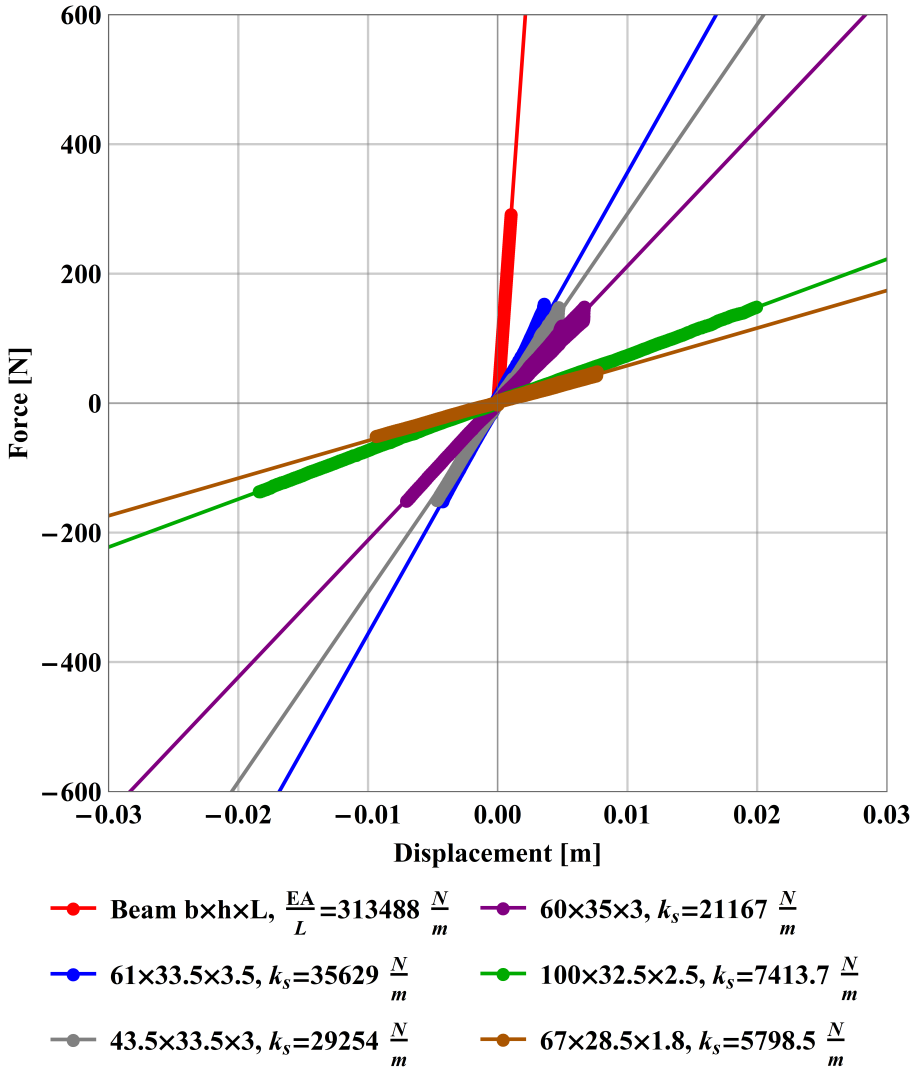

Figure 4.4: Compression-extension curves of four springs system and specimen tensile test. Thick (thin) lines are experimental (linear approximation) values.

the resonance.

The last part of the identification tests is to estimate the damping coefficient value and natural frequency. For first purpose the method of logarithmic decrement is used [114]. It is one of the most basic methods in which a structure is initially distorted in the shape of first bending mode and then the deformation is released together with recording amplitudes for free oscillations. The mea-

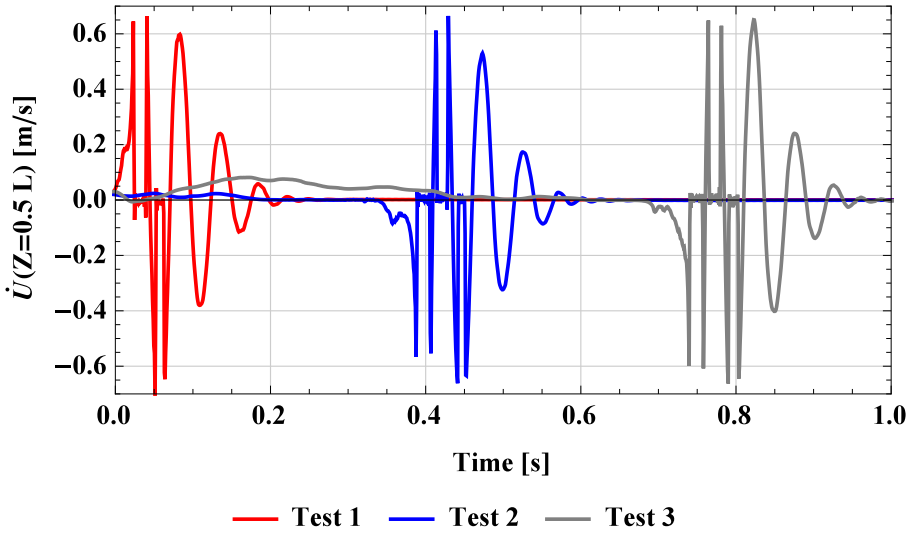

Figure 4.5: Experimental free oscillations of the beam $\boldsymbol{S}$, $k_s = 29254$ N/m. Record of the the entire measurement including deflection, lock release, out of scale measurement and amplitude decrement.

surement is performed with use non contact scanning laser Doppler vibrometer Polytec PSV-500 [115, 116]. Scanning head is set in front of the beam (Perpendicular to the XZ plane) and a laser beam is focused on the marker W (Fig. 4.1b). Oscillations velocity of the structure is recorded. Based on time history, two successive amplitudes (peaks) of oscillations are chosen to calculate damping coefficient in the form:

$$\zeta \approx \frac{1}{\sqrt{1 + \left(\frac{2\pi}{ln \frac{U_{nmax}}{U_{n+1\ max}}} \right)^2}} \tag{4.1}$$

Figure 4.5 shows three attempts of the test for the beam with $k_s = 29254$ N/m. The record of laser signal starts from manual deflecting process, then a beam is released. At the beginning large amplitudes of oscillation causes that laser goes beyond the marker **W** and loses reflection. As soon as velocity of beams midpoint decreases below 0.6 m/s, signal is smoothly recorded with frequency 1250 samples per second. Using first four peak amplitudes, the damping coefficient were calculated and outcomes are presented in Table 4.2. For all three cases the damping coefficient increases together with amplitude. Damping in the system is influenced by many factors like air resistance, damping inside the

Table 4.2: Experimental values of damping; beam $\boldsymbol{S}$, $k_s = 29254$ N/m. Parameter n describes the positive amplitude of full measured half-wave.

	Damping coefficient ζ [-]		
$U_{n\ max}$	Test 1	Test 2	Test 3
$n = 1$	0.1648	0.1665	0.1566
$n = 2$	0.1955	0.1679	0.2422
$n = 3$	0.2607	0.2155	0.2481

beam material (structural damping) or interactions between joints and support. All these issues are reduced to only one (general) value and it is highly likely that it depends on the amplitude and is not fixed [83,85,117]. Nevertheless, the tests were carried out in a static position of the table top. During kinematic excitation the beam is subjected to greater aerodynamic forces, consequently the parameter ζ can be changed. In forthcoming tests the damping factor will be adjusted individually to each of the frequency response curve of the system.

Finally, for small velocity amplitudes FFT analysis is performed, which is aimed to determine the natural frequency of free vibrations, see Fig. 4.6. The most interesting first natural frequency is ambiguous and occurs in 18 and/or 20 Hz. Results may differ for manual initial deflection, despite the best efforts in manufacturing connections, there are micro gaps in the supported part of the holder. Micro impacts introduce noise into the system. The kinematic excitation smooths this effect in nonlinear frequency response curves as shown in Section 5.3.

The parameters M_t, I_0 and I_L additionally modify boundary conditions, as can be seen on schematic representation of kinematically excited structure in Fig. 4.7. The values of these parameters, together with several types of spring and structural damping coefficients, are reported in the Table. 4.3. In the following the specimen is linked with spring stiffness parameter and will be featured in the form $\boldsymbol{S}_{\kappa\times 100}$, for example the experimental setup with an axial spring $k_s = 2167$ N/m will be denoted by $\boldsymbol{S}_3$.

4.2 Testing procedure

The slip table can be used in a wide frequency band and it enables to control vibration enviroment. The vibration exciter transforms the electrically generated and amplified signal into mechanical motion which is then transmited to

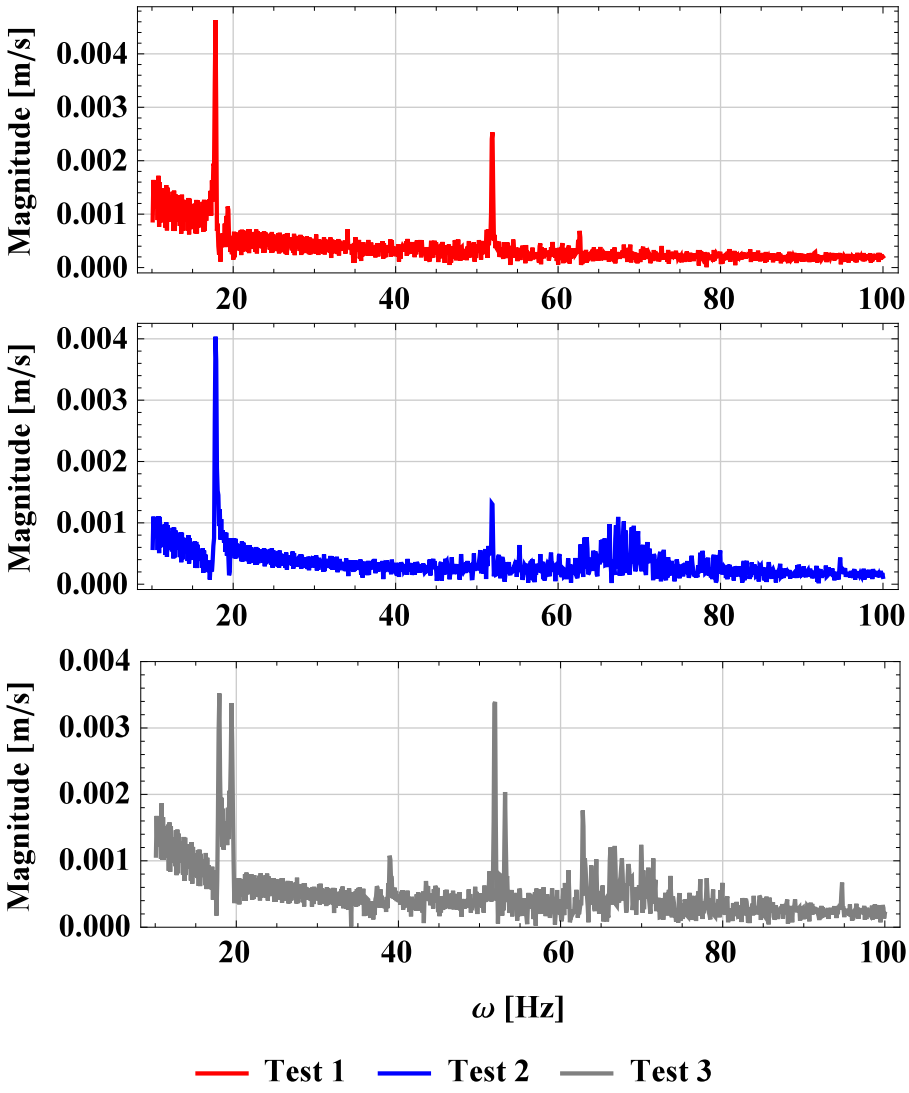

Figure 4.6: The fast Fourier transform of experimental time histories; beam $\boldsymbol{S}$, $k_s = 29254$ N/m.

the test sample by the shaker system [109]. The power generator has force limitation to 35000 N, the head is able to perform peak-peak displacement about 50.8 mm and frequency of excitation has to be greater than 10 Hz. The total moving mass is 234.95 kg and includes armature (31.5 kg), driver bar (8.45 kg), slip table (145 kg) and carried system (50 kg). It allows to run the slip table with maximal acceleration 147.15 m/s^2 (15 g). Considering that the natural fre-

Table 4.3: Parameters of the beam $\boldsymbol{S}$ and damping ratio of the structure.

M_t	I_0	I_L	k_s	κ	ζ
[kg]	[kg×m^2]	[kg×m^2]	[N/m]	[-]	[-]
0.155	1.0928×10^{-5}	7.556×10^{-6}	35629	0.05	0.1...0.3
			29254	0.042	
			21167	0.03	
			7413.7	0.01	
			5798.5	0.008	
			0 (no spring)	0	

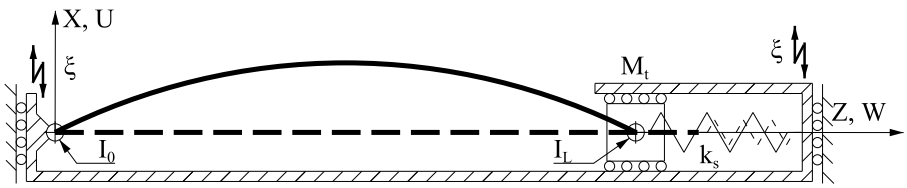

Figure 4.7: The kinematically excited hinged-simply supported beam with an axial spring, tip mas and moment of inertia.

quency of the beam is ≈ 20 Hz, we assume the frequency of excitation to range from 15 Hz to 30 Hz. It is associated to the maximum amplitude ± 4.14 mm, which is within the range allowed by the slip table. Performing long-time tests it is convenient to reduce critical amplitude up to 2.5 mm, which eliminates the risk of overloading and significantly reduces electricity consumption.

Two accelerometers are used for tests, first control gauge $\boldsymbol{C}$ is fixed on the hinges's holder and three-axial second sensor $\boldsymbol{M}$ is located in the middle of the beam, as shown in Figure 4.1_b. Controllers are linked with Personal Computer throught LMS, controlling and measuring systems. Figure 4.8 shows the scheme of the experimetal setup [118, 119].

Experiment started from tuning sensors, then frequency of excitation has been swept backward (Ω_-) from 30 Hz to 15 Hz and forward (Ω_+) from 15 Hz to 30 Hz. Each of sweeps began/ended by two seconds of start-up and shut-down, namely within this time the frequency of excitation is fixed and amplitude of excitation increases to given value or decreases to 0. Between Ω_- and Ω_+ excitation has been deactivated for 2 seconds. Total time of full course was 308 seconds and involved acceleration, deceleration processes together with

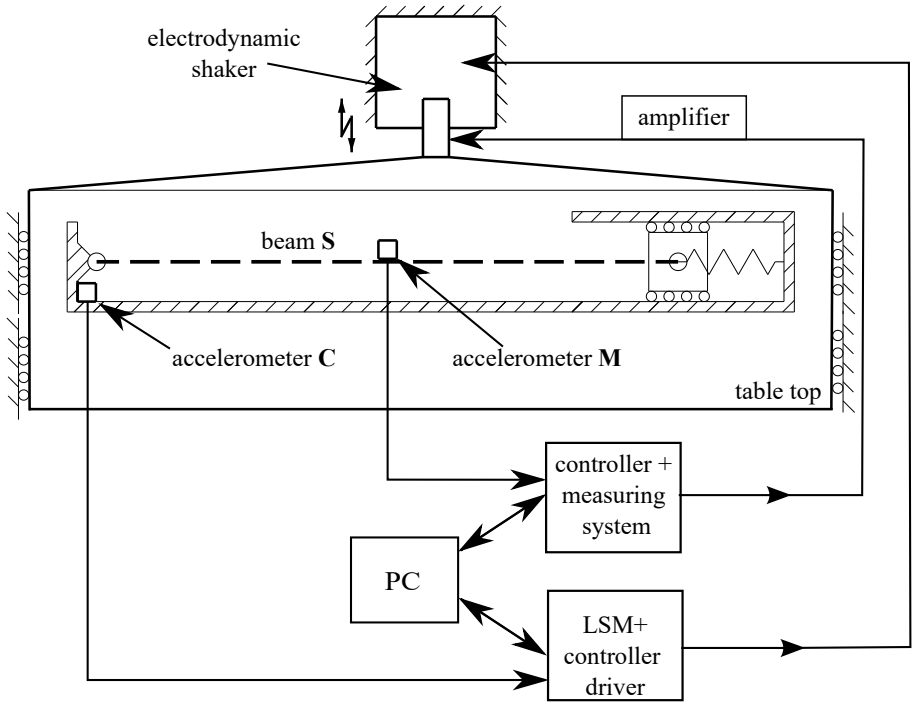

Figure 4.8: The control system scheme of the slip table - top view.

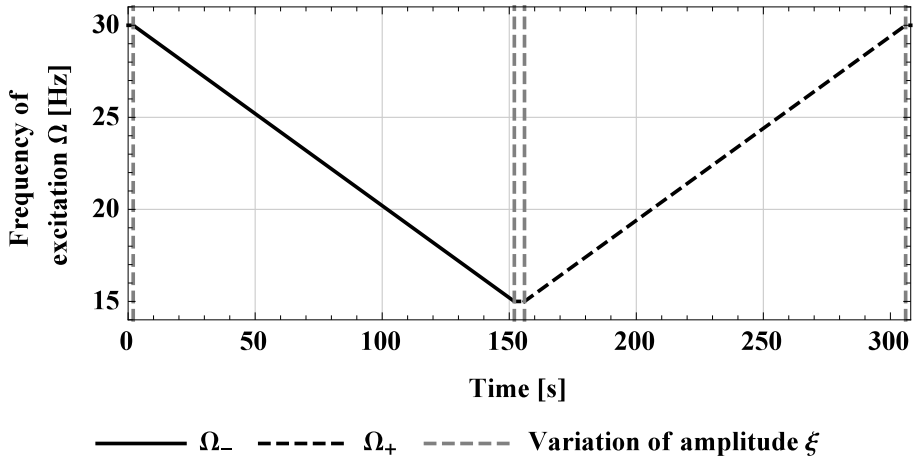

Figure 4.9: Frequency of excitation diagram for a full experimental cycle. Variation of amplitude states increment/decrement sections, during a sweep is constant.

two sweeps (forward and backward) and pause in the middle. In the input signal both parameters depend on time and the amplitude and the frequency of excitation. The input function is given by

$$g(t) = \xi(T)\cos\left(\Omega(T)T\right) \tag{4.2}$$

where ξ denotes the amplitude of excitation (displacement) and frequency of excitation $\Omega(T)$ is graphically presented in Fig. 4.9. One way sweep took 150 s. It means the speed of the sweep has been set 0.1 Hz/s. The experiment has been scheduled to examine full course (backward and forward) of each structure together with four amplitudes of excitation: 2.5 mm, 2 mm, 1.5 mm and 1 mm. In total it gives 48 (2×24) experimental frequency response curves.

The constant amplitude of excitation $\xi(\Omega)$ generates logarithmic acceleration gain together with increasing frequency of excitation. The acceleration profile $h(T)$ becomes:

$$h(t) = \frac{4\pi^2}{9.05778}\zeta(T)\Omega(T)^2\cos\left(\Omega(T)T\right), \tag{4.3}$$

and is represented in the standard form related to the gravity g_n. Multiplying the result by the constant 9.05778 the unit transforms into mm/s^2. The calculation is done automatically by the LMS software, see the profile editor in Fig. 4.10 and selected profiles of maximum amplitudes in 4.11a,b.

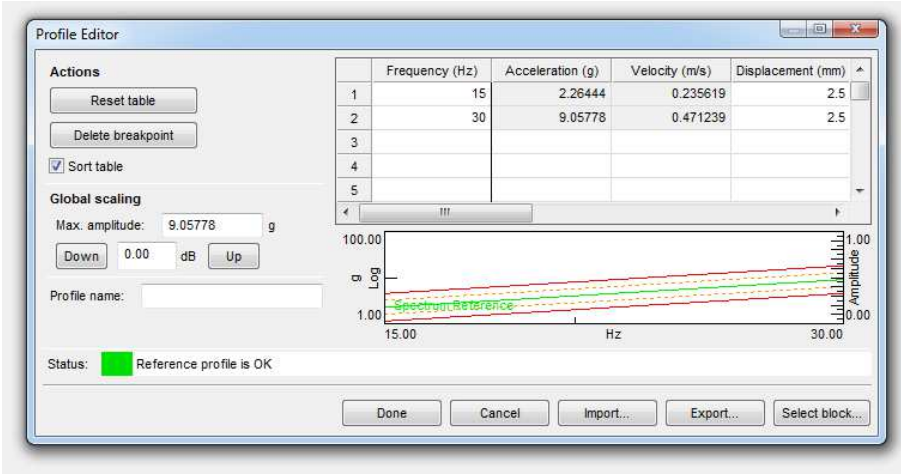

Figure 4.10: The profile editor in the LMS software.

An additional validation test on the control sensor with use the vibrometer Polytec PSV-500 was performed [115]. The constant velocity amplitude was tested for a few frequencies and simultaneously the motion was monitored by

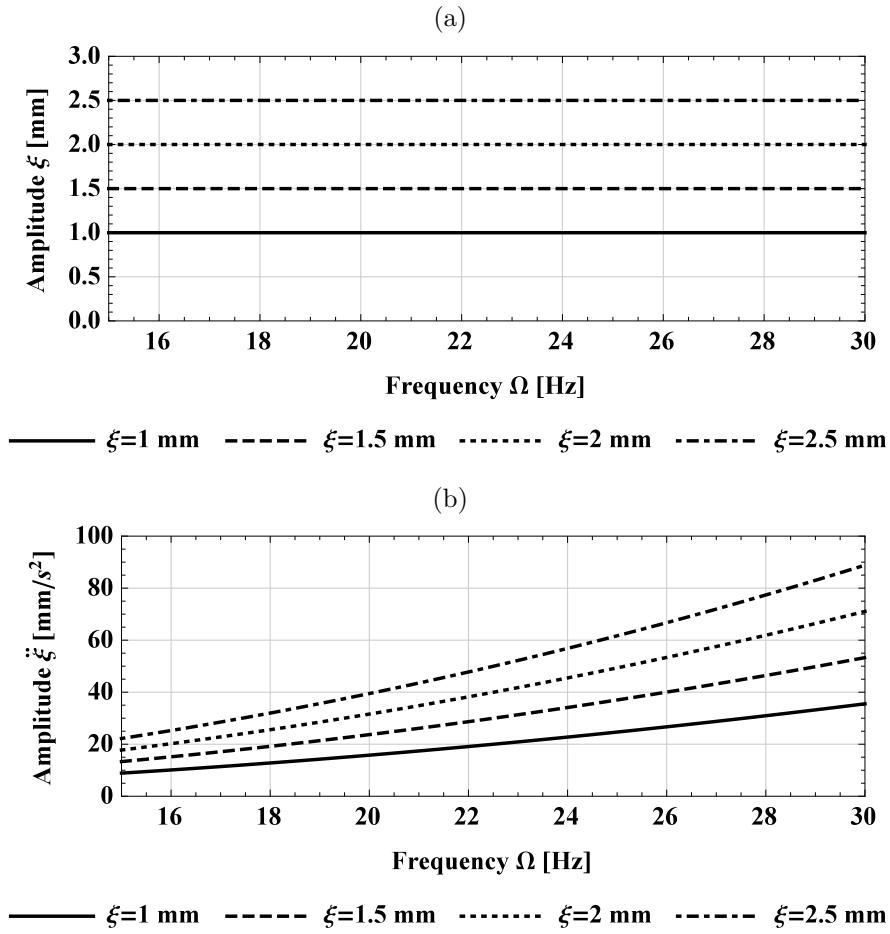

Figure 4.11: Maximum amplitudes of the selected excitation profiles: displacement (a) and acceleration (b).

a laser beam. The comparative study was successful for all tested frequencies.

4.3 Post processing

Outcomes of experimental test are absolute acceleration amplitudes of oscillations $\ddot{E}_a(\Omega)$ for accellerometer $\boldsymbol{M}$ and its phase angle $\varphi(\Omega)$ with respect to controller $\boldsymbol{C}$. The presumable time histories of acceleration are integrated to get the time histories of displacement. This procedure is done by optional function of the software. In the input displacement amplitude and frequency of excitation $\boldsymbol{C}$ are driven. Comparing results, it is convenient to convert the

absolute amplitude $E_a(\Omega)$ into relative amplitude $E_r(\Omega)$:

$$E_a(\Omega) = E_r(\Omega) + \zeta \cos\left(\varphi(\Omega)\right) \tag{4.4}$$

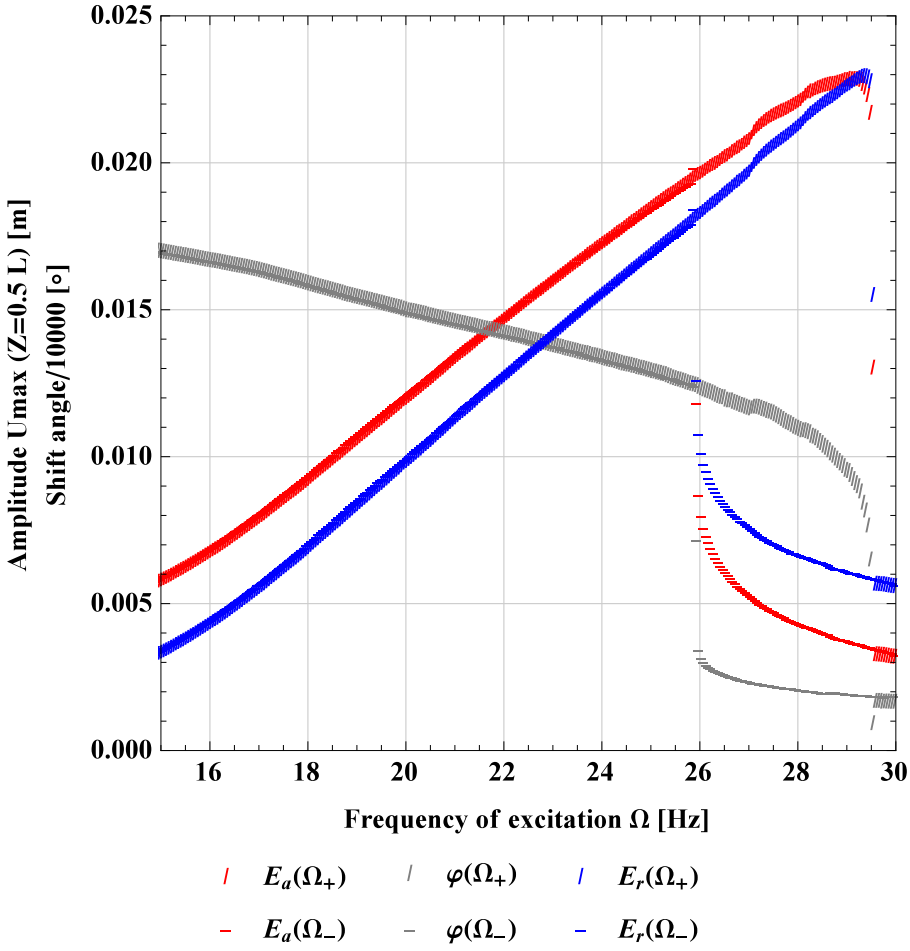

Figure 4.12: Frequency response curves and corresponding shift angle, $\boldsymbol{S}_{4.2}$.

Figure 4.12 shows preliminary experimental results for external excitation $\xi = 2.5$ mm. The frequency-amplitude curves are bend toward right (hardening nature), where the hysteresis of stable solutions appears between 26 Hz and 29.5 Hz ($\approx 1.5 \times \omega_1$). The shift angle decreases together with frequency of excitation increment. Jumps between upper and lower branches provoke a rapid change in the shift angle $\varphi(\Omega)$. In order to distinguish the increment/decrement if frequency change we introduce $E_r(\Omega_+)$ for sweep forward and $E_r(\Omega_-)$ for

sweep backward.

Experimental setup is located in the laboratory of Department of Applied Mechanics at Lublin University of Technology, and measurements were done in changeable environment throughout the day during a few weeks. Temperature conditions (between 20°C and 30°C) have a big impact on Teflon sleeves interaction and beam material properties. Another disadvantage in process of building the frequency response curves was replacing set of four springs. Despite all efforts, the system settings are different from the nominal ones, so the beam length and inclination angle slightly changes. Additionally the specimen tightening into hinge and shaft have not been perfect, consequently during table top movement the beam was continuously pulled out/pushed into handles, or mechanism of supporting part got stuck. The last doubt was about the condition of the sliding system and its abrasion over several months of testing. Differences in geometrical tolerance causes micro-impacts in the system and at least differ in the damping parameters of the structure. All of the above mentioned disadvantages affect dynamics of the system and they will be investigated in Section 5.3.

Chapter 5

Results

This Chapter is focused on the impact of variation an axial spring stiffness k_s on the dynamics of the system. Results for the two beams $\boldsymbol{T}_\kappa$ and $\boldsymbol{S}_\kappa$ are shown. First, outcomes of theoretical investigation on the beam $\boldsymbol{T}_\kappa$ is performed by finite element method and multiple time-scales method. Natural frequencies, backbone curves and frequency-amplitude curves for selected cases are compared. The analysis is not limited to primary resonance. Next, results are then supplemented by experimental tests based on kinematic excitation of the beam $\boldsymbol{S}_\kappa$ and its numerical counter part. This approach will enable to (indirectly) compare analytical, numerical and experimental methods.

5.1 Free oscillations

5.1.1 Linear dynamics

Substituting parameters of the beam $\boldsymbol{T}$ into equations (2.58)-(2.59) the first ten natural frequencies of the system are computed for the hinged-hinged/hinged-simply supported beams and then compared in Table 5.1.1. From practical point of view the discrepancy is negligible, since differences occur at higher frequencies. It is caused by the numerical approximations and are less than 1‰. It could be improved by more accurate discretization, nevertheless results are satisfactory for our purpose.

As mentioned before, transversal natural frequencies and corresponding mode shapes of the structure are independent of boundary conditions, but the axial spring is very important for longitudinal dynamics. Figures 5.1 and 5.2 display change in natural frequency and the beam deformation ratio. The simply supported beam has the lowest natural frequency. As the parameter κ increases, the natural frequency tends to the highest value, which corresponds to hinged-hinged beam ($\kappa = \infty$). In vicinity $\kappa = 0$ the system is more susceptible to changes and increasing the stiffness the sensitivity decreases.

Furthermore, the biggest longitudinal deformation of the node 101 occurs with no spring (Fig. 5.2), while a slight change in κ shifts the largest deflection

Table 5.1: Mode shapes and corresponding natural frequencies of the beam $\boldsymbol{T}$. Notation (h-ss) corresponds to hinged-simply supported boundary conditions and (h-h) describes hinged-hinged beam.

Mode No.	Mode shape	Natural frequency [Hz]		Difference [‰]
		FEM	Analytic	
1	1st bending	461.47	461.47	0.003
2	2nd bending	1764.50	1764.57	0.040
3	1st	2586.10 (h-ss)	2586.10 (h-ss)	0.000
	longitudinal	5172.00 (h-h)	5172.19 (h-h)	0.037
4	3rd bending	3720.40	3720.62	0.059
5	4th bending	6129.30	6129.35	0.171
6	2nd	7757.60 (h-ss)	7758.29 (h-ss)	0.089
	longitudinal	10343.00 (h-h)	10344.40 (h-h)	0.135
7	5th bending	8833.40	8836.46	0.346
8	6th bending	11723.00	11730.10	0.605
9	3rd	12927.00 (h-ss)	12930.50 (h-ss)	0.271
	longitudinal	15511.00 (h-hh)	15516.60 (h-h)	0.361
10	7th bending	14726.00	14740.10	0.957

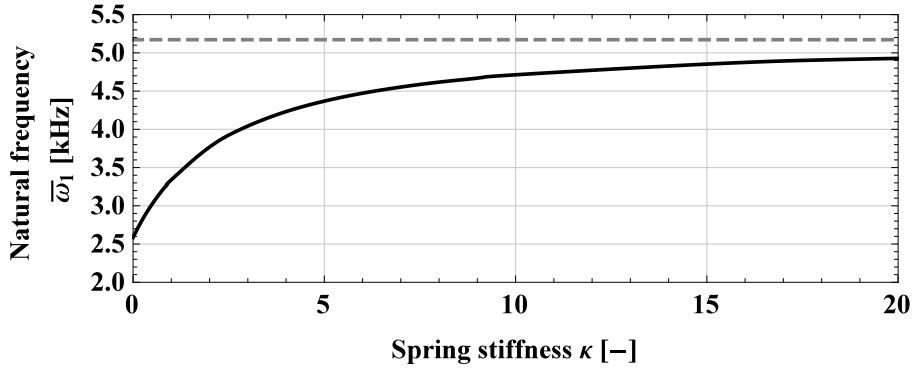

Figure 5.1: An axial spring influence on the first natural frequency of the system, dashed line coincides with the hinged-hinged beam $\boldsymbol{T}$.

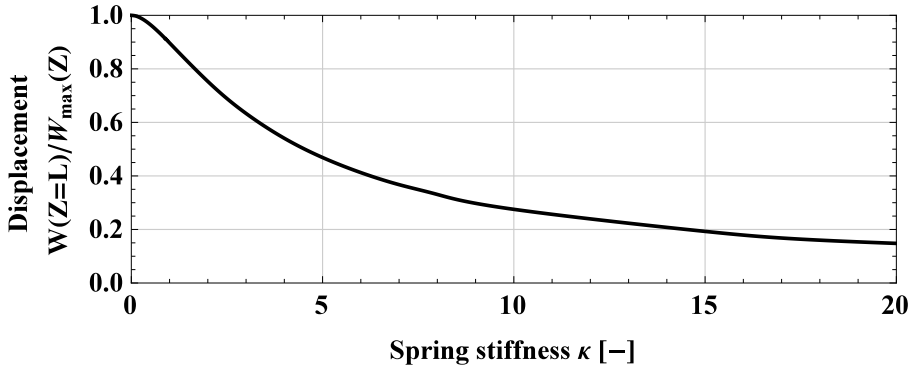

Figure 5.2: The axial spring influence on axial displacement of the beams end vs maximum longitudinal deflection of the beam. Properties of the beam $\boldsymbol{T}$.

forward center of the beam. Finally the hinged-hinged beam has restrained both ends and the relation $W(Z = L)/W_{max}(Z)$ goes to zero, as can be seen from mode shape in Fig. 3.3d.

5.1.2 Nonlinear dynamics

When amplitudes of vibrations increase, the linear analysis becomes less and less accurate. The nonlinear frequency of the system can vary together with amplitude of oscillations [6, 90, 120] and analysis need to be extended to nonlinear dynamics. Section 2.2 was focused on derivation the frequency response equation (2.92) and backbone curve equation (2.93) which links all geometrical and material properties of the structure. In the first attempt to validate analytical derivation on the beam model, the comparison of backbone curves with literature findings, based on Linsted-Poincaré method is performed in Fig. 5.3. The results are in a very good agreement, minor discrepancies occur only for small values of spring stiffness $k_s = 50000000N/m$ ($k_sL/EA = 0.012$) or in the absence of the spring $k_s = 0$.

At this stage we are focused on the comprehensive analysis of the beam $\boldsymbol{T}$ and check its hardening/softening behaviour for free oscillations. For this purpose we depict the nonlinear correction coefficient c_b as a function κ in Figures 5.4 and 5.5. For the first bending mode for $\kappa = 0$ the nonlinear correction coefficient is negative. It means that the beam $\boldsymbol{T}_0$ has the softening behaviour. For increasing spring stiffness coefficient $c_b(n = 1)$ intersects the abscissa (linear oscillations) in $\kappa \approx 0.018$, see Fig. 5.4_b. With further k_s growth the c_b monotonically (for $n = 1$, $n = 3$, $n = 4$, $n = 5$) tends to the fixed value corresponding to the axially restrained beam. At $\kappa \cong 10$ the difference with the

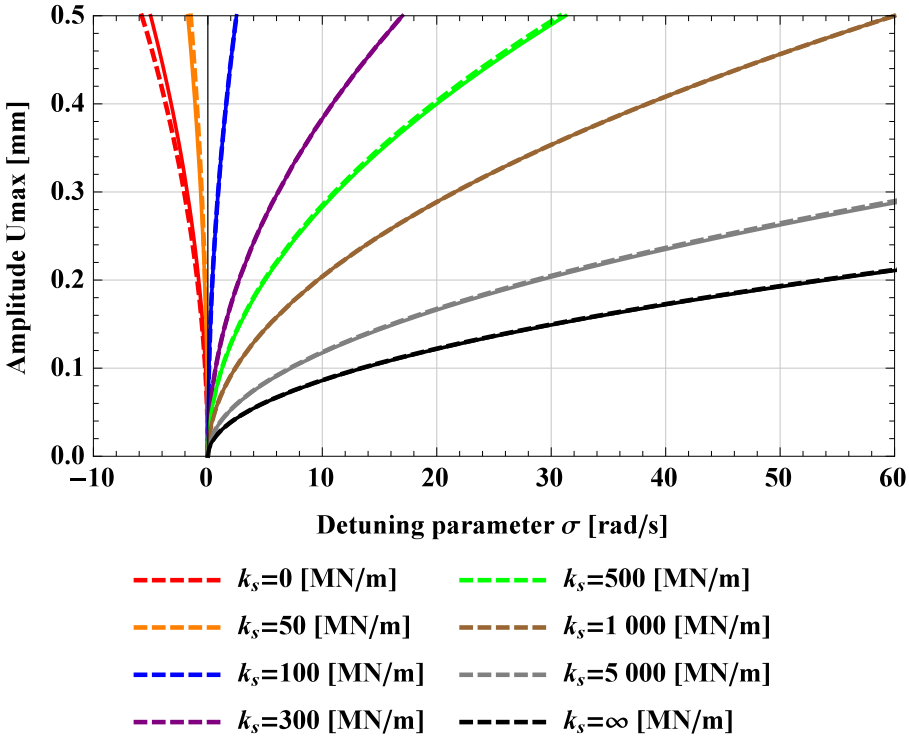

Figure 5.3: Multiple time scales method (solid lines) vs Linsted-Poincaré method (dashed) backbone curves for beam properties: $L = 5$ m, $H = 0.5$ m $B = 0.2$ m, $\rho = 7850$ kg/m^2, $E = 2.11\ 10^{11}$ N/m^2, $0 \leq k_s < \infty$, $EA/L = 4.22\ 10^9$ N/m [70, 76].

asymptotic limit is less than 4%. For all values of k_s the third, fourth and fifth modes have only hardening nature. For the hinged-hinged beam all c_b parameters are positive, and they gradually increase with successive n values. In other words, the beam $\boldsymbol{T}_\infty$ have stronger hardening effect for gradually higher order modes. Considering comparable amplitudes of oscillations for two consecutive modes, the frequencies are shifted more to the right ($+\sigma$) with respect to the natural (linear) one (ω_n).

The c_b for the second mode is principally positive (hardening), beside a small interval around $\kappa \simeq 1.382$, where the curve has a singularity and goes to $\pm$ infinity. It is caused by a denominator that crosses zero, together with a non-zero numerator. Similar cases are detected for sixth and seventh modes, their singular values are for $\kappa \approx 1.61$ and $\kappa \approx 12.99$, respectively. Due to uncertainty of the result, our analyses in this interval will be performed by finite element method in forced-damped case.

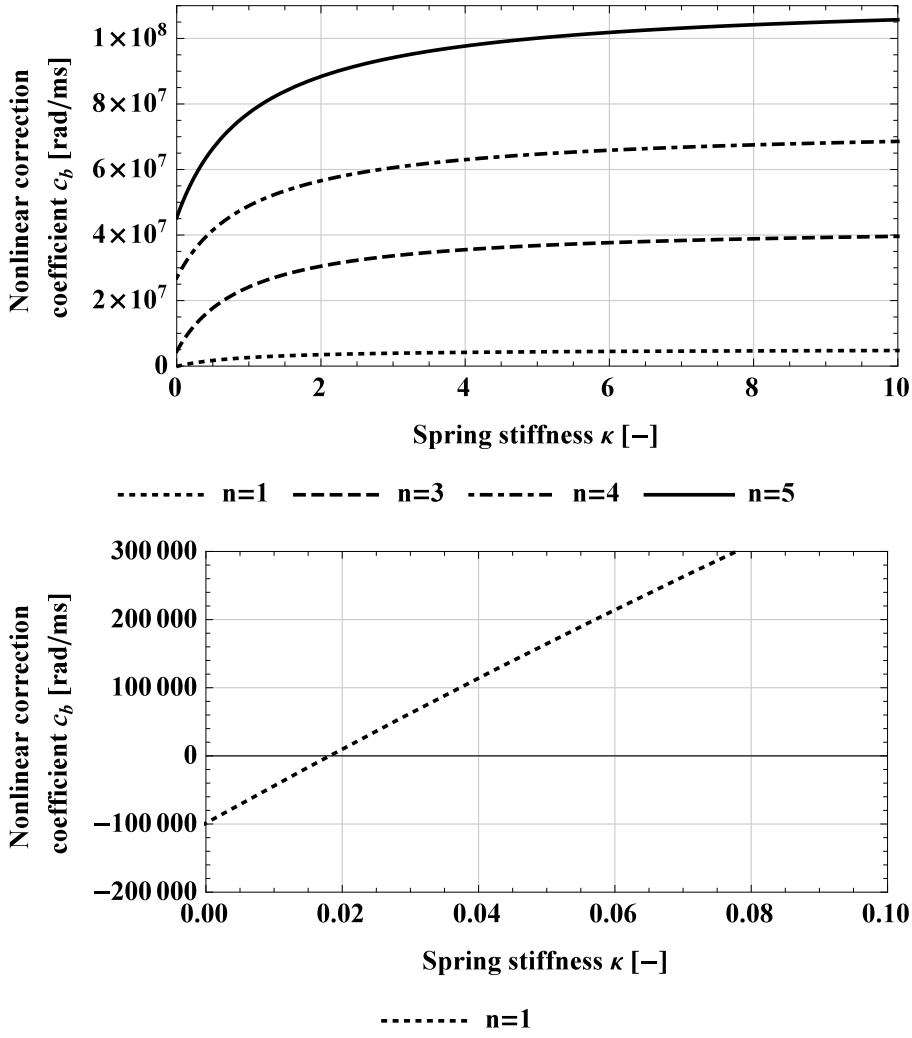

Figure 5.4: The nonlinear correction coefficients c_b for the beam $\boldsymbol{T}$.

For selected cases of spring stiffness the backbone curves are presented in Figures 5.6-5.12. It directly correlate the nonlinear correction coefficient with frequency-amplitude relations. Additionally, in Fig 5.6 analytical results are compared with outcomes of numerical simulations performed in Section 3.3.1. Verification of finite element method and multiple time-scales method shows very good agreement, even though for large amplitudes there are some discrepancies due to the influence of higher order modes, which has not been eliminated in numerical simulations because of the particular initial (static) configuration

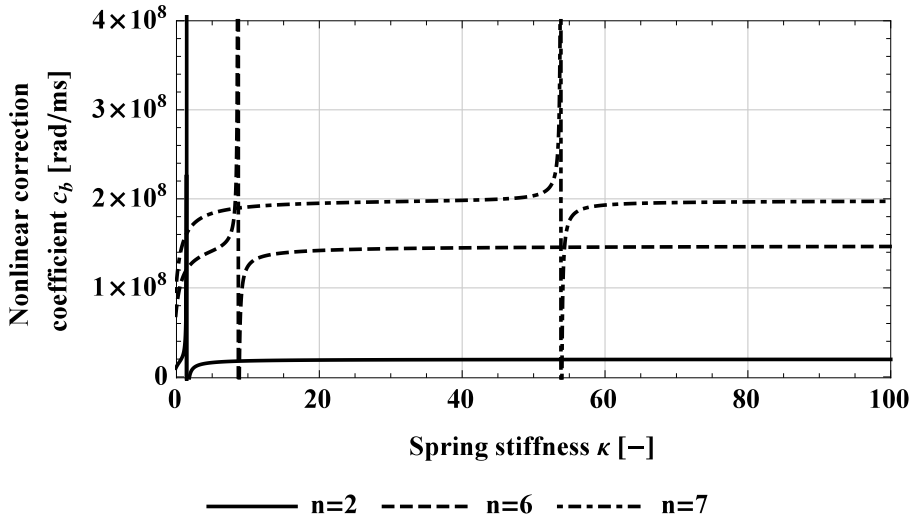

Figure 5.5: First three singularities of the nonlinear correction coefficients for the beam $\boldsymbol{T}$. More cases of singular points ($c_b = \pm\infty$) are expected for higher order modes, but not for higher stiffnesses of presented mode numbers.

from which the free vibrations start. It can mix different frequencies, e.g. $n = 1$ and $n = 3$ [121]. Inaccuracy of initial deformation shape is smoothly corrected in time by the damping. It is however remarkable that amplitudes smaller than 0.01 m (20% of beams thickness and 1% of the length) brings an excellent agreement, higher order frequencies are disappearing fast and only one main frequency remains. Nevertheless, very interesting phenomenon occurs for spring stiffnesses $\kappa = \infty$ and $\kappa = 4$, for interval between 530 Hz and 545 Hz, markers are arranged in linear trends. It can be expected that they will follow the regular mode until the vibrations disappear, but the signal becomes again diffused and then stabilize once again. This effect is different from other cases, where the numerical results asymptotically tend to analytical predictions. It is probably an additional interaction between other modes, which was not considered in analytical modeling. Furthermore, the beam $\boldsymbol{T}_\kappa$ with the same spring stiffnesses will be studied in Section 5.2 where in contrary to free-damped oscillations, a gradual increment of amplitude response enables to follow paths in a wider frequency spectrum of external excitation with much smaller dispersion of measuring points.

Free nonlinear oscillations for the second flexural mode ($n = 2$) of the beam $\boldsymbol{T}\kappa$ are shown in Fig. 5.7. Note that, the singularity in nonlinear correction coefficient displayed in Fig. 5.5 causes exit of some solutions from two limit

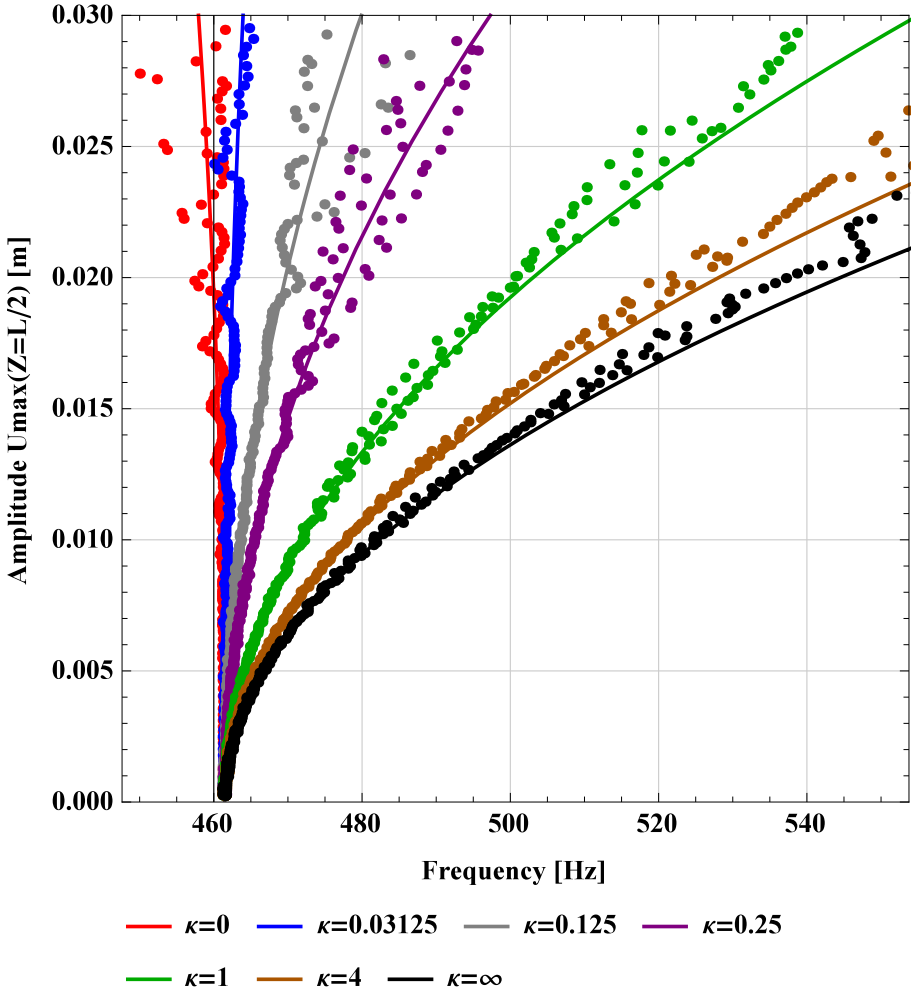

Figure 5.6: Backbone curves of the beam $\boldsymbol{T}$, $n = 1$. Lines are multiple time-scales method and dots are finite element simulations.

values related to parameters $\kappa = 0$ and $\kappa = \infty$. Relatively large values (positive and negative) of $c_b(\kappa)$ occur for $\kappa \approx 1.382$, which significantly changes the behaviour of the structure. Slightly smaller values ($\kappa = 1.3$) backbone curves have very strong hardening nature, but for a little bit greater spring stiffness the response of the beam represents softening behaviour ($\kappa = 1.6$). Far away from the critical spring stiffness the structure behaves like for the first bending mode, although amplitudes are smaller. Comparing responses of hinged-hinged beam for $\sigma = +86$ Hz the difference is about 50%. This case will be studied in Section 5.2.2 by the path following method.

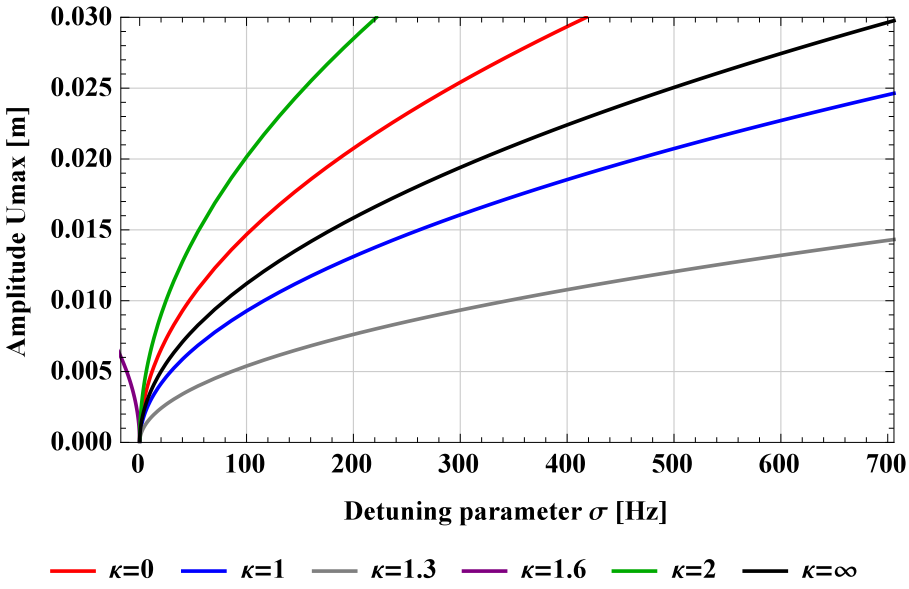

Figure 5.7: Backbone curves of the beam $\boldsymbol{T}$, $n = 2$.

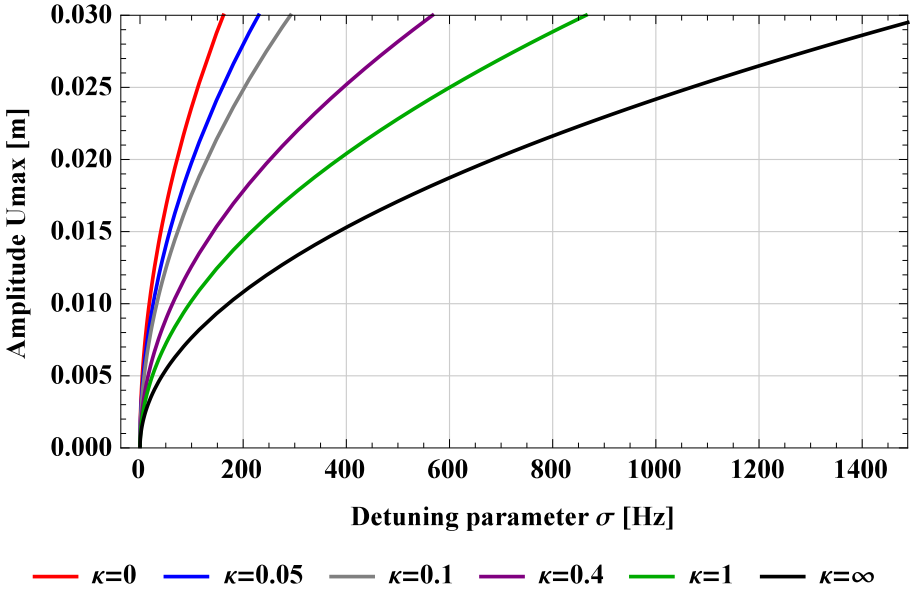

Figure 5.8: Backbone curves of the beam $\boldsymbol{T}$, $n = 3$.

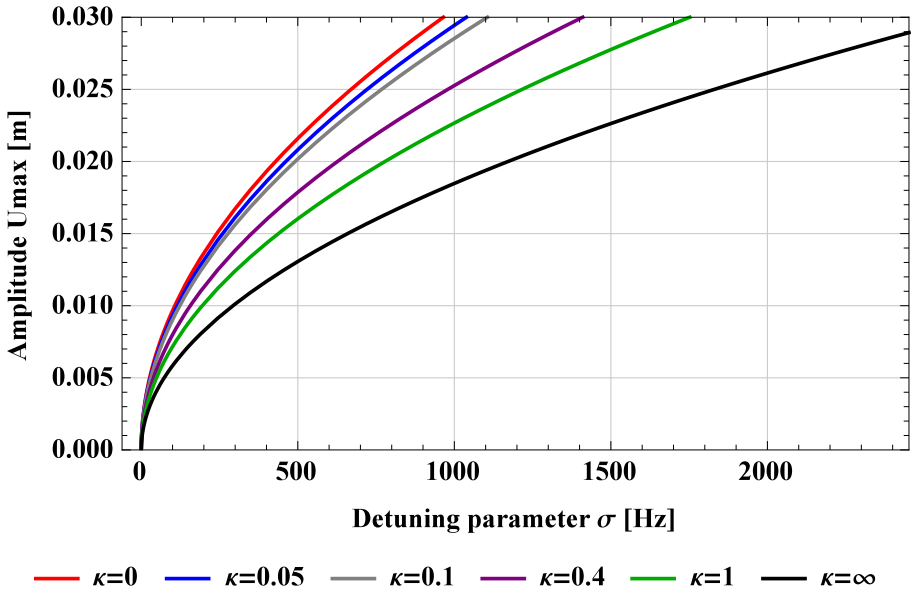

Figure 5.9: Backbone curves of the beam $\boldsymbol{T}$, $n = 4$.

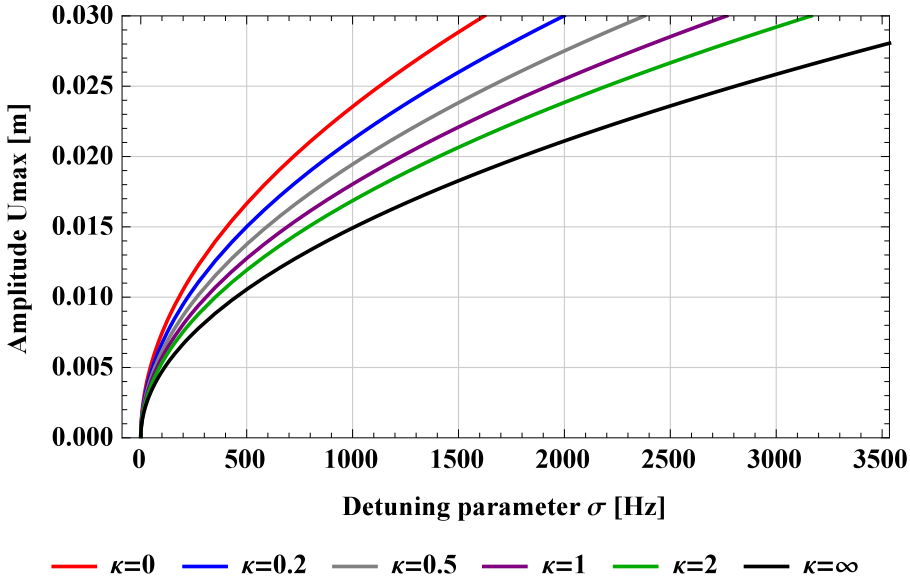

Figure 5.10: Backbone curves of the beam $\boldsymbol{T}$, $n = 5$.

The third, fourth and fifth bending modes do not have above mentioned anomalies. For all spring stiffnesses in the range $0 \leq k < \infty$ the beam represents only hardening phenomenon, see Figs. 5.8, 5.9 and 5.10. A gradual change in κ bends backbone curves more and more to the right for all three cases. Large amplitudes of oscillations require getting further away from resonance for higher order resonances e.g. amplitude 25 mm (0.5 thickness of the beam) for the simply supported (hinged-hinged) correspond to detuning parameter $\sigma(n = 3) = 120 rad/s$, $\sigma(n = 4) = 680 rad/s$ and $\sigma(n = 5) = 1040 rad/s$ ($\sigma(n = 3) = 1050 rad/s$, $\sigma(n = 4) = 1850 rad/s$ and $\sigma(n = 5) = 2800 rad/s$), respectively.

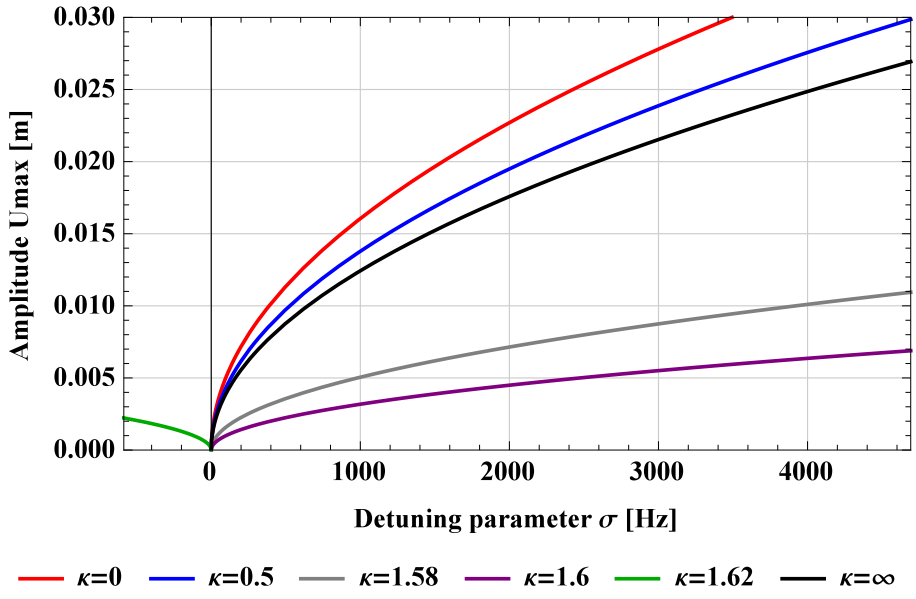

Figure 5.11: Backbone curves of the beam $\boldsymbol{T}$, $n = 6$.

The sixth and seventh resonant (bending) modes are also unsettled in vicinity of critical spring stiffnesses, which are presented in Fig. 5.5. For precisely selected parameter κ amplitudes of vibrations are approaching to zero, e.g. $\kappa(n = 6) = 1.6 \pm 0.02$ mm (see Fig. 5.11) and $\kappa(n = 7) = 13.0 \pm 0.1$ (see Fig. 5.12). It means that transverse oscillations near singularities vanish, which is incomprehensible at this stage and further analysis should be done by different methods to validate and better understand this particular phenomenon.

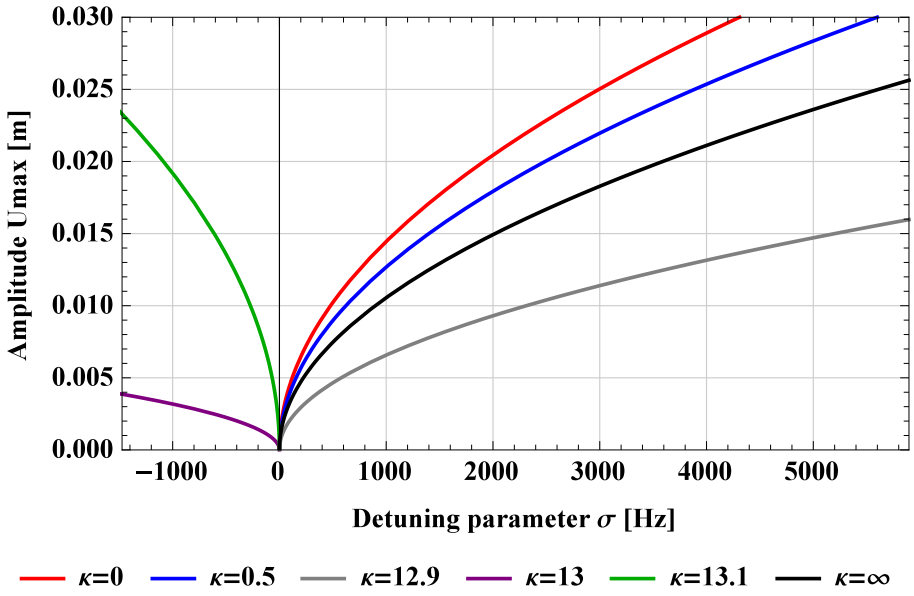

Figure 5.12: Backbone curves of the beam $\boldsymbol{T}$, $n = 7$.

5.2 Forced-damped vibrations

With the external exictation presence the structure possess more diversified nonlinear dynamics than in the case of free oscillations. A response of the nonlinear system has stable and unstable solutions, which depend on the ratio between the natural frequencies and the frequency of excitation [87]. The dynamics are further influenced by initial and boundary values of the problem [3]. In this Section we consider two cases of excitation:

- to directly trigger the first bending mode (symmetric), the cyclic vertical force is applied in the midpoint, $c_z = 2$;
- to study first, second and third (symmetric and asymmetric) modes the concentrated periodic force is positioned at one fourth of the span, $c_z = 4$.

First point is an excellent way to investigate odd-modes, but at the same time it prevents analytical even-modes analysis. For the same reason second point is excluded for integer multiplicity of $n = 4$.

5.2.1 Excitation in the midpoint

Figure 5.13 shows frequency response curves of primary resonance for the beam $\boldsymbol{T}$. Results are obtained from frequency response equation Eq. (2.92) and

numerical simulations described in Section 3.3.2. Accordingly with previous analysis, starting from the strongest hardening of hinged-hinged beam, then as spring stiffness decreases the frequency response curve straightens and finally for unrestrained beam characteristics bends slightly towards left, showing a softening behaviour. Markers, which present numerical solutions, overlap solid lines for detuning parameter range -50 Hz $< \sigma <$ $+50$ Hz even for large amplitudes. Differences increase for frequencies greater than $+100$ Hz. The reasons of divergence are

- analytical approach is suitable for small values of detuning parameter, while the range of the plot is in wide interval $-0.1\omega_1 < \sigma < +\omega_1$ [90];
- the multiple time-scales method is applied up to second order approximate solution (cubic nonlinearities), higher order approximation of the exact beam model can possess higher accuracy of the frequency response curves [66];
- finite element method is not limited to the individual nth mode, but interacts simultaneously with a finite number of modes of the system [77].

Further analysis shows that upper branches of numerical solution for $\kappa = 4$ and $\kappa = 1$ are featured by two local peaks in $\sigma = 185$ Hz and $\sigma = 340$ Hz. Time histories of those peaks are used to carry out discrete Fast Fourier Transform (FFT) analysis [122]. Displayed in Fig.5.14$_b$ the Fast Fourier Transform (FFT) indicates two main amplitude peaks in $\omega(\kappa = 4) = 646$ Hz and $\omega(\kappa = 4) \approx 1938$ Hz as well as $\omega(\kappa = 1) = 796$ Hz and $\omega(\kappa = 1) \approx 2388$ Hz. Those values correspond to the frequency of excitation (left peak) and indirectly excited another nonlinear mode (right peak). It is worth to remark that the even modes are not excited by external force, they interact among themselves by nonlinear terms, for instace inertia. We also highlight that $1938/646 = 3$ and $2388/796 = 3$ showing that we are dealing with a 1 to 3 superharmonic resonance. Examples on this phenomenon can be found in [123–126].

We believe that peak disturbances are cased by time sampling together with location of the recording signal (almost at the node of the second nonlinear bending mode) and do not have an extra mechanical background.

To better understand this phenomenon, the concentrated force is relocated from $c_z = 2$ to $c_z = 4$. This manner allows to pump energy directly into even as well as odd modes and to study more frequency response curves.

5.2.2 Asymmetrical excitation

Primary resonance

In this case, the harmonic external excitation is applied at $Z = L/4$, the frequency range is reduced to $-0.2\omega_1 < \sigma < 0.5\omega_1$. Also amplitude of excitation

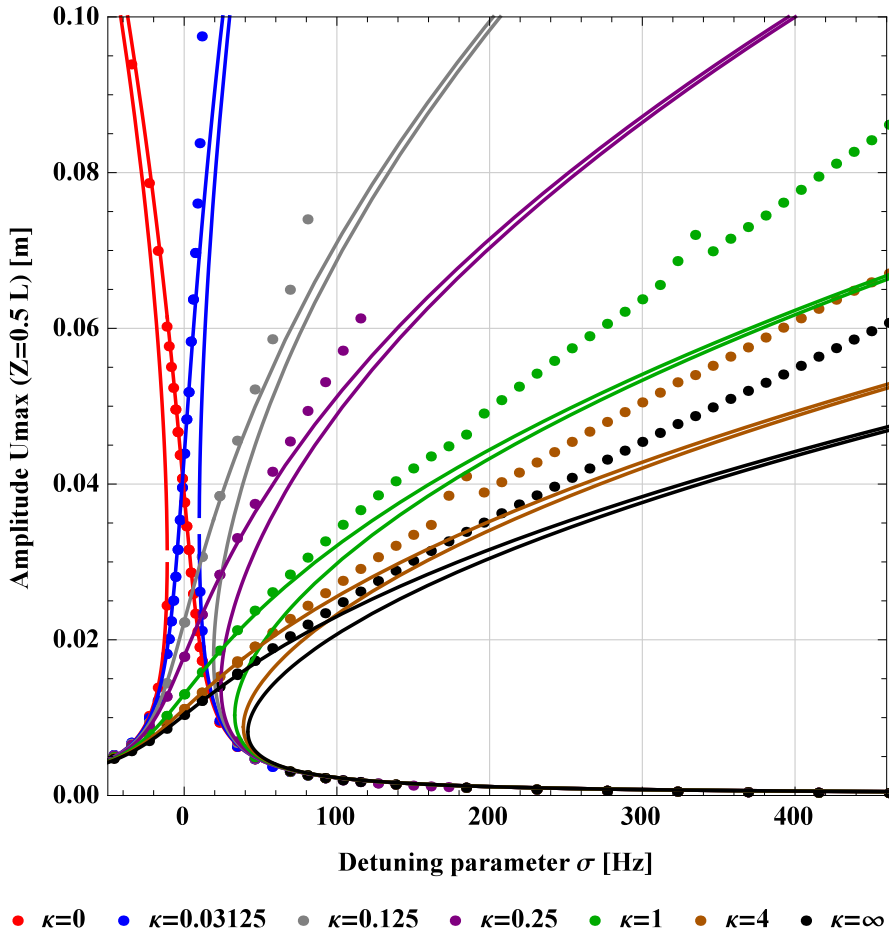

Figure 5.13: Frequency response curves: multiple time-scales method (lines) vs finite element method (dots); beam $\boldsymbol{T}$, $n = 1$, $c_z = 2$, $P_v = 40799.2$ N, $\zeta = 6$ %.

P_v is adjusted to enforce midpoint quasi-static deflection about 1 mm (2% of least radius of gyration) for the hinged-hinged beam $\boldsymbol{T}$.

Frequency response curves in the neighborhood of the first bending mode are shown in Fig. 5.15. Differences between analytical and numerical results increase as the detuning parameter increases. Significant deviation of the curves begins at 75 Hz for $\kappa = 0.25$ and 150 Hz for $\kappa = 1$, $\kappa = 5$ as well as $\kappa = \infty$. For assumed amplitude of excitation and damping coefficients the bifurcation exists for axial spring stiffness greater than 0.5% of beams tensile stiffness. An additional jump in solution occurs for $\kappa = 1$. Time histories of points

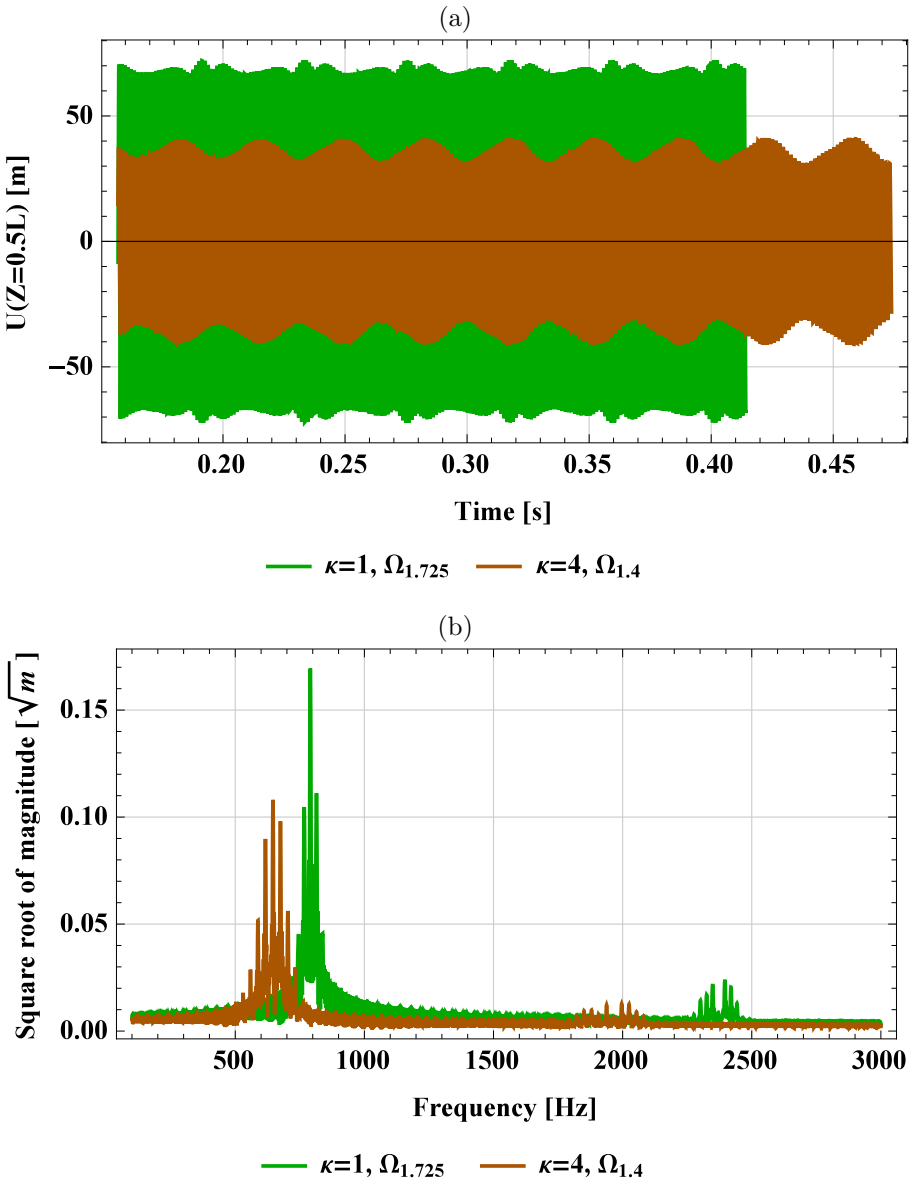

Figure 5.14: Steady state time history for $\kappa = 1$, $\Omega = 796.04$ Hz and $\kappa = 4$, $\Omega = 646.06$ Hz (a). Time is measured for a given frequency of excitation, preceding signal eliminates transience. Fast Fourier transform (b) of selected time intervals: 2^{13} points.

marked by the black diamond and circle are investigated by FFT in Fig. 5.16. Single strong peaks are observed for points marked by rectangle and diamond.

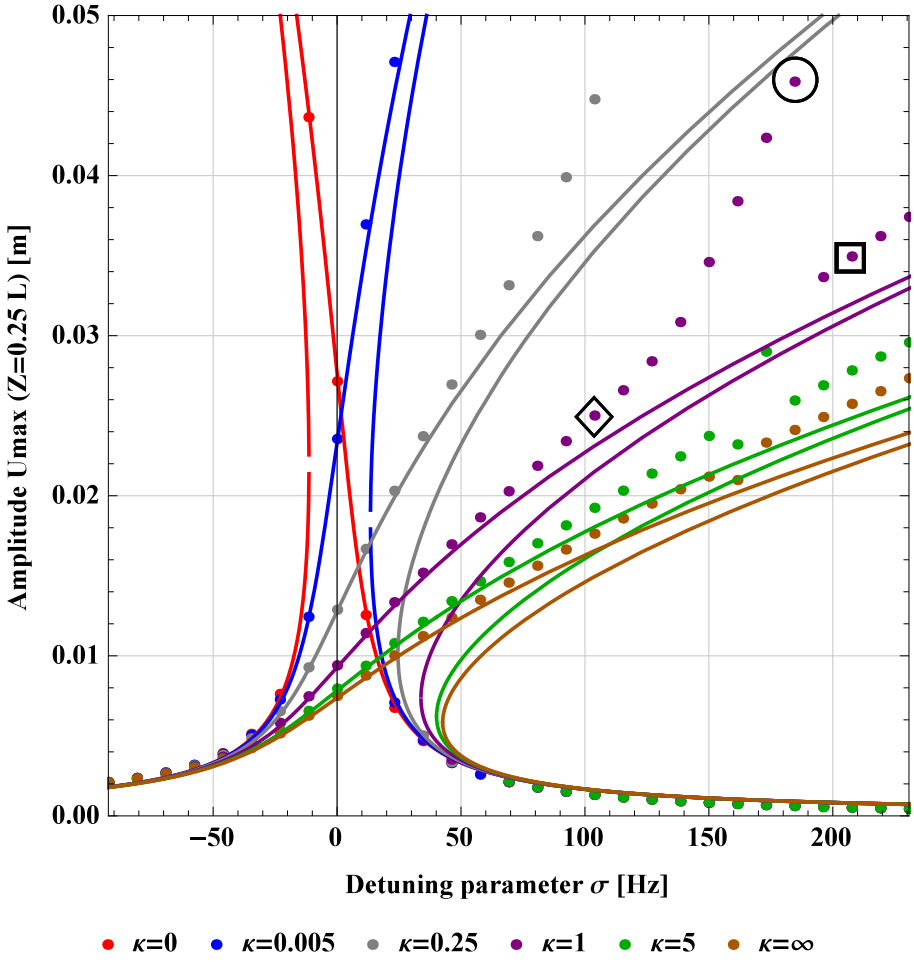

Figure 5.15: Frequency response curves: multiple time scales method (lines) vs finite element method (dots); beam $\boldsymbol{T}$, $n = 1$, $c_z = 4$, $P_v = 59839.5$ N, $\zeta = 6$ %.

Additionally the series marked with diamond has a negligible small peak about 1650 Hz. The circled time history has two major peaks, occurring at frequencies $\omega = 654$ Hz and $\omega = 1940$ Hz, whose ratio is again 1 to 3, showing again a superharmonic bending-bending internal resonance. Second mode participation in time history in $\Omega_{1.2}$ is marginal, and the amplitude of the second peak increases by increasing the frequency, up to the last acquired value. At $\Omega_{1.4}$ maximum values ratio is 6.75/16 (42%!) and for next computational frequency $\Omega_{1.425}$ the maximum amplitude jumps to single-frequency solution path, where it has only one peak in the FFT.

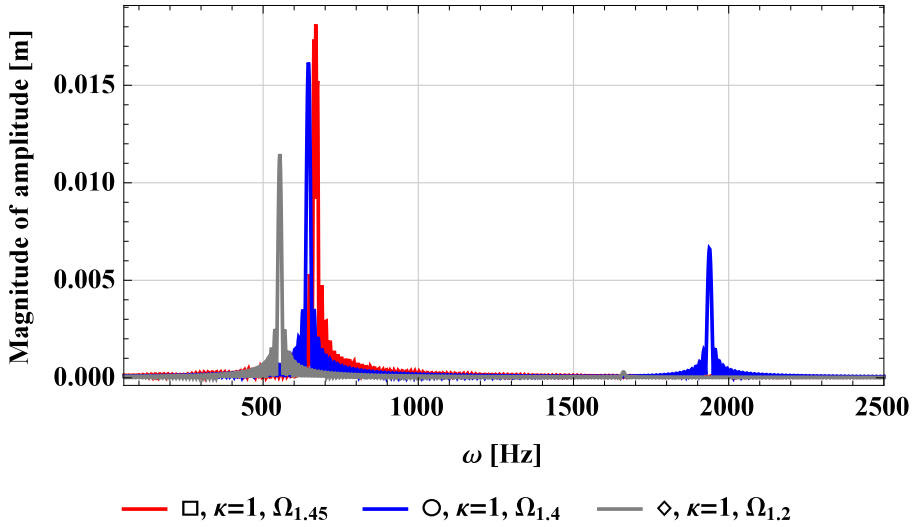

Figure 5.16: Fast Fourier transform of three time histories marked by diamond, circle and rectangle in Fig. 5.13. Time interval consists of 2^{12} points recorded with sampling $1/(40\Omega)$.

Since the interval 150 Hz$< \sigma <$ 200 Hz may have an additional solution, the shooting method is used to look for further branches with lack of internal resonance. As said in Section 3.3.3 the shooting method can be used for a predefined narrow range of initial conditions and frequency spectrum. This method saves computational time with respect to path following method, because there is on need to start simulation from resonant frequency and follow the stable path up to the $\sigma = 200$ Hz and then sweep backward. The investigation is made directly in the specified range.

The initial deformations of the beam $Umax_{m,n}(U0_m, \Omega_n)$ have been set as in Table 5.2, where m describes initial maximum deformation of the beam midpoint (in millimeters) and n denotes the ratio of frequencies Ω/ω_1.

Only underlined values of initial conditions lead to solutions presented in Fig. 5.17. It shows how precisely the initial deformation of the structure have to be predefined and how easily stability of the solution can be lost. Figure 5.18 displays time histories of the 26th node, despite starting nearby stable branch after sufficient time amplitude goes to the lower non-resonant amplitude.

Nevertheless, phenomenon of nonlinear internal resonance is confirmed. The results can be described as an additional higher order nonlinear resonance which is built on the primary one and their frequencies ratio 1 to 3. Let us refer to a few works, which are related to this phenomenon and are investigated by different approaches [127–130].

Table 5.2: Initial conditions of shooting method.

n	m									
1.4	45	46	47	48	49	50	51	52	53	54
1.375	40	41	42	43	44	45	46	47	48	49
1.35	40	41	42	43	44	45	46	47	48	49
1.325	40	41	42	43	44	45	46	47	48	49

Secondary resonance

Study on secondary resonance is performed with the same methods as for primary resonance, the only differences are in parameter κ and frequency of excitation Ω, which is varied in between $-0.05\omega_2$ and $+0.13\omega_2$. In this case outcomes of numerical and analytical computations are divided in two parts, first far away from the singularity and second in its close proximity. The critical κ is about 1.382 and investigated values of the parameter are marked in Fig. 5.19 on both sides of the singular point where the coefficient $c_b(\kappa \approx 1.382)$ goes to $\pm\infty$. In this specific range, presented technique of multiple time-scales method does not have physical meaning, because internal resonances have not been considered in our simulations.

Let us discuss the results presented in Fig. 5.20. All frequency response curves have hardening nature. The smooth change between the two limit values $\kappa = 0$ and $\kappa = \infty$ is broken by approaching the singular point ($\kappa = 1.382$ in between $\kappa = 1$ and $\kappa = 2$). Out of this interval, since the multiple time-scales and finite element methods have analogous results, we can assume their correctness. A slight change in the nonlinear correction coefficient for beams $\boldsymbol{T}_{100}$ and $\boldsymbol{T}_{200}$ generates almost indistinguishable modifications of the analytical frequency-amplitude curves.

Frequency response curves for spring stiffnesses close to the singular point (together with hinged-hinged and hinged-simply supported beams reported for reference) are displayed in Fig. 5.20. Divergent results are obtained for $\kappa = 1.5$, $\kappa = 1.6$, $\kappa = 1.7$ and $\kappa = 1.75$. In those cases the spring system has only softening nature (see Fig. 5.21), although by decreasing spring stiffness below the critical spring stiffness $\kappa = 1.382$ the hardening behaviour of the structure is available as well. Nonlinear dynamics of the beam is in qualitative agreement, approaching the singular point from larger values of spring stiffness, as we observe the frequency response curve tilts more and more to the left, according to the fact that the system becomes more and more softening, because c_b tends to $-\infty$. Apart from $\kappa = 1.75$, analytical and numerical methods give equivalent

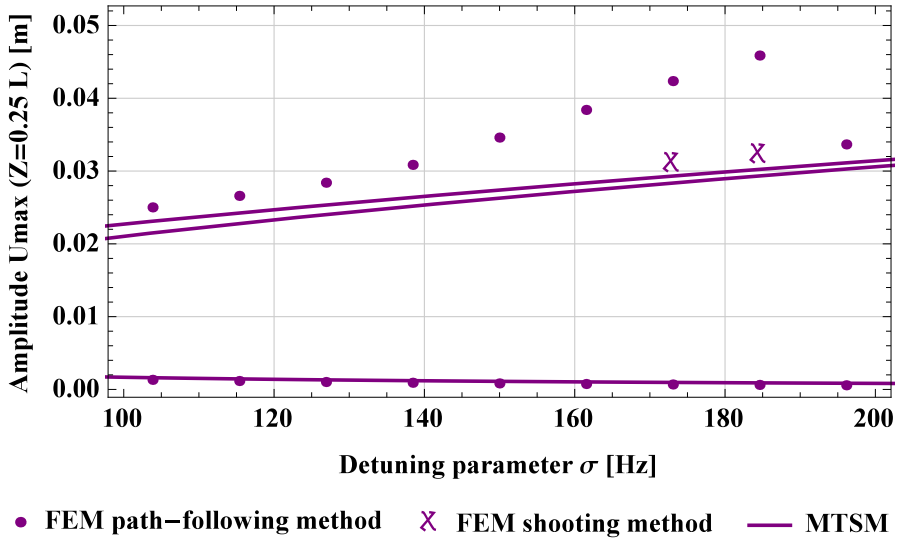

Figure 5.17: Three stable solutions of the system $\boldsymbol{T}_{100}$, computations completed by the shooting method.

amplitudes in $\sigma = 0$, but unfortunately are in quantitative conflict for large detuning parameter. Even small amplitudes of oscillations become questionable in this particular range.

Assuming that perturbation method is correctly balanced only for $\Omega_1(\sigma = 0)$, we focus on the continuation by finite element method and inspect time histories of selected points. Case $\kappa = 1.5$, $n = 2$ attracted our attention because it is closest to the critical point $\kappa = 1.382$. In the plotted interval it has three sets of points:

- -50 Hz $< \sigma < -33$ Hz, solutions of lower amplitudes of oscillations (up to 3 mm), with analytical counterpart;
- -33 Hz $< \sigma < +12$ Hz, there is only one path of higher amplitudes which is in qualitative agreement with analytical frequency response curves;
- $+12$ Hz $< \sigma < +50$ Hz, maximum amplitudes are spreaded with with no analytical counterpart.

The three frequencies are marked by diamond, circle and rectangle are now deeply investigated; their transient time histories and Fast Fourier Transforms are plotted in Fig. 5.21. The diamond and circle responses start from slightly disturbed initial conditions and stabilize smoothly, amplitudes of longitudinal/transverse oscillations go to constant amplitudes within less than half sec-

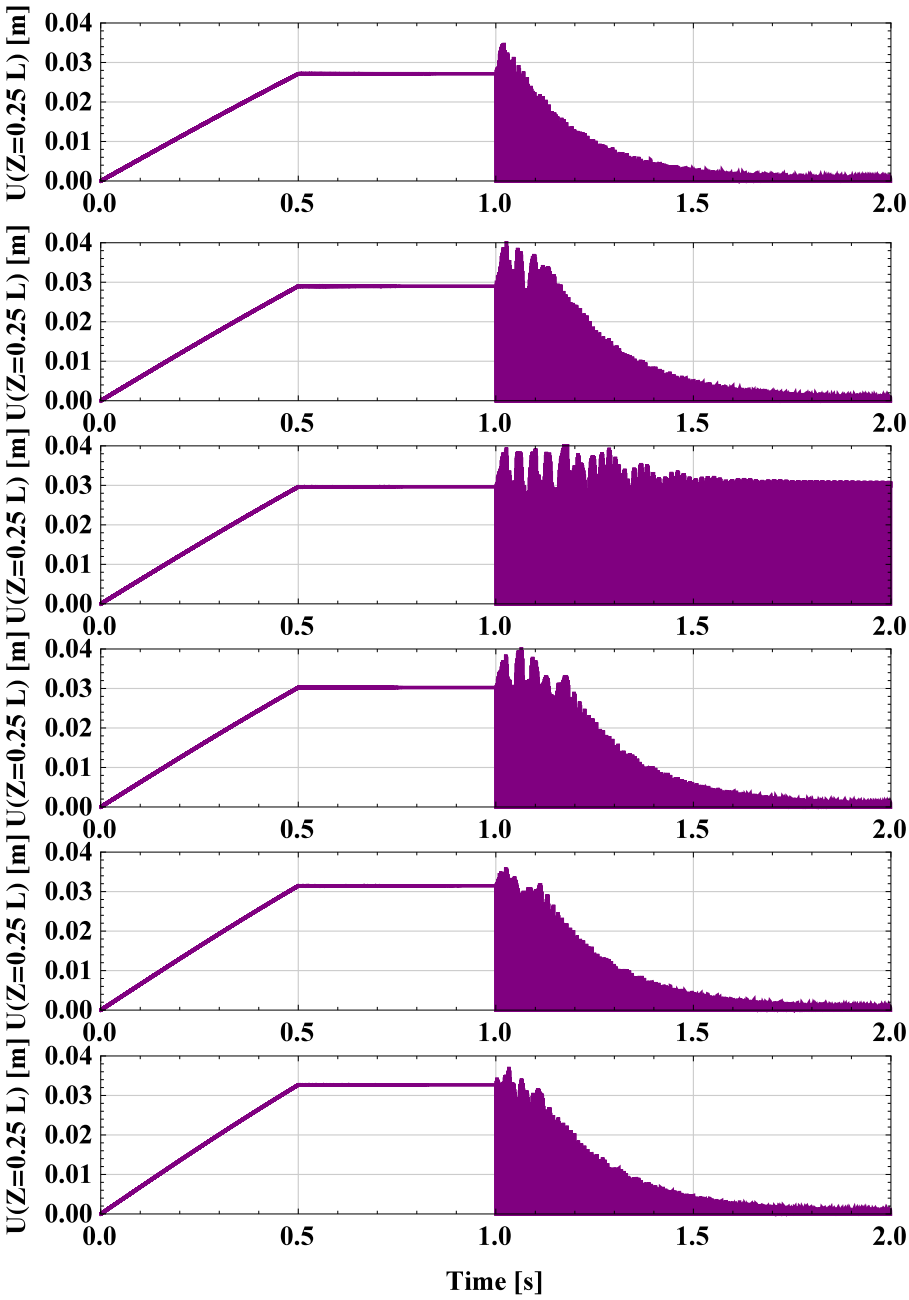

Figure 5.18: Time histories of shooting method for $\Omega_{1.375}$, from top to bottom: $m = 42$, $m = 44$, $m = 45$, $m = 46$, $m = 48$, $m = 50$; the beam $\boldsymbol{T}_{100}$, $n = 1$, $c_z = 4$, $P_v = 59839.5$ N, $\xi = 6$ %.

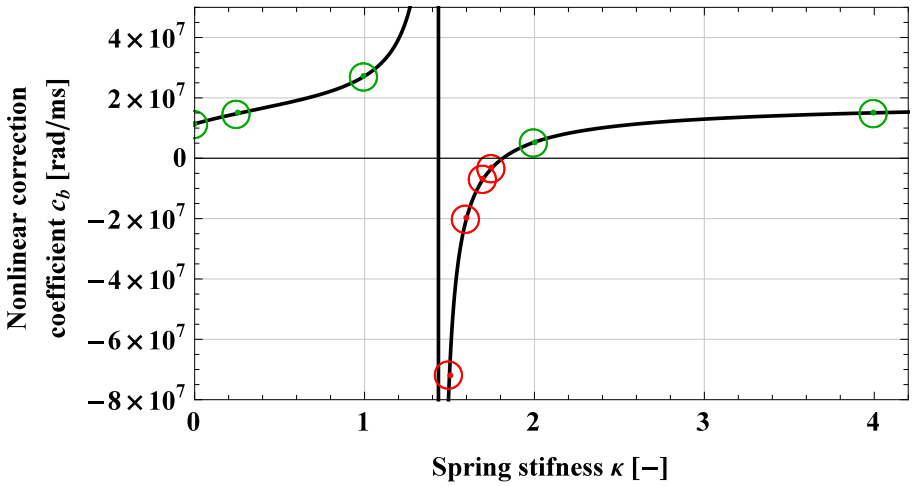

Figure 5.19: The singularity of nonlinear correction coefficient (curved line) for the second bending mode of the beam $\boldsymbol{T}$. Round markers correspond to certain (green) and uncertain (red) investigated cases.

ond. Constant amplitudes ratios $W(Z = 0.25L)/U(Z = 0.25L)$ are 6/195 (diamond) and 2/9 (circle). Second proportion is about 22% and clearly shows that axial vibrations are excited. Both cases have clear peaks of amplitude, which are related to the frequency of excitation in transverse direction and double frequency in longitudinal one. Due to symmetry of the system the natural periods are in ratio 1 to 0.5.

The crucial part of this work is the analysis of the case marked as a square. Time histories show that energy transfer exists from the excited transverse mode to an axial one and viceversa. When transverse oscillations go to maximum amplitudes the longitudinal ones are disappearing, when axial vibration increases the flexural mode suddenly vanishes in correspondence of the maximum axial amplitudes. For third set of points, which are responsible for beating phenomenon, maximum amplitudes in Fig. 5.21 are read (maximum amplitude of the long time simulation), while their counter part in axial direction is zero. The beating phenomenon occurs in the studied system when the flexural natural frequency is very close to one half of natural frequency in longitudinal direction. Various examples of beating can be found in [131–134]. This interesting mechanism is robust and repeatable not only for the first mode. The singularities of nonlinear correction coefficient c_b (see Fig. 5.5) now are understood as an interaction between axial/transverse internal resonances. The first peak corresponds to the first longitudinal $\overline{\omega}_1$-second bending ω_2 modes; second peak to the second axial $\overline{\omega}_2$-sixth transverse ω_6 modes; third peak to

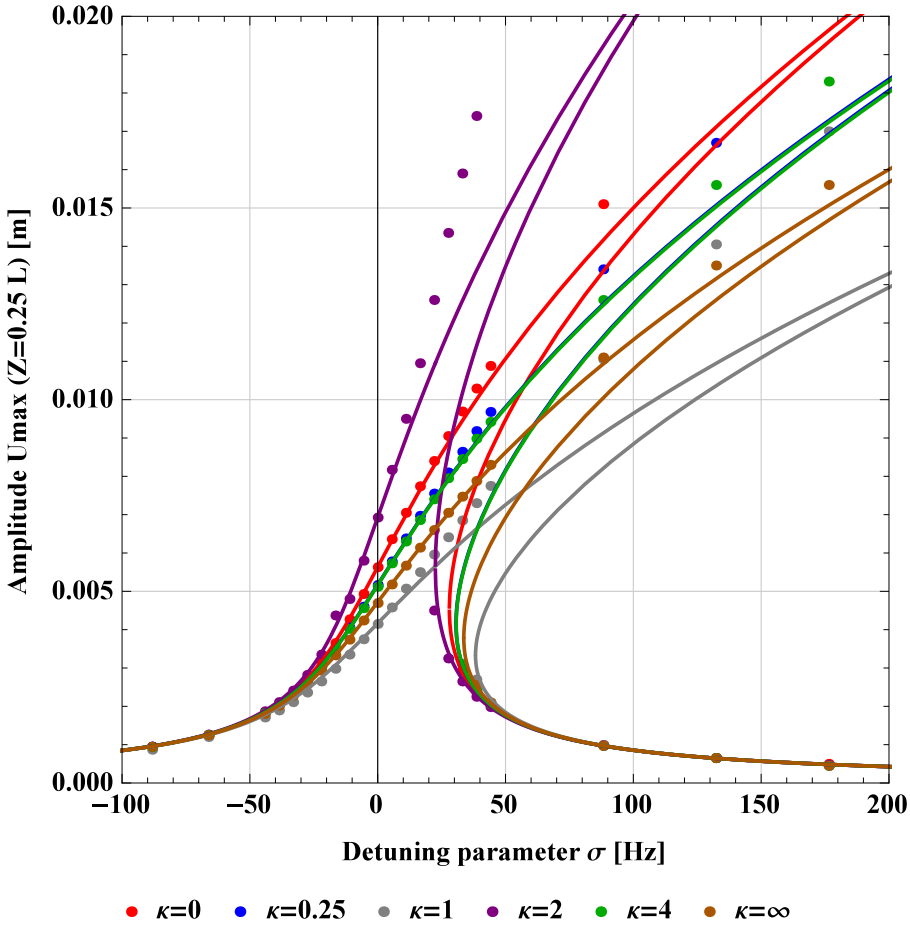

Figure 5.20: Frequency response curves: multiple time-scales method (lines) vs finite element method (dots); beam $\boldsymbol{T}$, $n = 2$, $c_z = 4$, $P_v = 59839.5$ N, $\zeta = 6$ %.

the third lengthwise $\overline{\omega}_3$-seventh flexural ω_7 modes. Besides, for continuous system infinite number of internal resonance exists. The FFT analysis shows that magnitude of amplitude $U(Z = 0.25L)$ is torn between frequency of excitation Ω and half of first natural frequency $\overline{\omega}_1$ and $W(Z = 0.25L)$ has analogous shape.

As presented in [90, 125], to study internal resonances a dedicated perturbation method have to be applied. To the best of authors' knowledge, this interaction is detected for the first time and can occur in any beam system with proper dimensions relations. It shows that the consideration of extensible piece element should be taken into account in further analysis on beams.

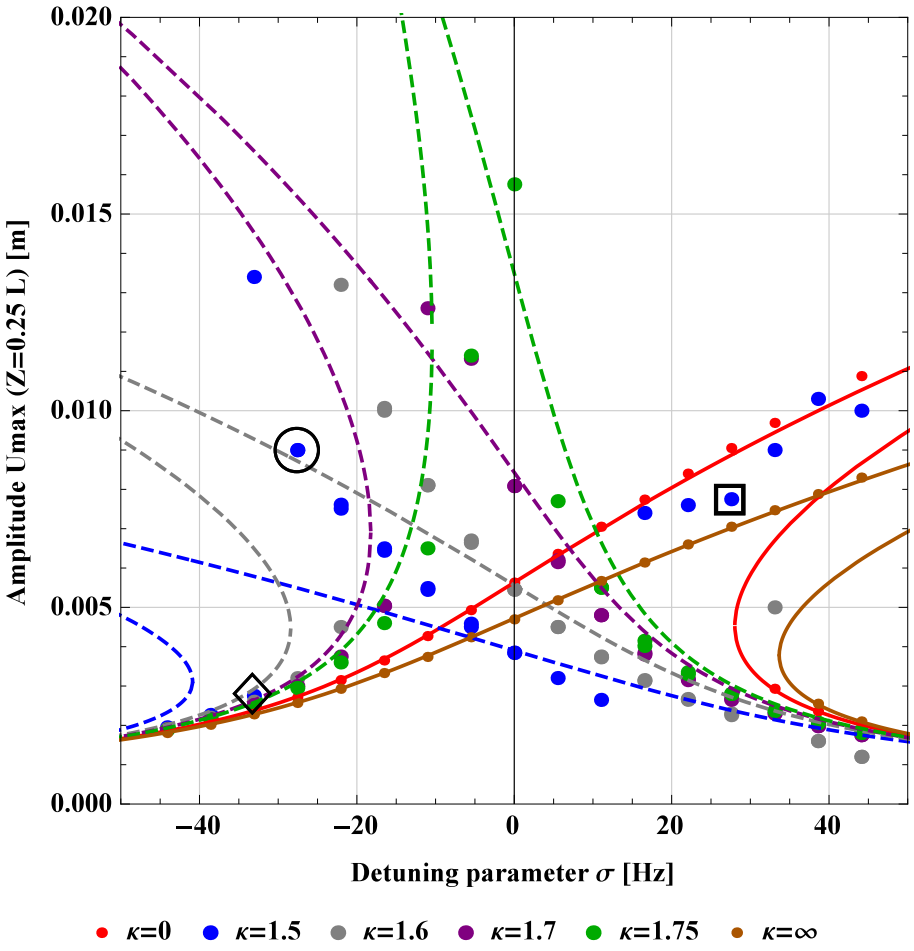

Figure 5.21: Frequency response curves: multiple time-scales method (lines) vs finite element method (dots); beam $\boldsymbol{T}$, $n = 2$, $c_z = 4$, $P_v = 59839.5$ N, $\zeta = 6$ %.

Deeper analysis is out of scope of this thesis, but it will be continued in near future [135].

Third resonance

Analyses on the resonance of the fourth (third flexural) natural frequency shows that for stiffnesses of the boundary spring the structure has only hardening behaviour, which agrees with the results of Fig. 5.23. Numerical frequency response curves display hysteresis for $\kappa_1 > 1$ and do not have an additional mode interactions. Comparison of two methods shows excellent agreement, and all

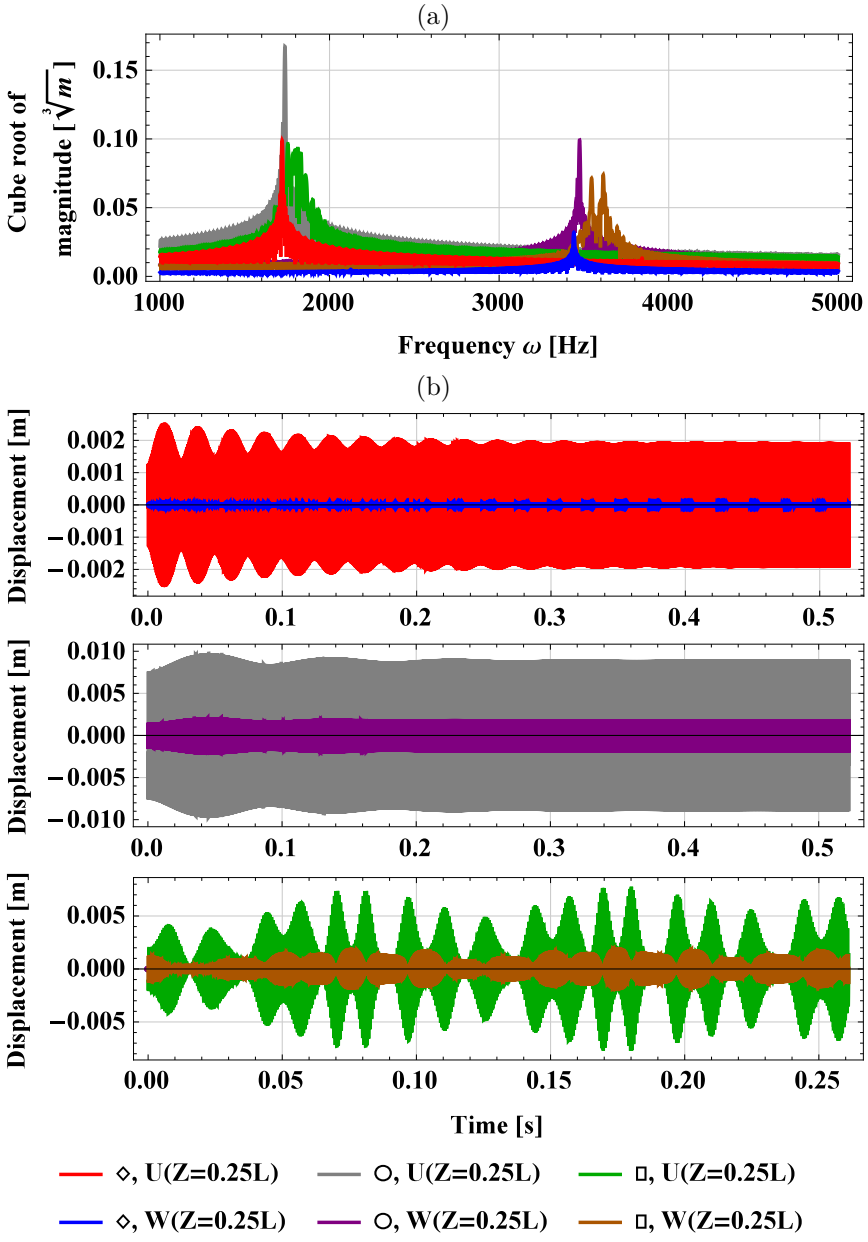

Figure 5.22: Fast Fourier transform curves (a) of the last 2^{12} recorded displacement points. Subsequent transient time histories in axial and longitudinal directions (b); they represent marked points by diamond, circle and rectangle in Figure 5.21.

dots (corresponding to numerical simulations) cover corresponding analytical lines. As expected, amplitudes of vibrations are smaller than those of primary and secondary forced-damped resonances.

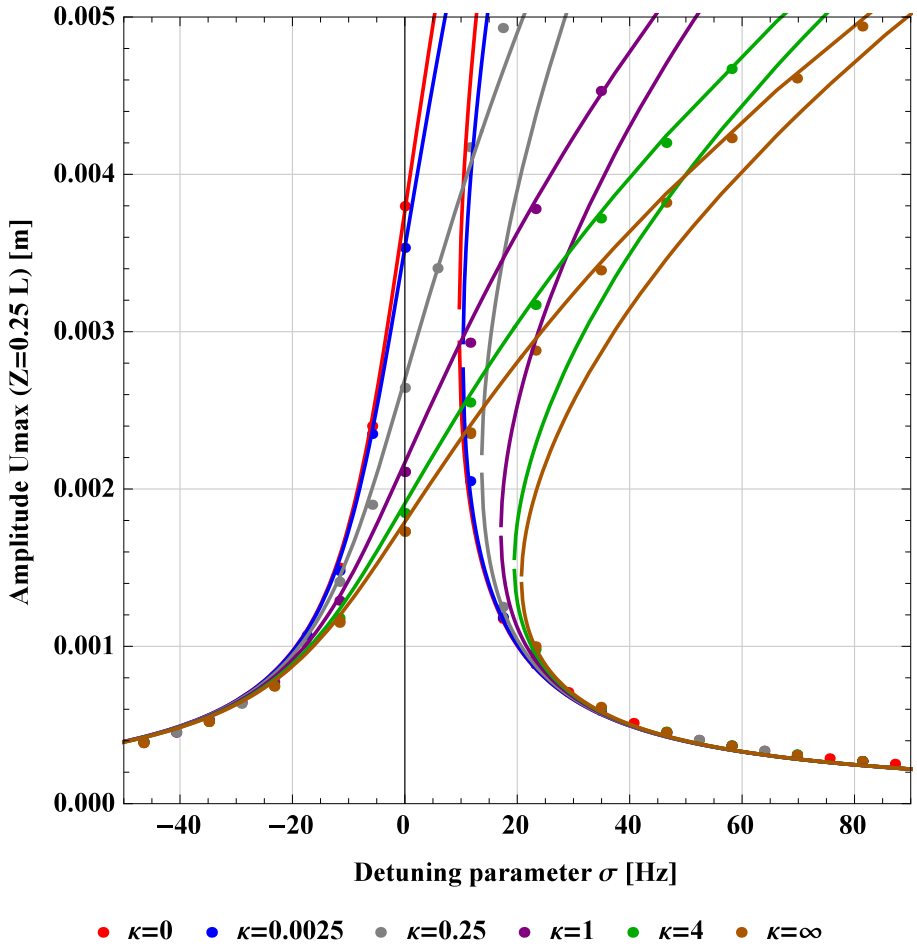

Figure 5.23: Frequency response curves: multiple time-scales method (lines) vs finite element method (dots); beam $\boldsymbol{T}$, $n = 3$, $c_z = 4$, $P_v = 59839.5$ N, $\zeta = 6$ %.

At this point we finish the comparison between finite element method and multiple time-scales method results. In next Section 5.3 we will examine kinematically excited beam $\boldsymbol{S}$ with an additional tip mass and rotatory inertia of hinges. Those terms change boundary conditions of the system, and therefore procedure of analytical approach should be reconsidered, starting from the linear analysis through a new solvability conditions in the first and second order

of solution. This is left for further developments.

5.3 Experimental verification

We analyse six cases of boundary conditions and four amplitudes of excitation separately. The modulus of elasticity E in the numerical simulations to the experimental natural frequency is fitted [136,137], then linear viscous damping coefficient is adjusted to minimize the differences between the numerical and the experimental frequency response curves. Figure 5.24 shows the natural frequency of the beam as a function of Young modulus for the first and second bending modes. An example of damping coefficient influence on the amplitudes of oscillations is displayed in Fig. 5.25.

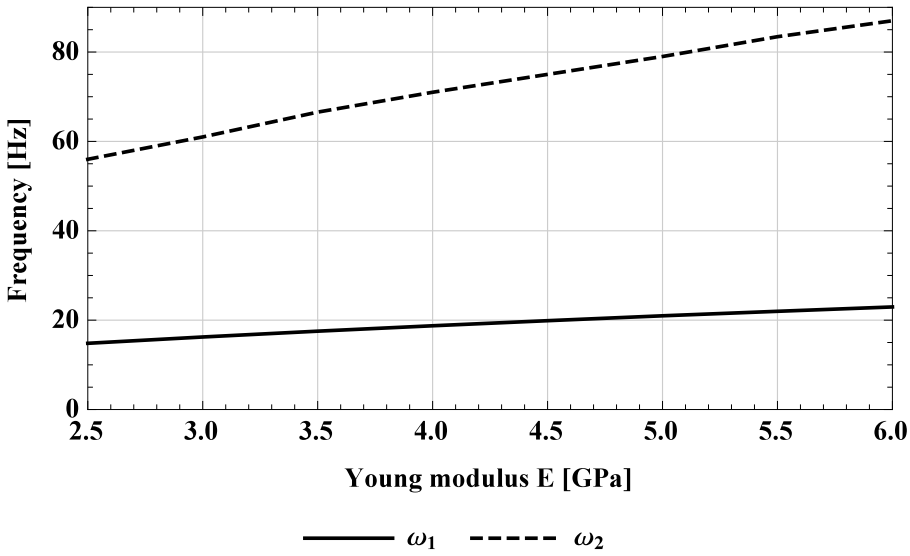

Figure 5.24: Numerical first ω_1 and second ω_2 natural frequencies of the hinged-simply supported beam as a function of the Young modulus.

The damping coefficient ζ is one of the most important governing parameters for the resonant interval, because it influences very much the maximum amplitude, whereas far from resonance ($17 > \Omega$ and $25 < \Omega$) damping coefficient has less importance. In fitting procedure other parameters of the systems $\boldsymbol{S}_0$-$\boldsymbol{S}_5$ like dimensions, density and Poisson's ratio remain unchanged.

Set of six plots which contain experimental frequency response curves are consecutively presented in Figures 5.26, 5.27, 5.28, 5.29, 5.30, 5.32. They are ordered from the hinged simply supported with no spring, through increasing stiffness k_s up to the highest stiffness $\boldsymbol{S}_5$ of beam-spring system and tests were

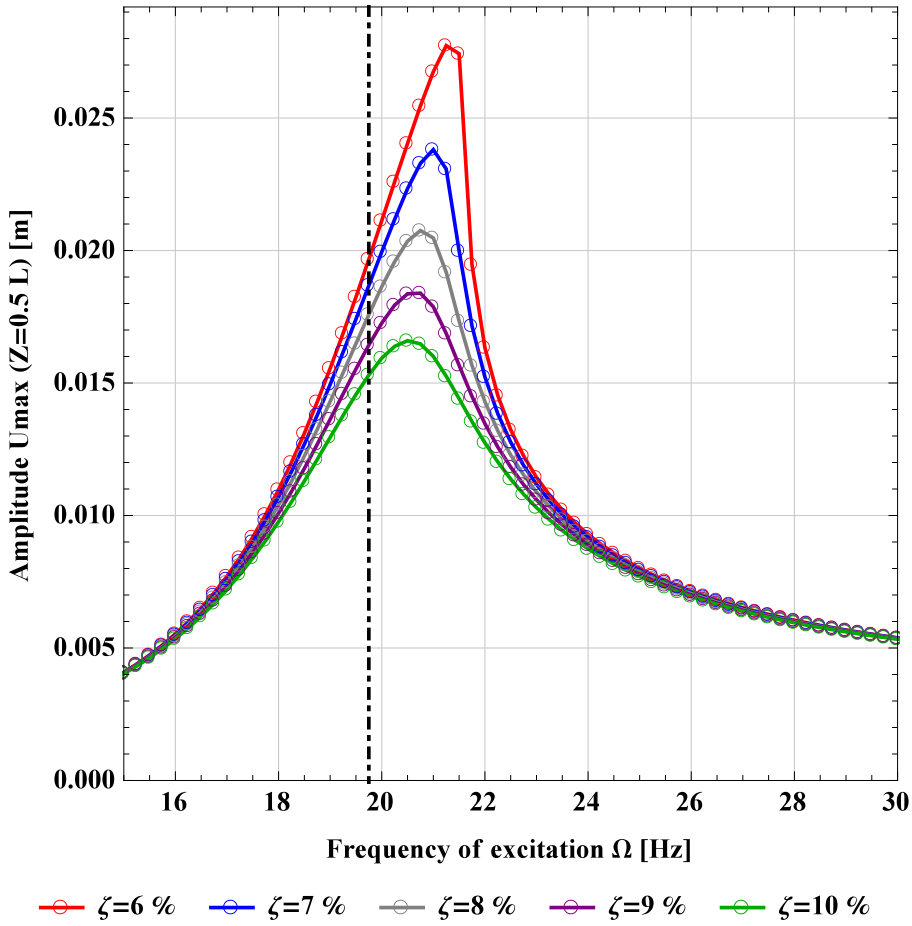

Figure 5.25: Frequency response curves for damping parameters test. Numerical results for the beam configuration $\boldsymbol{S}_{0.8}$, $\zeta = 2.5$ mm, the first natural frequency $\omega_1 = 19.75$ Hz is plotted as dot-dashed vertical line.

done for each beam starting from the highest amplitude of excitation. Moreover, the frequency sweep has been set at first backward and then forward. In the following tests amplitudes of kinematic excitation ξ were consequently reduced (from 2.5 mm to 1.0 mm). The cases $\boldsymbol{S}_0$, $\boldsymbol{S}_{0.8}$ and $\boldsymbol{S}_{4.2}$ are compared with finite element results. The comparative analysis provides the following properties: (i) the Young modulus changes (natural frequencies shift) during the experiments; and (ii) the damping coefficient is amplitude dependent. The variability of both parameters are reported in plot legends. The changes are small but nevertheless very important to reflect so well the results obtained

on the prototype. There may be many reasons of the natural frequency and damping coefficient change. One of them is increasing temperature during long-lasting experimental tests. The power generator is cooled down by air flow and the hot fluid is blown off into the laboratory room. In a daily interval the temperature increases about 8 degrees of Celsius and the Plexiglas is susceptible to temperature changes, unfortunately the temperature was not continuously registered. The second reason can be a slight pulling in/out of the beam from the hinge and shaft, together with improving the quality of sliding surfaces during tests. It generates a very complex problem, wherein too little information was considered during experiment and provides the basis for further research on this topic.

As for the Timoshenko beam $\boldsymbol{T}_0$, the specimen $\boldsymbol{S}_0$ has soft softening nature. Analysis performed in [74] shows that the tip mass softens the characteristic in the axially unrestrained configuration and almost does not affect commensurate with higher stiffnesses. Curves $E_r(\Omega_{\pm}, \xi = 1.5)$ are shifted for about ± 0.25 Hz and responses $E_r(\Omega_{\pm}, \xi = 2.5$ mm) in peak of maximum amplitudes slightly differ (see Fig. 5.26). Numerical results fully cover the experiment, the damping coefficient ζ grows together with ξ as well as the calculated natural frequency ω_1 decreases over the testing time. These characteristics can be compared (indirectly) with tests performed on a simply supported bronze beam about dimensions $0.8 \times 10 \times 450$ mm in Figure 9 of [63], where the frequency response curve is also bent toward left and for higher amplitudes of the oscillations (about 15% of the beams' length) than in our study, a jump between stable paths occur. The significantly greater tip mas $m_t = 0.25$ kg (tip to beam mass ratio 7.89) may affect the stronger softening effect response as studied in [74]. Additional compliance of both experiments is a small dispersion of vibration amplitudes for sweeping forward and backward (thermal effect). Moreover, it can be deduced from the perfect mach of both methods (experiment vs analytic) only very close to the resonant frequency that a distinction of relative (experiment) and absolute (analytic) amplitudes in their analysis was ignored, see the difference Fig. 4.12 and Eq. 4.4.

The setup $\boldsymbol{S}_{0.8}$ (Fig. 5.27) contains the weakest spring, this small change in boundary conditions turns the system response into soft hardening. Shape of experimental responses is smoother than in previous case, and again damping coefficient grows together with ζ. However, the natural frequency is constant, except at $\xi = 1.5$ mm. We attribute this minor difference to small difference of temperature during the various tests.

Despite spring stiffness increment the response of the structure in Fig. 5.28 seems to be almost linear. It is in contrast to the analytical and numerical results, where for the primary resonance the hardening increases monotonically with spring stiffness. This change could be due to the temperature variation

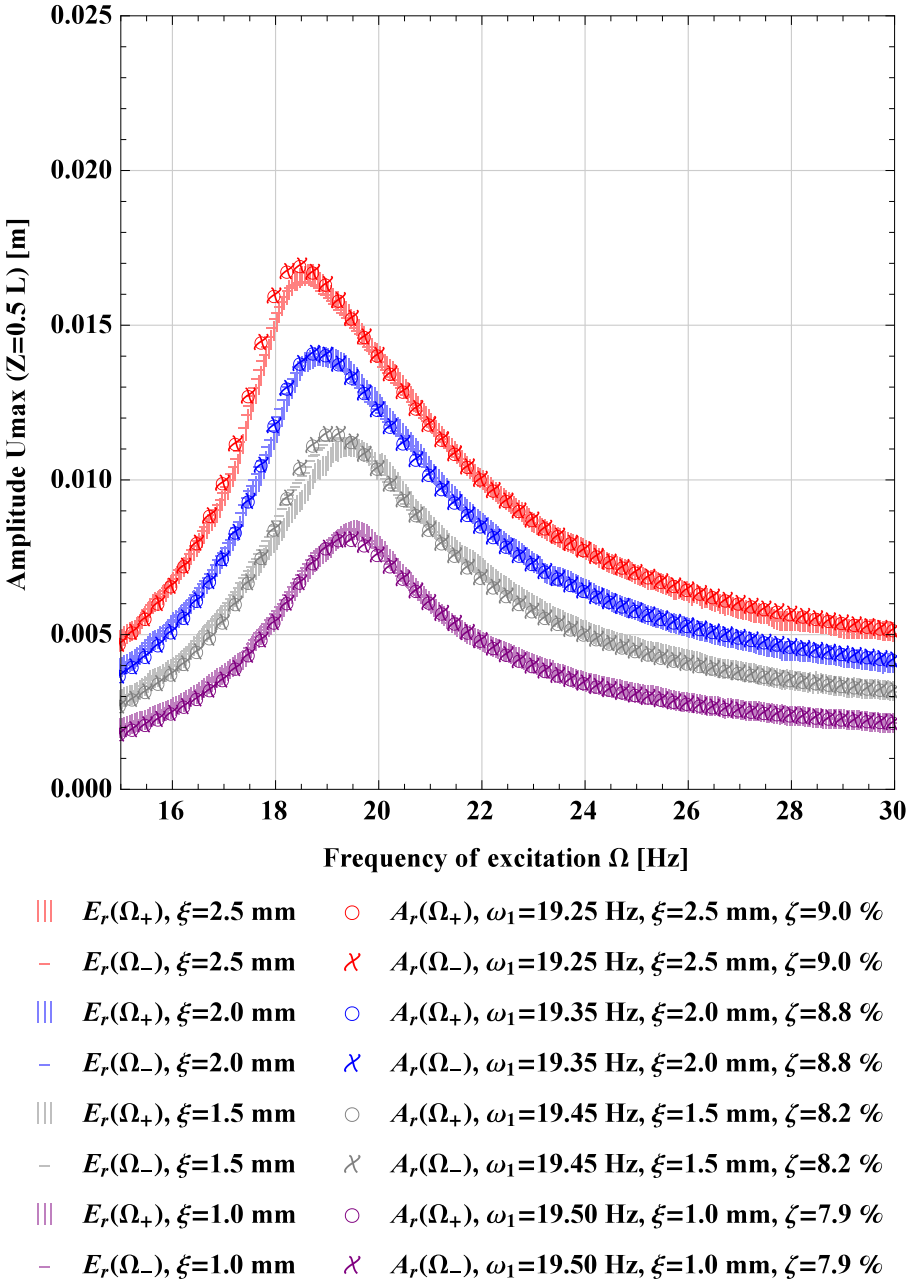

Figure 5.26: Frequency response curves: experiment vs numerical results; $\boldsymbol{S}_0$.

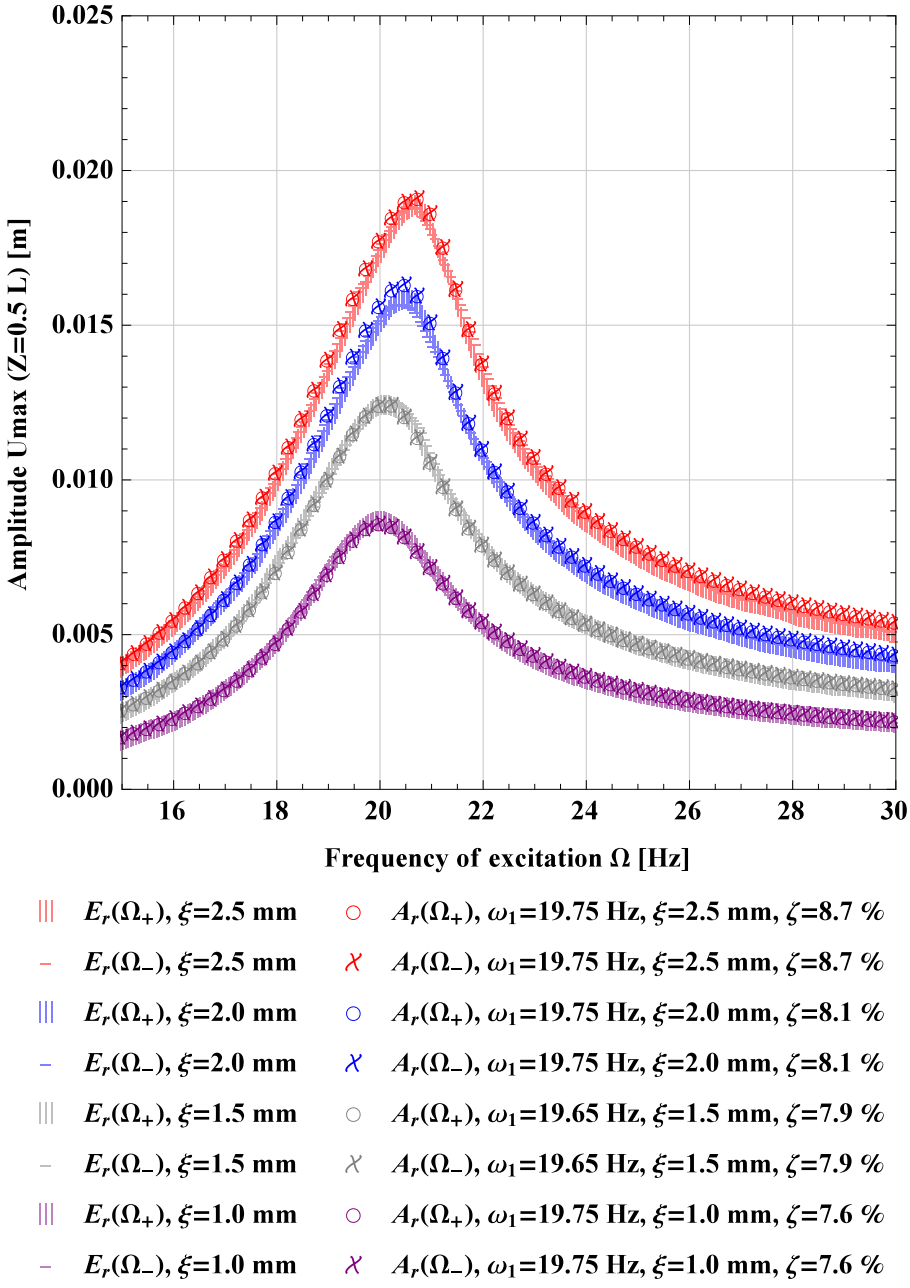

Figure 5.27: Frequency response curves: experiment vs numerical results; $\boldsymbol{S}_{0.8}$.

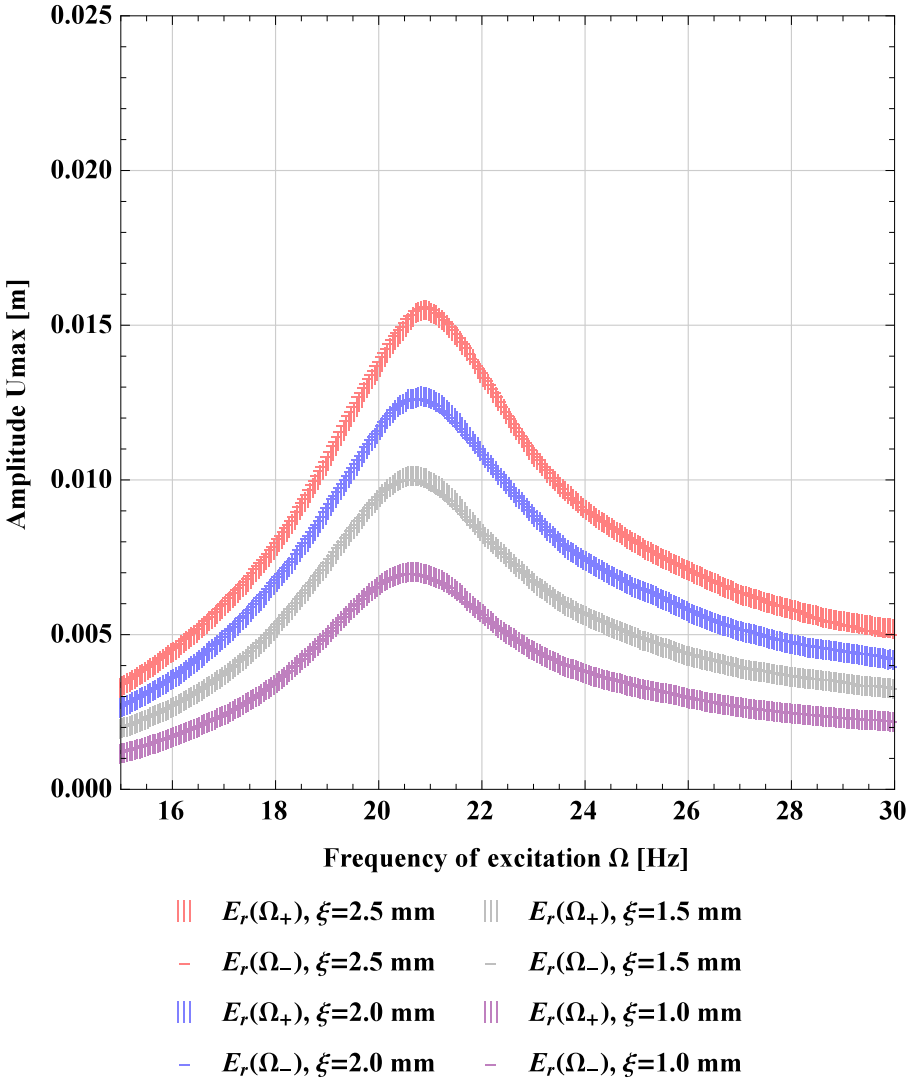

Figure 5.28: Experimental frequency response curves; $\boldsymbol{S}_1$.

(Young modulus), assembly error or another unexpected dynamical effect.

In fact, the stiffness of the springs system has been tested in quasi-static conditions, but the motion of slip table acts on the beam and working elements (sliding support). The spring stiffnesses for $\boldsymbol{S}_{0.8}$ and $\boldsymbol{S}_1$ are very close to each other. Note that, in this particular case the longest springs are used (see Fig. 4.2, case $100\times32.5\times2.5$ mm), and it may happen that they have interacted with the transverse movement, which could decrease dynamical stiffness. The

estimated natural frequency $\omega_1 = 20.75$ Hz is also the highest from the tested cases.

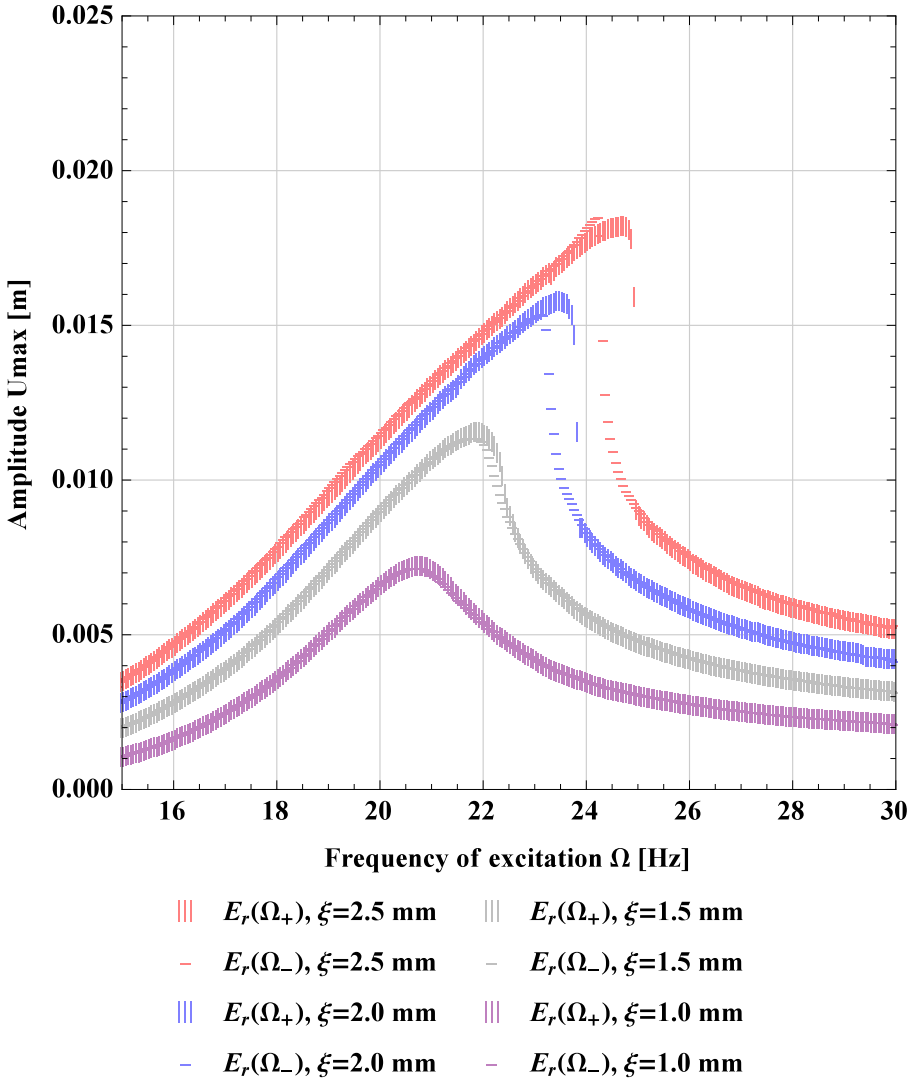

Figure 5.29: Experimental frequency response curves; $\boldsymbol{S}_3$.

Further increment of the axial spring stiffness bends characteristics toward right (Fig. 5.29). In construction of $\boldsymbol{S}_3$ jumps between upper and lower stable paths occur for $\xi = 2.0$ mm and $\xi = 2.5$ mm, and the jumping intervals are 23.4-23.8 Hz and 24.3-24.9 Hz, respectively. The local hump arise on the curves just after one of jumps for sweep backward, $\xi = 2.5$.

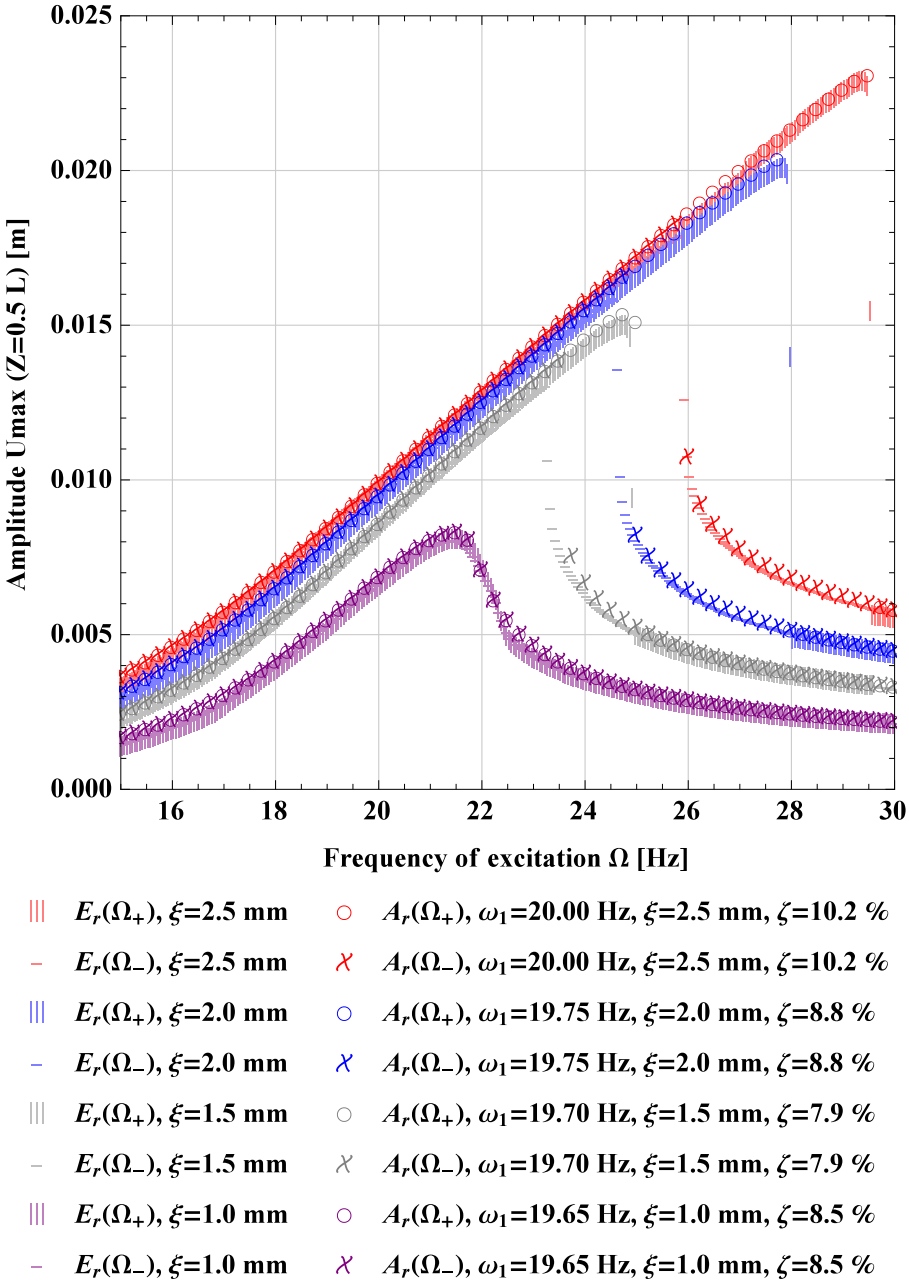

Figure 5.30: Frequency response curves: experiment vs numerical results; $\boldsymbol{S}_{4.2}$.

The most successful experimental configuration is $\boldsymbol{S}_{4.2}$ (Fig. 5.30). Amplitude of oscillations for the biggest excitation force is 24 mm, it is 5.6% of the beam length and 505% of the beams thickness. The hysteresis of the two solutions appears for excitation amplitudes $\xi = 1.5$ mm, $\xi = 2.0$ mm and $\xi = 2.5$ mm and their frequency intervals are accordingly: 23.3-24.9 Hz, 24.8-29.9 Hz and 24.9-29.5 Hz. The frequency interval for the last curve is 0.23 ω_1, and the test has been repeated few times to check the results. Proper parameters fit (ω_1, ξ) enables to match very well the hysteresis and the corresponding solution transitions. On the curve $E_r(\Omega_+), \zeta = 2.5$ mm a slight ridge has grown between 27 Hz and 29.5 Hz. This region has been studied with the numerical simulations by recording two additional points on the beam. Figure 5.31 shows that $U(Z = 0.25L)$ and $U(Z = 0.75L)$ loose symmetry, it means that the first and the second bending modes interact. According to Fig. 5.24 the

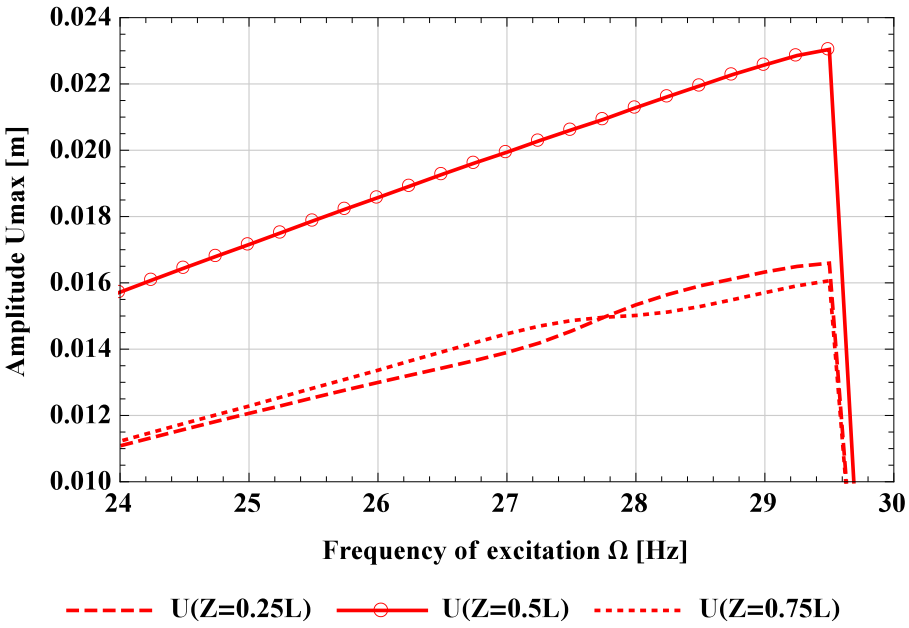

Figure 5.31: Frequency response curves obtained in numerical simulations for three points along the beam of configuration $\boldsymbol{S}_{4.2}$, $\omega_1 = 20$ Hz.

frequencies $\omega_1(E = 4.5$ GPa$) = 20$ Hz and $\omega_2(E = 4.5$ GPa$) = 75$ Hz are in ratio 3.75, and it is far from internal resonance (in linear regime). However, considering the frequency of excitation $\Omega \approx 27$ Hz, the relation Ω/ω_2 becomes 2.78. Assuming that the second bending mode has hardening nature (frequency response increases together with the amplitude), it intersects frequencies relation which are precisely 3. The symmetrical excitation of the beam very poorly

stimulate the second bending mode, which slightly modifies nonlinear modal shape of response. The response of midpoint (modal node for $n = 2$) remains undisturbed.

In order to trig simultaneously the first and the second bending modes the symmetry in the system must be broken, for example as it has been done in Section 5.2.2

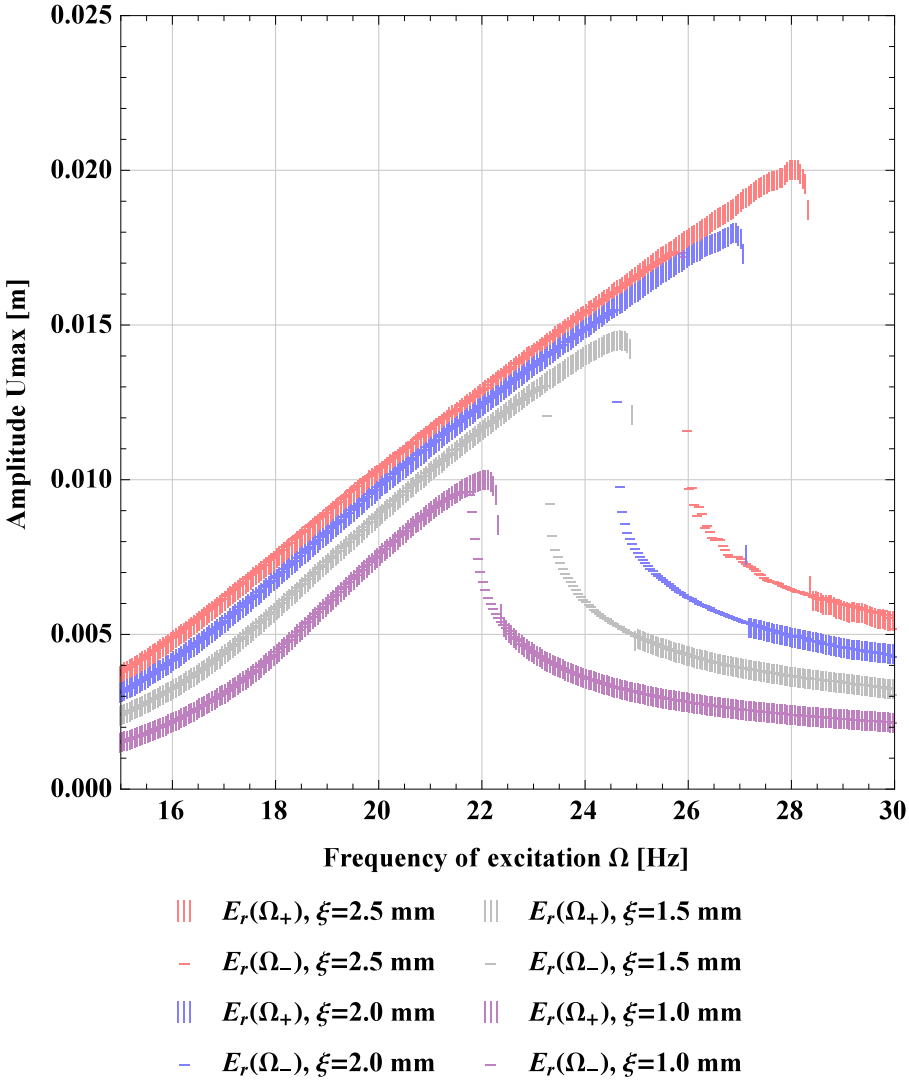

Figure 5.32: Experimental frequency response curves; $\boldsymbol{S}_5$.

The strongest hardening behaviour of the beam-spring system is found for $\boldsymbol{S}_5$

(Fig. 5.32), although the structural dissipation limits length of followed branches. Similarly to the previous case soft bulges appear for 27 Hz $< \Omega <$ 28.5 Hz, $\xi = 2.5$ of upper as well as lower branches. Based on performed numerical computations, more extensive analysis of two modes interaction require increasing the amplitude of excitation or change method of excitation, but due to the restrictions imposed by shaker limitations, the experimental tests have been completed at this stage.

Collectively analyzing the results, the summary Tab. 5.3 is built for studied cases, where the peaks of amplitudes are selected as well as their corresponding jump frequencies. Changes in critical frequency with increasing amplitude show the hardening/softening dichotomy. Underlined cells mark the bifurcation occurrence.

Table 5.3: Maximum relative amplitudes of the kinematically excited beam-spring system.

Amplitude of excitation	$E_{rmax}(\Omega_+)$ $[mm(Hz)]$		
ξ $[mm]$	$\boldsymbol{S}_0$	$\boldsymbol{S}_{0.8}$	$\boldsymbol{S}_1$
2.5	17.0(18.50)	19.0(20.75)	15.5(20.90)
2.0	14.0(18.75)	16.5(20.50)	13.0(20.70)
1.5	11.5(19.00)	12.5(20.25)	10.0(20.60)
1.0	8.0(19.50)	8.5(20.00)	7.0(20.50)
ξ $[mm]$	$\boldsymbol{S}_3$	$\boldsymbol{S}_{4.2}$	$\boldsymbol{S}_5$
2.5	19.0(25.00)	23.5(29.50)	20.0(28.00)
2.0	16.5(23.5)	20.0(27.50)	18.0(25.50)
1.5	12.0(21.75)	15.0(25.00)	15.5(25.00)
1.0	7.5(20.75)	8.0(21.5)	10.0(22.10)

The direct frequency response curve fitting of the laboratory results shows the dissipation and natural frequency trends for the kinematically excited beam; they are reported in Fig. 5.33. Damping coefficient linearly grows with increasing amplitude of excitation, in contrary to the preliminary results for $\xi = 0$ presented in Tab. 4.2. As displayed in Fig. 4.12, the absolute displacement (velocity) of the system is bigger than relative displacement (velocity). Natural frequencies were examined in three cases: softening, soft hardening and harden-

ing; and they increase, remain almost constant and decrease, respectively. Note that experiment from the biggest to the smallest amplitudes of excitation have been performed. There is a high probability of slight changes in the clamps, which affect the length of the beam and consequently the natural frequency of the structure. However, there may be more of these disadvantages, for example a change in temperature. Deeper discussion on results of experimental tests has been submited to [78].

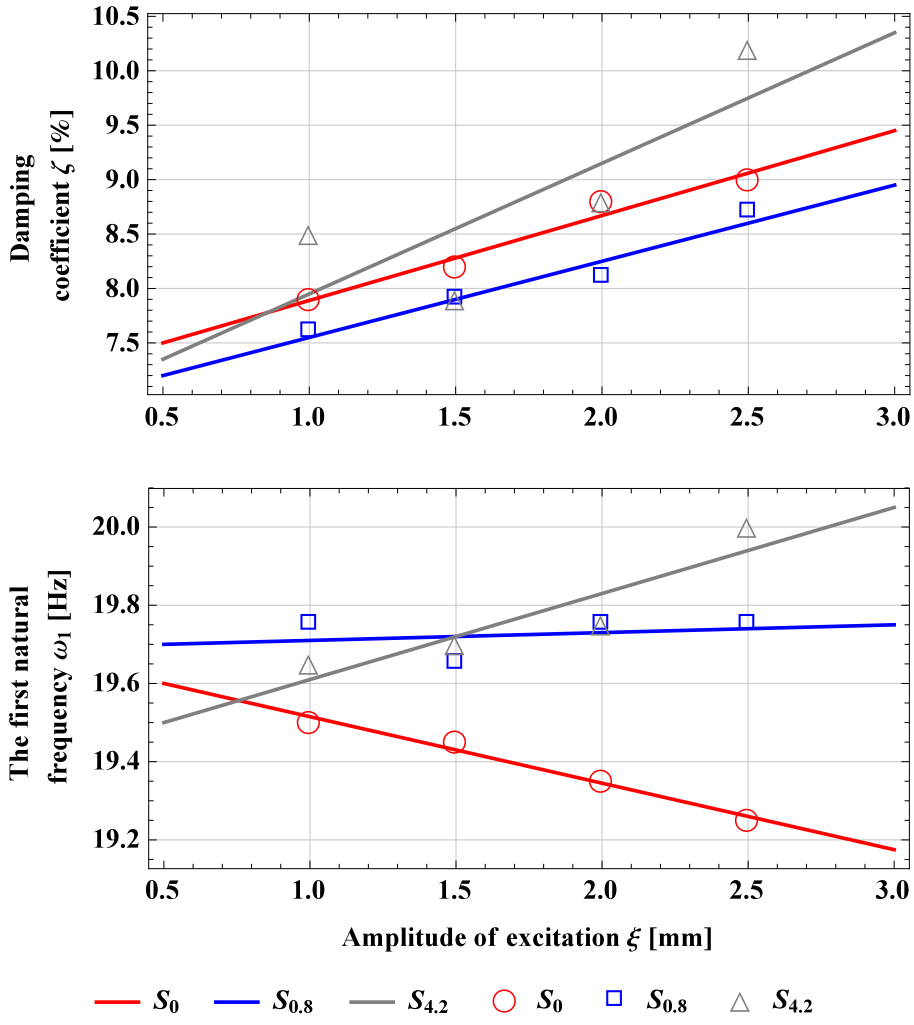

Figure 5.33: Summary of linear trends of damping coefficient (top) and natural frequencies (bottom).

Chapter 6

Conclusions

Planar simply supported beams with an axial spring in one end as an adaptable boundary condition to control nonlinear dynamic of the structure are considered in the thesis. In Chapter 2 three governing equations of motion were derived for the structure considering axial, bending and shearing deformations of the beam element; longitudinal, transverse and rotatory inertia; linear elasticity of the material and the set of six boundary conditions having regard to pivotal elastic element. Afterwards, the problem is expanded in Taylor series and the method of multiple time-scales is introduced, performed linear analysis and determined the frequency response equation which describes free as well as forced-damped nonlinear oscillations. The cubic nonlinearities are solved up to the second order of approximation, what successfully captures large amplitudes of vibrations for primary and higher order resonances. The free dynamics of the system for the first seven bending modes was checked in terms of hardening/softening dichotomy, wherein the key parameter is the ratio of spring to beam tensile stiffnesses. Analytical investigations end with the fully constructed frequency response curves of forced-damped structure for the first three flexural modes.

In Chapter 3, as a support for cumbersome analytical calculations commercial finite element software Abaqus_CAE® is used. At first the beam-spring structure is modeled and then to confirm analytical calculations, the linear modal analysis is performed. Three different methods were presented for testing nonlinear dynamics of the system. To draw backbone curves of the numerical model free oscillations of the system with an initial deformation and a slight damping were used; approximately transforming a time history into a frequency-amplitude arrangement the hardening/softening behaviour were captured very well. A two transient in time types of simulation were used to investigate nonlinear forced-damped vibrations. To build the full frequency response curve an excitation was, gradually changed through increasing and decreasing frequency. Apart from the transitional state amplitudes in frequency domain were recorded and for stronger nonlinearities or large amplitudes the solution hysteresis was found. Additional solutions, unexplored by path-following

method, in specific frequency intervals were studied by guessing an initial nonlinear modal shape. Parallel finite element computations complemented each other.

After sophisticated studies on theoretical problem a physical prototype was designed, manufactured and tested in Chapter 4. Presented setup is mounted on slip table (vibration exciter) with changeable boundary conditions in the axial direction. In the first stage, properties of the specimen and suspension of the sliding support were tested. Next attention was paid to free oscillations and corresponding structural damping which indeed is amplitude dependent. Finally full experimental frequency response curves of kinematically excited structure were drawn. Selected cases were compared with the numerical results with identical hardening/softening behaviour, and very good agreement was obtained.

Results of analytical calculations, numerical simulations and experimental investigations are presented in Chapter 5. First, the natural frequencies of beams are compared analytically and numerically for the first ten modes of the structure with a good agreement, then influence of an axial spring on axial beams displacement in the linear regime is highlighted. Successively nonlinear free and forced-damped vibrations with the use of the nonlinear correction coefficient, backbone curves and frequency response curves are analyzed theoretically up to the seventh bending mode. In the numerical simulations the superharmonic flexural-flexural and axial-flexural resonances are detected. In particular the latter interaction is novel in the knowledge of beam's dynamics. The experimental results are particularly useful in the investigation. They thoroughly confirm a smooth change from softening to hardening by increasing the stiffness of the spring, which was studied in [67–72, 74–78] as well as is the one of the main objectives of the thesis.

6.1 The advantages of presented studies

Analytical vs numerical and numerical vs experimental results are simultaneously compared between each other, and all three methods provide reliable results. In both studied cases of simply supported beams $\boldsymbol{T}$ (non-slender) and $\boldsymbol{S}$ (slender) have softening behaviour for the first bending mode. The elastic element, which is axially fixed to the beams tip, interferes only with longitudinal mode of the linear regime without changing lateral linear frequency and associated mode shape. Higher amplitudes of oscillation exit linear nature of the structure and throughout geometrical nonlinearities and inertia terms link two orthogonal directions of motion. This coupling was one of main motivations of this work. Interaction of two modes (axial and transversal) becomes more and more complex by analyzing different boundary conditions (κ) and higher order

resonances (n).

All three methods for the primary resonance show compliance in the smooth change from softening to hardening by changing the boundary conditions in the longitudinal direction. The only suspected case is the experiment on $\boldsymbol{S}_1$, where additional unclear external interaction appeared. When frequency of excitation further move away from the first natural frequency, interactions between the first and second flexural-flexural modes are stimulated in numerical simulations and experimental tests. Appropriately selected spring stiffness k_s and asymmetrical excitation of the system enabled three stable solutions paths for a given frequency.

Investigating, with good success, higher order resonances a new phenomenon of the internal transversal-axial resonance 2:1 was detected, which breaks monotonic changes in nonlinear correction coefficient c_b by singularities. In this critical case the structure is characterized by high vibration amplitudes in both directions: longitudinal and transverse. Furthermore, occurrence of energy transfer between those two modes is very interesting from practical point of view as a paramount structural element for cutting-edge applications, such as nonlinear vibration absorbers and nonlinear vibration energy harvesters among others.

Finite element analysis shows additional phenomena, which are not included in the analytical derivation. But, analytical considerations consist of cumbersome calculations; require solvability conditions and integration of very complex functions. After all the effort of deriving frequency response curves, it is easy to examine the system for individual parameters e.g. κ, A/L, γ with little expenditure of time. In numerical simulations it is easy to visualize the results, but the computational time is very long for all of the presented methods for nonlinear dynamics analysis, in particular the path-following method.

The setup presented in this work can be successfully upgraded for further investigations on boundary conditions-frequency response curves of the structure. This requires an extension of the analytical model, in particular environmental and boundary conditions.

6.2 Further developments

There are still a lot of challenges which need to be assessed in the future. They are ordered from the most attractive:

- numerical, analytical and experimental study on the internal axial-transversal resonance two to one;
- derivation analytical solutions of flexular-flexular internal resonances two to one and three to one like in [105];

- investigation on different configurations, including rotatory and translatory inertia in boundary conditions as well as nonhomogeneous beam properties along the beam length;
- development of multifrequency excitation;
- extension a beam model to shearable, non-planar with the bending-bending-twisting effects.

Bibliography

[1] S. Timoshenko, History of strength of materials: With a brief account of the history of theory of elasticity and theory of structures, Dover Publications, New York, 1999.

[2] A. E. H. Love, A treatise on the mathematical theory of elasticity, 4th Edition, Cambridge University Press, Cambridge, 1927 (3rd ed 2013).

[3] L. Meirovitch, Analytical methods in vibrations, Macmillan series in applied mechanics, Macmillan, New York, N.Y., 1967.

[4] W. T. Thomson, Theory of vibration with applications, Prentice-Hall, Englewood Cliffs, N.J., 1972.

[5] J. N. Reddy, An introduction to nonlinear finite element analysis, reprint Edition, Oxford Univ. Press, Oxford, 2004.

[6] A. H. Nayfeh, P. F. Pai, Linear and Nonlinear Structural Mechanics, Wiley, 2004. doi:10.1002/9783527617562.

[7] E. Carrera, G. Giunta, M. Petrolo, Beam Structures, John Wiley & Sons, Ltd, Chichester, UK, 2011. doi:10.1002/9781119978565.

[8] S. S. Rao, Mechanical vibrations, 5th Edition, Prentice Hall, Upper Saddle River, N.J., 2011.

[9] John William Strutt, Baron Rayleigh, Theory of sound, 1877.

[10] R. W. Traill-Nash, A. R. Collar, The effects of shear flexibility and rotatory inertia on the bending vibrations of beams, The Quarterly Journal of Mechanics and Applied Mathematics 6 (2) (1953) 186–222. doi:10.1093/qjmam/6.2.186.

[11] R. M. Davies, Lv. the frequency of transverse vibration of a loaded fixed-free bar .—iii. the effect of the rotatory inertia of the bar, The London, Edinburgh, and Dublin Philosophical Magazine and Journal of Science 23 (155) (1937) 563–573. doi:10.1080/14786443708561828.

[12] S. P. Timoshenko, On the correction for shear of the differential equation for transverse vibrations of prismatic bars, The London, Edinburgh, and

Dublin Philosophical Magazine and Journal of Science 41 (245) (1921) 744–746. doi:10.1080/14786442108636264.

[13] S. P. Timoshenko, On the transverse vibrations of bars of uniform cross-section, The London, Edinburgh, and Dublin Philosophical Magazine and Journal of Science 43 (253) (1922) 125–131. doi:10.1080/14786442208633855.

[14] E. T. Kruszewski, Effect of transverse shear and rotary inertia on the natural frequency of a uniform beam, National Advisory Committe (1949) 1–16.

[15] G. Herrmann, Forced motions of Timoshenko beams.
URL https://apps.dtic.mil/dtic/tr/fulltext/u2/013062.pdf

[16] R. D. Mindlin, L. E. Goodman, Beam vibrations with time-dependent boundary conditions, Journal of Applied Mechanics (17) (1950) 377–380.

[17] R. D. Mindlln, G. Herrmann, A one-dimensional theory of compressional waves in an elastic rod, Proceedings of the first US National Congress of Applied Mechanics (1951) 187–191.

[18] C. L. Dolph, On the Timoshenko theory of transverse beam vibrations, Quarterly of Applied Mathematics 12 (2) (1954) 175–187.

[19] T. C. Huang, The effect of rotatory inertia and of shear deformation on the frequency and normal mode equations of uniform beams with simple end conditions, Journal of Applied Mechanics 28 (4) (1961) 579–584. doi:10.1115/1.3641787.

[20] G. R. Cowper, The shear coefficient in Timoshenko's beam theory, Journal of Applied Mechanics 33 (2) (1966) 335. doi:10.1115/1.3625046.

[21] B. Dawson, Rotary inertia and shear in beam vibration treated by the Ritz method, The Aeronautical Journal 72 (688) (1968) 341–344. doi:10.1017/S0001924000084165.

[22] B. Dawson, W. Carnegie, Modal curves of pre-twisted beams of rectangular cross-section, Journal of Mechanical Engineering Science 11 (1) (1969) 1–13. doi:10.1243/JMES_JOUR_1969_011_003_02.

[23] J. B. Carr, The effect of shear flexibility and rotatory inertia on the natural frequencies of uniform beams, Aeronautical Quarterly 21 (1) (1970) 79–90. doi:10.1017/S0001925900005242.

[24] S. Atluri, Nonlinear vibrations of a hinged beam including nonlinear inertia effects, Journal of Applied Mechanics 40 (1) (1973) 121. doi:10.1115/1.3422909.

[25] A. V. Srinivasan, Non-linear vibrations of beams and plates, International Journal of Non-Linear Mechanics 1 (3) (1966) 179–191. doi:10.1016/0020-7462(66)90003-5.

[26] S. Woinowsky-Krieger, The effect of axial force on the vibration of hinged bars, Journal of Applied Mechanics (Vol. 17) (1950) 35–36.

[27] D. A. Evensen, Nonlinear vibrations of beams with various boundary conditions, AIAA Journal 6 (2) (1968) 370–372. doi:10.2514/3.4506.

[28] J. G. Eisley, Nonlinear vibration of beams and rectangular plates, Zeitschrift für angewandte Mathematik und Physik ZAMP 15 (2) (1964) 167–175. doi:10.1007/BF01602658.

[29] C. Mei, Nonlinear vibration of beams by matrix displacement method, AIAA Journal 10 (3) (1972) 355–357. doi:10.2514/3.6595.

[30] C. Mei, Finite element displacement method for large amplitude free flexural vibrations of beams and plates, Computers & Structures 3 (1) (1973) 163–174. doi:10.1016/0045-7949(73)90081-3.

[31] G. Prathap, T. K. Varadan, The large amplitude vibration of hinged beams, Computers & Structures 9 (2) (1978) 219–222. doi:10.1016/0045-7949(78)90141-4.

[32] M. R. Crespo Da Silva, C. C. Glynn, Nonlinear flexural-flexural-torsional dynamics of inextensional beams. i. equations of motion, Journal of Structural Mechanics 6 (4) (1978) 437–448. doi:10.1080/03601217808907348.

[33] M. R. Crespo Da Silva, C. C. Glynn, Nonlinear flexural-flexural-torsional dynamics of inextensional beams. ii. forced motions, Journal of Structural Mechanics 6 (4) (1978) 449–461. doi:10.1080/03601217808907349.

[34] J. R. Hutchinson, Vibrations of solid cylinders, Journal of Applied Mechanics 47 (4) (1980) 901–907. doi:10.1115/1.3153811.

[35] G. W. McMahon, Experimental study of the vibrations of solid, isotropic, elastic cylinders, The Journal of the Acoustical Society of America 36 (1) (1964) 85–92. doi:10.1121/1.1918918.

[36] J. R. Hutchinson, Transverse vibrations of beams, exact versus approximate solutions, Journal of Applied Mechanics 48 (4) (1981) 923. doi:10.1115/1.3157757.

[37] A. Luongo, G. Rega, F. Vestroni, On nonlinear dynamics of planar shear indeformable beams, Journal of Applied Mechanics 53 (3) (1986) 619. doi:10.1115/1.3171821.

[38] A. Luongo, M. Pignataro, G. Rega, F. Vestroni, Nonlinear vibrations of beams including shear deformations and rotatory inertia 28 180–191. doi:10.1007/978-3-642-83040-2_16.

[39] A. Luongo, G. Rega, F. Vestroni, Accurate nonlinear equations and a perturbational solution for the free nonplanar vibrations of inextensional beams, 2nd Int. Conf. on Recent Advances in Structural Dynamics (1984) 341–350.

[40] A. Luongo, G. Rega, F. Vestroni, : Nonlinear dynamics of planar sheear-indeformable beam, 1st. Scienza delle Costruzioni, L'Aquila (1984) 80.

[41] M. R. Crespo Da Silva, Non-linear flexural-flexural-torsional-extensional dynamics of beams—i. formulation, International Journal of Solids and Structures 24 (12) (1988) 1225–1234. doi:10.1016/0020-7683(88)90087-X.

[42] M. R. Crespo Da Silva, Non-linear flexural-flexural-torsional-extensional dynamics of beams—ii. response analysis, International Journal of Solids and Structures 24 (12) (1988) 1235–1242. doi:10.1016/0020-7683(88)90088-1.

[43] W. M. van Spengen, Capacitive RF MEMS switch dielectric charging and reliability: a critical review with recommendations, Journal of Micromechanics and Microengineering 22 (7) (2012) 074001. doi:10.1088/0960-1317/22/7/074001.

[44] M. I. Younis, E. M. Abdel-Rahman, A. Nayfeh, A reduced-order model for electrically actuated microbeam-based mems, Journal of Microelectromechanical Systems 12 (5) (2003) 672–680. doi:10.1109/JMEMS.2003.818069.

[45] F. Goldschmidtboeing, P. Woias, Characterization of different beam shapes for piezoelectric energy harvesting, Journal of Micromechanics and Microengineering 18 (10) (2008) 104013. doi:10.1088/0960-1317/18/10/104013.

[46] H. M. Ouakad, S. Ilyas, M. I. Younis, Investigating Mode Localization at Lower- and Higher-Order Modes in Mechanically Coupled MEMS Resonators, Journal of Computational and Nonlinear Dynamics 15 (3), 031001. arXiv:https://asmedigitalcollection.asme.org/computationalnonlinear/article-pdf/15/3/031001/6469214/cnd_015_03_031001.pdf, doi:10.1115/1.4045634.

[47] J. Chung, H. H. Yoo, Dynamic analysis of a rotating cantilever beam by using the finite element method, Journal of Sound and Vibration 249 (1) (2002) 147–164. doi:10.1006/jsvi.2001.3856.

[48] F. Georgiades, J. Latalski, J. Warminski, Equations of motion of rotating composite beam with a nonconstant rotation speed and an arbitrary preset angle, Meccanica 49 (8) (2014) 1833–1858. doi:10.1007/s11012-014-9926-9.

[49] J. Warmiński, L. Kloda, S. Lenci, Nonlinear vibrations of an extensible rotating beam with tip mass, Meccanica (in press) 1–39.

[50] M. Rafiee, F. Nitzsche, M. Labrosse, Dynamics, vibration and control of rotating composite beams and blades: A critical review, Thin-Walled Structures 119 (2017) 795–819. doi:10.1016/j.tws.2017.06.018.

[51] W. Fan, P. Qiao, Vibration-based damage identification methods: A review and comparative study, Structural Health Monitoring: An International Journal 10 (1) (2011) 83–111. doi:10.1177/1475921710365419.

[52] E. Manoach, J. Warminski, L. Kloda, A. Teter, Vibration based methods for damage detection in structures, MATEC Web of Conferences 83 (2016) 05007. doi:10.1051/matecconf/20168305007.

[53] E. Manoach, J. Warminski, L. Kloda, A. Teter, Numerical and experimental studies on vibration based methods for detection of damage in composite beams, Composite Structures 170 (2017) 26–39. doi:10.1016/j.compstruct.2017.03.005.

[54] K. V. Avramov, Non-linear beam oscillations excited by lateral force at combination resonance, Journal of Sound and Vibration 257 (2) (2002) 337–359. doi:10.1006/jsvi.2002.5043.

[55] W. Lacarbonara, G. Rega, Resonant non-linear normal modes. part ii: activation/orthogonality conditions for shallow structural systems, International Journal of Non-Linear Mechanics 38 (6) (2003) 873–887. doi:10.1016/S0020-7462(02)00034-3.

[56] S. A. Emam, A. H. Nayfeh, On the nonlinear dynamics of a buckled beam subjected to a primary-resonance excitation, Nonlinear Dynamics 35 (1) (2004) 1–17. doi:10.1023/B:NODY.0000017466.71383.d5.

[57] W. Lacarbonara, H. N. Arafat, A. H. Nayfeh, Non-linear interactions in imperfect beams at veering, International Journal of Non-Linear Mechanics 40 (7) (2005) 987–1003. doi:10.1016/j.ijnonlinmec.2004.10.006.

[58] M. Pakdemirli, A. H. Nayfeh, Nonlinear vibrations of a beam-spring-mass system, Journal of Vibration and Acoustics 116 (4) (1994) 433. doi:10.1115/1.2930446.

[59] W. Lacarbonara, R. Camillacci, Nonlinear normal modes of structural systems via asymptotic approach, International Journal of Solids and Structures 41 (20) (2004) 5565–5594. doi:10.1016/j.ijsolstr.2004.04.029.

[60] I. S. Son, Y. Uchiyama, W. Lacarbonara, H. Yabuno, Simply supported elastic beams under parametric excitation, Nonlinear Dynamics 53 (1-2) (2008) 129–138. doi:10.1007/s11071-007-9301-7.

[61] M. Pakdemirli, H. Boyacı, Vibrations of a stretched beam with non-ideal boundary conditions, Mathematical and Computational Applications 6 (3) (2001) 217–220. doi:10.3390/mca6030217.

[62] H. Boyaci, Vibrations of stretched damped beams under non-ideal boundary conditions, Sadhana 31 (1) (2006) 1–8. doi:10.1007/BF02703795.

[63] W. Lacarbonara, H. Yabuno, Refined models of elastic beams undergoing large in-plane motions: Theory and experiment, International Journal of Solids and Structures 43 (17) (2006) 5066–5084. doi:10.1016/j.ijsolstr.2005.07.018.

[64] A. Arena, G. Formica, W. Lacarbonara, H. Dankowicz, Nonlinear finite element-based path following of periodic solutions (DETC2011-48673) (2011) 787–793.

[65] A. Shibata, S. Ohishi, H. Yabuno, Passive method for controlling the nonlinear characteristics in a parametrically excited hinged-hinged beam by the addition of a linear spring, Journal of Sound and Vibration 350 (2015) 111–122. doi:10.1016/j.jsv.2015.03.055.

[66] N. Araumi, H. Yabuno, Cubic–quintic nonlinear parametric resonance of a simply supported beam, Nonlinear Dynamics 90 (1) (2017) 549–560. doi:10.1007/s11071-017-3680-1.

[67] S. Lenci, G. Rega, Nonlinear free vibrations of planar elastic beams: A unified treatment of geometrical and mechanical effects, Procedia IUTAM 19 (2016) 35–42. doi:10.1016/j.piutam.2016.03.007.

[68] S. Lenci, G. Rega, Axial-transversal coupling in the free nonlinear vibrations of timoshenko beams with arbitrary slenderness and axial boundary conditions, Proceedings. Mathematical, physical, and engineering sciences 472 (2190) (2016) 20160057. doi:10.1098/rspa.2016.0057.

[69] S. Lenci, F. Clementi, G. Rega, A comprehensive analysis of hardening/softening behaviour of shearable planar beams with whatever axial boundary constraint, Meccanica 51 (11) (2016) 2589–2606. doi:10.1007/s11012-016-0374-6.

[70] F. Clementi, S. Lenci, G. Rega, Cross-checking asymptotics and numerics in the hardening/softening behaviour of Timoshenko beams with axial end spring and variable slenderness, Archive of Applied Mechanics 87 (5) (2017) 865–880. doi:10.1007/s00419-016-1159-z.

[71] S. Lenci, F. Clementi, G. Rega, Comparing nonlinear free vibrations of Timoshenko beams with mechanical or geometric curvature definition, Procedia IUTAM 20 (2017) 34–41. doi:10.1016/j.piutam.2017.03.006.

[72] S. Lenci, F. Clementi, Axial-transversal coupling in the nonlinear dynamics of a beam with an inclined roller, International Journal of Mechanical Sciences 144 (2018) 490–501. doi:10.1016/j.ijmecsci.2018.06.007.

[73] S. Lenci, Isochronous Beams by an Inclined Roller Support, Journal of Applied Mechanics 85 (9), 091008. doi:10.1115/1.4040453.

[74] L. Kloda, S. Lenci, J. Warminski, Nonlinear dynamics of a planar hinged-supported beam with one end lumped mass and longitudinal elastic support, MATEC Web of Conferences 241 (2018) 01016. doi:10.1051/matecconf/201824101016.

[75] L. Kloda, S. Lenci, J. Warmiński, Nonlinear dynamics of a planar hinged-supported beam with one end spring system, MATEC Web of Conferences 148 (6) (2018) 06004. doi:10.1051/matecconf/201814806004.

[76] L. Kloda, S. Lenci, J. Warminski, Nonlinear dynamics of a planar beam–spring system: analytical and numerical approaches, Nonlinear Dynamics 94 (3) (2018) 1721–1738. doi:10.1007/s11071-018-4452-2.

[77] L. Kloda, S. Lenci, J. Warminski, Nonlinear dynamics of a planar hinged-simply supported beam with one end spring: Higher order resonances, in: I. Kovacic, S. Lenci (Eds.), IUTAM Symposium on Exploiting Nonlinear Dynamics for Engineering Systems, Vol. 37 of IUTAM Bookseries, Springer International Publishing, Cham, 2020, pp. 155–165. doi:10.1007/978-3-030-23692-2_14.

[78] L. Kloda, S. Lenci, J. Warmiński, Hardening vs softening dichotomy of a hinged-simply supported beam with one end axial linear spring: experimental and numerical studies, International Journal of Mechanical Sciences (in press) 1–22.

[79] E. Babilio, S. Lenci, On the notion of curvature and its mechanical meaning in a geometrically exact plane beam theory, International Journal of Mechanical Sciences 128-129 (2017) 277–293. doi:10.1016/j.ijmecsci.2017.03.031.

[80] E. Babilio, S. Lenci, Consequences of different definitions of bending curvature on nonlinear dynamics of beams, Procedia Engineering 199 (2017) 1411–1416. doi:10.1016/j.proeng.2017.09.382.

[81] J. Brouwers, Response near resonance of non-linearly damped systems subject to random excitation with application to marine risers, Ocean Engineering 9 (3) (1982) 235–257. doi:10.1016/0029-8018(82)90016-6.

[82] I. Chueshov, I. Lasiecka, Attractors for second-order evolution equations with a nonlinear damping, Journal of Dynamics and Differential Equations 16 (2) (2004) 469–512. doi:10.1007/s10884-004-4289-x.

[83] A. Eichler, J. Moser, J. Chaste, M. Zdrojek, I. Wilson-Rae, A. Bachtold, Nonlinear damping in mechanical resonators made from carbon nanotubes and graphene, Nature nanotechnology 6 (6) (2011) 339–342. doi:10.1038/nnano.2011.71.

[84] S. J. Elliott, M. Ghandchi Tehrani, R. S. Langley, Nonlinear damping and quasi-linear modelling, Philosophical transactions. Series A, Mathematical, physical, and engineering sciences 373 (2051) (2015). doi:10.1098/rsta.2014.0402.

[85] M. Amabili, Nonlinear damping in nonlinear vibrations of rectangular plates: Derivation from viscoelasticity and experimental validation, Journal of the Mechanics and Physics of Solids 118 (2018) 275–292. doi:10.1016/j.jmps.2018.06.004.

[86] H. Goldstein, C. Poole, J. Safko, Classical Mechanics, 3rd Edition, Addison Wesley, London, 2002.

[87] A. H. Nayfeh, B. Balachandran, Applied Nonlinear Dynamics, Wiley, 1995. doi:10.1002/9783527617548.

[88] A. H. Nayfeh, Introduction to perturbation techniques, Wiley-VCH Verlag GmbH, [E.U.A.], 2004.

[89] A. H. Nayfeh, C.-M. Chin, Pertubation methods with mathematica (2004).
URL https://gedube.ga/perturbationmethodswith.pdf

[90] A. H. Nayfeh, D. T. Mook, Nonlinear oscillations, Physics textbook, Wiley, Weinheim, 2007.

[91] A. H. Nayfeh, Perturbation methods, Physics textbook, Wiley, Weinheim, 2007.

[92] A. H. Nayfeh, Linear and Nonlinear Structural Mechanics, 1st Edition, Wiley Series in Nonlinear Science, Wiley-VCH, Weinheim, 2008.

[93] V. Balakrishnan, All about the dirac delta function (?), Resonance - Journal of Science Education 8 (8) (2003) 48–58.
URL http://repository.ias.ac.in/1082/

[94] C. Young, Algebra and trigonometry, John Wiley & Sons, Inc, Hoboken, NJ, 2010.

[95] I. Kovacic, M. J. Brennan, The Duffing equation: Nonlinear oscillators and their phenomena, Wiley, Chichester, West Sussex, U.K and Hoboken, N.J, 2011.

[96] R. P. Felgar, D. Young, Tables of characteristic functions representing normal modes of vibration of a beam, 44th Edition, The University of Texas Publication, 1949.

[97] J. Gawryluk, M. Bochenski, A. Teter, Modal analysis of laminated "CAS" and "CUS" box-beams, Archive of Mechanical Engineering 64 (4) (2017) 441–454. doi:10.1515/meceng-2017-0026.

[98] N. Jaber, A. Ramini, A. A. A. Carreno, M. I. Younis, Higher order modes excitation of electrostatically actuated clamped–clamped microbeams: experimental and analytical investigation, Journal of Micromechanics and Microengineering 26 (2) (2016) 025008. doi:10.1088/0960-1317/26/2/025008.

[99] O. C. Zienkiewicz, R. L. Taylor, The finite element method for solid and structural mechanics, 6th Edition, Elsevier Butterworth-Heinemann, Oxford and Burlington, MA, 2005.

[100] O. C. Zienkiewicz, R. L. Taylor, J. Z. Zhu, The finite element method: Its basis and fundamentals, 6th Edition, Elsevier Butterworth-Heinemann, Amsterdam and Boston, 2005.

[101] C. Lanczos, An iteration method for the solution of the eigenvalue problem of linear differential and integral operators, Journal of Research of the National Bureau of Standards 45 (4) (1950) 255. doi:10.6028/jres.045.026.

[102] G. Kerschen, M. Peeters, J. C. Golinval, A. F. Vakakis, Nonlinear normal modes, part i: A useful framework for the structural dynamicist, Mechanical Systems and Signal Processing 23 (1) (2009) 170–194. doi:10.1016/j.ymssp.2008.04.002.

[103] H. Yabuno, A. H. Nayfeh, Nonlinear normal modes of a parametrically excited cantilever beam, Nonlinear Dynamics 25 (1/3) (2001) 65–77. doi:10.1023/A:1012938213046.

[104] D. Jiang, C. Pierre, S. W. Shaw, Large-amplitude non-linear normal modes of piecewise linear systems, Journal of Sound and Vibration 272 (3-5) (2004) 869–891. doi:10.1016/S0022-460X(03)00497-8.

[105] W. Lacarbonara, G. Rega, A. H. Nayfeh, Resonant non-linear normal modes. part i: analytical treatment for structural one-dimensional systems, International Journal of Non-Linear Mechanics 38 (6) (2001) 851–872. doi:10.1016/S0020-7462(02)00033-1.

[106] H. E. Nusse, J. A. Yorke, Basins of attraction, Science 271 (5254) (1996) 1376–1380. doi:10.1126/science.271.5254.1376.

[107] L. Börgesson, Abaqus, in: Coupled Thermo-Hydro-Mechanical Processes of Fractured Media - Mathematical and Experimental Studies, Vol. 79 of Developments in Geotechnical Engineering, Elsevier, 1996, pp. 565–570. doi:10.1016/S0165-1250(96)80047-2.

[108] H. Poincaré, Science and hypothesis, London W. Scott.
URL https://archive.org/details/scienceandhypoth00poinuoft/page/n6

[109] T. Schultheiss, Vibration Test System TV 59335/AIT-340TGT MO 48 XL: Technical Documentation: (S/N:267/10), Schalkau, 2006.
URL www.tira-gmbh.de

[110] The calculation of the weight and length of the expanded coil cylindrical steel(in polish: Obliczenie ciężaru i długości w rozwinięciu sprężyny walcowej ze stali) (2019).
URL http://www.springs.com.pl/oblicz.php

[111] Altuglas International Arkema Group, General information and physical properties: Booklet (2019).
URL https://www.plexiglas.com/export/sites/plexiglas/.content/medias/downloads/sheet-docs/plexiglas-general-information-and-physical-properties.pdf

[112] Shimadzu Corporation, Technical documentation - practical testing solutions (2015).
URL https://www.ssi.shimadzu.com/sites/ssi.shimadzu.com/files/Products/literature/testing/C224-E057B.pdf

[113] R. D. Blevins, Formulas for natural frequency and mode shape, reprint ed. Edition, Krieger, Malabar, FL, 2001.

[114] D. J. Inman, Engineering vibration, 3rd Edition, Pearson Education, Upper Saddle River, 2008.

[115] Polytec, Technical dcumentation: (2005).
URL https://www.polytec.com/eu/vibrometry/products/full-field-vibrometers/psv-500-scanning-vibrometer/

[116] H. Tabatabai, D. E. Oliver, J. W. Rohrbaugh, C. Papadopoulos, Novel applications of laser Doppler vibration measurements to medical imaging, Sensing and imaging 14 (2013) 13–28. doi:10.1007/s11220-013-0077-1.

[117] M. Amabili, Nonlinear damping in large-amplitude vibrations: modelling and experiments, Nonlinear Dynamics 93 (1) (2018) 5–18. doi:10.1007/s11071-017-3889-z.

[118] J. Gawryluk, A. Mitura, A. Teter, Use of an active element for dynamic control of a thin-walled laminated beam with kinematic excitation, Archive of Mechanical Engineering (3) (2019) 379–387. doi:10.24425/ame.2019.129681.

[119] A. Teter, J. Gawryluk, M. Bochenski, Experimental and numerical studies of a cracked thin-walled box-beams, Composite Structures 202 (2018) 807–817. doi:10.1016/j.compstruct.2018.04.029.

[120] D. J. Ewins, Modal testing: Theory, practice and application, 2nd Edition, Vol. 10 of Mechanical engineering research studies Engineering dynamics series, Research Studies Press, Baldock, 2000.

[121] P. H. McDonald, Nonlinear dynamics of a beam, Computers & Structures 40 (5) (1991) 1315–1320. doi:10.1016/0045-7949(91)90401-7.

[122] J. W. Cooley, J. W. Tukey, An algorithm for the machine calculation of complex fourier series, Mathematics of Computation 19 (90) (1965) 297. doi:10.2307/2003354.

[123] J. J. Thomsen, Vibrations and Stability, Springer Berlin Heidelberg, Berlin, Heidelberg, 2003. doi:10.1007/978-3-662-10793-5.

[124] M. H. Ghayesh, H. A. Kafiabad, T. Reid, Sub- and super-critical nonlinear dynamics of a harmonically excited axially moving beam, International Journal of Solids and Structures 49 (1) (2012) 227–243. doi:10.1016/j.ijsolstr.2011.10.007.

[125] C. Samanta, P. R. Yasasvi Gangavarapu, A. K. Naik, Nonlinear mode coupling and internal resonances in mos 2 nanoelectromechanical system, Applied Physics Letters 107 (17) (2015) 173110. doi:10.1063/1.4934708.

[126] J. H. Yang, M. A. Sanjuán, H. G. Liu, Vibrational subharmonic and superharmonic resonances, Communications in Nonlinear Science and Numerical Simulation 30 (1-3) (2016) 362–372. doi:10.1016/j.cnsns.2015.07.002.

[127] A. A. Afaneh, R. A. Ibrahim, Nonlinear response of an initially buckled beam with 1:1 internal resonance to sinusoidal excitation, Nonlinear Dynamics 4 (6) (1993) 547–571. doi:10.1007/BF00162232.

[128] P. Ribeiro, M. Petyt, Non-linear vibration of beams with internal resonance by the hierarchical finite-element method, Journal of Sound and Vibration 224 (4) (1999) 591–624. doi:10.1006/jsvi.1999.2193.

[129] M. H. Ghayesh, S. Kazemirad, M. Amabili, Coupled longitudinal-transverse dynamics of an axially moving beam with an internal resonance, Mechanism and Machine Theory 52 (2012) 18–34. doi:10.1016/j.mechmachtheory.2012.01.008.

[130] C. Lan, W. Qin, W. Deng, Energy harvesting by dynamic unstability and internal resonance for piezoelectric beam, Applied Physics Letters 107 (9) (2015) 093902. doi:10.1063/1.4930073.

[131] E. Peterson, F. B. Llewellyn, The operation of modulators from a physical viewpoint, Proceedings of the IRE 18 (1) (1930) 38–48. doi:10.1109/JRPROC.1930.221883.

[132] V. Sharma, C. O. Arun, I. P. Krishna, Development and validation of a simple two degree of freedom model for predicting maximum fundamental

sloshing mode wave height in a cylindrical tank, Journal of Sound and Vibration 461 (2019) 114906. doi:10.1016/j.jsv.2019.114906.

[133] J. Náprstek, C. Fischer, Super and sub-harmonic synchronization in generalized van der pol oscillator, Computers & Structures 224 (2019) 106103. doi:10.1016/j.compstruc.2019.106103.

[134] B. Bharat, V. R. Sonti, Resonance and beating phenomenon in a nonlinear rigid cylindrical acoustic waveguide: The axisymmetric mode, Journal of Sound and Vibration 458 (2019) 262–275. doi:10.1016/j.jsv.2019.06.025.

[135] J. Awrejcewicz, J. Mrozowski, P. Olejnik, M. Jastrzebska, O. Jarzyna, M. Kaźmierczak, G. Kudra, S. Bartosz, G. Wasilewski, A. Wijata, W. Kunikowski, M. Ludwicki, B. Zagrodny (Eds.), 15th International Confernce Dynamical Systems — Theory and Applications: Nonlinear dynamics of a planar beam-spring system: a 2:1 internal transversal-axial resonance, L. Kloda, S. Lenci, J. Warminski, 2019.
URL https://www.dys-ta.com/

[136] G. Pickett, Equations for computing elastic constants from flexural and torsional resonant frequencies of vibration of prisms and cylinders, Proc. ASTM 45 (1945) 846–865.

[137] S. Spinner, T. W. Reichard, W. E. Tefft, A comparison of experimental and theoretical relations between Young's modulus and the flexural and longitudinal resonance frequencies of uniform bars, Journal of Research of the National Bureau of Standards Section A: Physics and Chemistry 64A (2) (1960) 147. doi:10.6028/jres.064a.014.